Influences of Processing and Composition on the Grain Boundary Character Distribution

Herbert M. Miller III
Department of Materials Science and Engineering
Carnegie Mellon University
December 4, 2008

Abstract

Experiments were performed to observe the effects of processing and composition on the grain boundary character distribution (GBCD) of $SrTiO_3$, MgO, and Ni. Anisotropic interfacial energies and, in the case of nickel, crystallographic constraints, are expected to influence the evolution of the GBCD during processing.

Interrupted grain growth experiments were performed with $SrTiO_3$ to observe the evolution of the GBCD with grain growth. The GBCD was determined at three time steps during grain growth and quantitative comparisons were made. Guidelines for quantitative comparisons of grain boundary plane distributions (GBPDs) and GBCDs were established Relative grain boundary energies were evaluated using two independent techniques to observe the relationship between grain boundary population and energy and the role that grain boundary energy has in determining the GBCD.

It was found that anisotropic interfacial energies dictate an anisotropic GBCD which develops very early in the grain growth process for $SrTiO_3$. The GBPD remains constant even as the grain size increases. Relatively low energy {100} grain boundary planes are favored. The five parameter GBCD evolves during grain growth to eliminate relatively higher energy grain boundaries while lower energy grain boundaries are preserved.

Doping was explored as a processing technique to alter the GBCD in MgO. The GBCDs of 3000 ppm Ca-doped MgO and undoped MgO were measured and quantitatively compared. Relative grain boundary energy anisotropy was determined for each material and compared to the anisotropy of the GBPD.

Calcium doping in MgO increases the anisotropy of the GBPD and GBCD. Specifically, the relative population of {100} grain boundary orientations increases with doping. In the five parameter GBCD of the pure material, some misorientations favor {100} boundary plane orientations and in these cases, the doping increases this preference. For misorienations in the pure material that favor {111} boundary plane orientations, the preference for {111} is diminished or the preference switches to {100} orientations. The anisotropy of the grain boundary energy distribution increases with doping.

Iterative thermomechanical processing was explored as a technique to alter the GBCD in nickel. GBCDs were determined before and after iterative thermomechanical processing for both commercially available "grain boundary engineered" (Integran) and high purity nickel. Triple junction analysis was performed in which triple junctions were classified according to the types of grain boundaries that formed the junction. The relative grain boundary energy distribution was also determined for high purity nickel.

Grain boundary energy was also found to be a factor of influencing GBCD evolution during iterative thermomechanical processing. Boundaries with relatively higher energy decrease in population while lower energy boundaries increase in population. Specifically, random boundaries are preferentially eliminated while the population of $\Sigma 3$ boundaries increases. However, because the evolution mechanism is different than in grain growth, and relies more on local rearrangements of boundaries rather than large scale elimination of interfacial area, constraints placed on the resulting network of boundaries influence the GBCD as well. Thus, interfacial energy is not the sole factor that determines the GBCD in nickel. The population of incoherent $\Sigma 3$

4

boundaries increases more than the population of the much lower energy coherent $\Sigma3$ boundaries. $\Sigma9$ and $\Sigma27$ boundaries are also observed to increase in population. These boundaries tend to be the result of interacting $\Sigma3$ boundaries. This conclusion is supported by the triple junction populations that show an increase in triple junctions that are comprised of two or three $\Sigma3^n$ type boundaries, where $n = 1,2,$ or 3. A mechanism is proposed that accounts for the increased population of incoherent $\Sigma3$ boundaries, the increased populations of $\Sigma9$ boundaries, and the observed triple junction populations.

Acknowledgements

There are far too many people who have aided or supported me in some manner throughout my entire academic career – my entire life – to list them all in this setting. If you're upset you didn't make the list, I'm truly sorry, but trust me – I remember exactly how you helped me, and will never forget for a single moment. With that said, I of course need to acknowledge the people who were most instrumental in helping me achieve my current level of success. My parents, Steph and Herb, and my grandparents, instilled a love of learning and supported my curiosity from a very early age. I am certain that Camp Boompa and rock and roll into my crib late into the night have played a huge positive role in determining who I am today. I am also indebted to all former members of the Rohrer group - especially Drs. Jennifer Giocondi, Chang-Soo Kim, Bassem el-Dasher, and David Saylor. Each played an instrumental role in teaching me how to think and act like a scientist and life-long student. Of course, nothing would ever get done at a university without the support staff. I consider myself lucky to have worked with the great staff of the Carnegie Mellon Materials Science and Engineering Department – all of whom were always helpful and above all, just plain nice. Even if Suzanne Smith did tease me all the time. Many good friends have helped me over the years, but I will never forget just how much Jason Gruber helped me – academically, mentally, and gastronomically! Miles Hinderliter helped a little, too.

But, even with all of the aforementioned support, none of this would have been possible for me if it wasn't for my advisor, Professor Gregory Rohrer. I consider him the professional model that I aspire to, and a true friend. I will never be able to repay him for all of the ways that he has helped me grow as a person and as a scientist. I intend to

spend the rest of my career striving to deserve the opportunities that I have because of

him, though. Thanks.

Table of Contents

Chapter 1

1. Introduction

1.1 Motivation

Many engineering solutions require the use of materials that are polycrystalline. These solid materials are made up of many misoriented crystallites joined at grain boundaries. Understanding the effects of polycrystalline microstructures on materials properties (mechanical, electrical, chemical, etc.) is an important ongoing area of research in the field of materials science. Among the widely studied aspects of the microstructure are the grain size, grain size distribution, second phase contributions to properties, orientation/misorientation texture and porosity. These studies have led to greater understanding of microstructure/properties relationships. Until recently, though, little work has been done to fully characterize the distribution of grain boundary types in materials.

The full macroscopic description of a grain boundary requires knowledge of both grain-to-grain misorientation and the orientation of the grain boundary plane. This description requires five independent parameters [1] and is typically referred to as the five parameter grain boundary character distribution (GBCD). Thus, the parameter space that encompasses the range of possible general boundaries is large. As a result, the scope of much previous work characterizing grain boundaries was restricted to boundaries with simplistic geometries. Recent advances in microscopic techniques and computational power allow a statistically significant number of grain boundaries to be analyzed considering both misorientation and orientation of the grain boundary plane. To better

understand the effects of grain boundaries on materials properties, it is necessary to first gain greater understanding of the types of boundaries in materials. With this information, and some knowledge of the factors that determine the types of boundaries that occur, it becomes possible to imagine scenarios for manipulation of the GBCD with intent to improve materials properties.

1.2 Objective

The objective of this research is to explore the evolution of the five parameter GBCD during processing. Evolution of the GBCD was studied during both capillary driven grain growth and during sequential thermo-mechanical processing, or "grain boundary engineering" (GBE) [2]. In the former, changes in the GBCD are driven by a reduction of interfacial energy, and in the latter case, changes are driven in part by the relaxation of stored energy. Previous work has described the anisotropic nature of the GBCD and its relation to the surface energy anisotropy at a single point in time [3, 4] but the question of how these distributions arise has not been experimentally addressed in significant detail. Studies of the evolution of the GBCD in liquid-phase containing ceramic systems shed some light on these issues [5, 6]; however, it is expected that the results will be different for dense solid materials. Simulation results predict anisotropic, steady state behavior of the GBCD [7, 8]; these results will be tested experimentally. Sequential thermo-mechanical processing is explored as a technique for predictably altering the evolution of the GBCD with the goal of achieving desired materials properties.

A previously established stereological procedure for calculating the GBCD will be used in this work [9]. Uncertainties associated with this technique will be addressed, and guidelines for consistent and accurate determination of the GBCD for quantitative comparison will be established.

1.3 Hypothesis

If there is no anisotropy in particle shape, packing in a uniaxially compacted powdered ceramic should be random and there will likely be little or no anisotropy in the types of interfaces between particles found in the green body. During the first stages of sintering, it is possible that this will lead to an initial GBCD that is isotropic. It is hypothesized that following a transitory period, the GBCD will be statistically self similar with normal grain growth. In the context, self similarity means that the GBCD will be independent of the mean grain size. This state will be inversely related to the grain boundary energy anisotropy of the material. Lower energy grain boundaries will be both larger in area and occur more frequently than in a random distribution of boundary types. The resultant distribution of grain boundary types will be a result of the preferential elimination of higher energy boundaries, the increase in area of lower energy boundaries, and the generation of new boundary area during normal grain growth. A schematic of this hypothesis will be presented in Chapter 2.

It is further hypothesized that changing the surface energy or grain boundary energy anisotropy will result in a change in the steady state behavior of the GBCD. Sequential thermo-mechanical processing of fcc metals leads to changes in the steady state GBCD that are influenced by topological, as well as energetic, factors.

1.4 Method

To characterize the evolution of the GBCD during simple grain growth, electron backscatter diffraction (EBSD) in a scanning electron microscope will be used in a semi-automatic fashion to collect orientation maps of planar surfaces for several polycrystalline samples. From this data, grain-to-grain misorientations as well as in-plane boundary angles can be extracted. This provides four of the five parameters necessary for specifying a grain boundary type. The inclinations of specific grain boundaries, however, are unknowable from this data. Previous measurements of the GBCD with an EBSD-based technique have relied on either serial sectioning [10, 11] or a stereological-based approach [9] for recovery of this fifth parameter. For the work presented in this document, a stereological approach will be used to statistically determine the GBCD. This stereological approach has been shown to give results comparable to those obtained with serial sectioning for materials with little or no orientation texture [9]. It should be noted that serial sectioning, while experimentally challenging, is the only way to determine inclinations of specific grain boundaries. Serial sectioning also allows for recovery of grain boundary energy anisotropy and provides insight into the connectivity of the grain boundary network. While the experiments in this thesis rely mostly on stereology, some automated serial sectioning experiments in a dual beam focused ion beam microscope were used to evaluate relative grain boundary energies.

Because of the statistical nature of the stereological technique, the amount of data used in the calculation can strongly affect the reliability of the GBCD determination. These issues will be addressed in detail in Chapter 2, Section 2, and Chapter 3, Sections

3.3 and 3.4. High-symmetry cubic materials will be studied in this thesis because it is known that they will require the least amount of data for reliable results. Furthermore, materials are selected for which we have some pre-existing knowledge of the GBCD and for which EBSD preparation and data collection procedures have already been established [3-5]. From these materials, $SrTiO_3$, MgO and Ni have been chosen as model systems. Ceramic materials prove to be convenient model materials to monitor GBCD evolution during capillarity driven grain growth because it is possible to get as close to a random starting point as possible by starting from powders. To compare this form of GBCD evolution to evolution by deformation processing, it is more necessary to work with a metallic system. Nickel is a reasonable choice in this case because in spite of the substantial existing literature dealing with "grain boundary engineering" in nickel, the mechanisms of GBCD evolution with mechanical processing for this material are still not completely understood.

Grain growth experiments will be completed with polycrystalline $SrTiO_3$. Samples will be prepared with conventional powder processing techniques and the GBCD will be determined at various times during grain growth at a constant temperature in an ambient atmosphere.

The GBCD will be determined for a nominally pure and Ca-doped MgO samples to observe the effects of doping on grain boundary energy anisotropy and the resultant effects on the GBCD.

Sequential thermo-mechanical processing experiments will be completed with commercially available "grain boundary engineered" Ni (Integran, Technology, Inc.) and high-purity Ni samples (Alfa Aesar 99.999%). The GBCD will be determined and

compared for "reference" and "grain boundary engineered" states. Specific attention will be paid to the populations of so called "special" boundaries (boundaries with some degree of coincidence or relatively simple geometry) and to describing the triple junction distributions of the samples.

To support the hypothesis of an inverse correlation of interfacial energy anisotropy and the GBCD, it is necessary to determine the relative energies of grain boundaries. Atomic force microscope (AFM) measurements of thermal grooves in polycrystalline materials have proven to be a relatively simple technique for determining interfacial energy anisotropy [12, 13]. This is the one of the techniques employed in the present work. Thermal groove geometries will be measured for several $SrTiO_3$ and MgO samples. From these measurements, a distribution of relative grain boundary energies in the material of interest will be determined. Serial sectioning can also be used to determine the true dihedral angles of certain grain boundaries. From this information, relative grain boundary energies can be calculated [14]. Focused Ion Beam (FIB) milling, coupled with EBSD orientation mapping, will be employed to calculate relative grain boundary energies for $SrTiO_3$ to support the thermal groove geometry results. The same technique will be applied to nickel.

Chapter 2

2. Background

2.1 Introduction

Dense polycrystalline materials are comprised of many adjacent single crystals, misoriented with respect to each other. These crystals, referred to as grains, are joined by a three-dimensional network of internal interfaces known as grain boundaries. It is this network of grain boundaries (along with several other potential components) that is typically referred to as the "microstructure" of a material. Microstructural evolution and microstructure/property relationships have long been subjects of research for materials scientists. Such studies naturally require microstructural characterization. Historically, microstructure was studied primarily from two dimensional planar sections. Many of the existing theories of microstructural evolution are based on these observations, and assume isotropic interface properties. It was not until the last two decades or so that new experimental techniques and increases in computing power have allowed for the study of the true three dimensional shapes of grains and the connectivity of the interfacial network. Still, there are relatively few experimental and theoretical observations that relate anisotropic interface properties to microstructural evolution.

In this section, parameters required to distinguish grain boundaries and the distribution of grain boundaries present (the grain boundary character distribution, or GBCD) in materials will be defined. A review of measurements of the GBCD, the correlation between GBCD and material properties, as well as the relationship between the GBCD and grain boundary energy will be presented. Next, the existing experimental

results concerning the evolution of the GBCD, along with various simulation results, will be reviewed. Finally, results describing the evolution of the GBCD with sequential thermo-mechanical processing ("grain boundary engineering") of cubic close-packed metals will be addressed.

2.2 Distinguishing Grain Boundaries

The orientations of the grains in polycrystalline solids are typically specified with respect to sample coordinates. One such way of specifying orientations utilizes three Eulerian angles, ϕ_1, Φ, and ϕ_2, to describe a series of rotations that bring the crystal axes into coincidence with the sample reference axes. This transformation may be represented as a 3x3 matrix denoted as $g(\phi_1, \Phi, \phi_2)$. Crystal systems exhibit symmetry which must be considered when specifying orientations. For M symmetry operators in a crystal class, there will be M transformations that will result in indistinguishable crystal orientations.

Polycrystallography is unsurprisingly more complex than crystallography. The macroscopic description of a grain boundary for a single phase material requires the specification of five independent parameters [1]. In the present work, three parameters are used to describe the lattice misorientation (Δg) across a boundary and two parameters are used to describe the interface normal (**n**) [3]. Just as an orientation may be represented by a transformation matrix relating crystal coordinates to sample reference axes, the misorientation between two crystallites can also be represented by a transformation matrix based on Eulerian angles that describe the orientation of one crystallite with respect to another. The full domain of misorientation space can be

described with ϕ_1, Φ, and ϕ_2, which range from $0-2\pi$, $0-\pi$, and $0-2\pi$, respectively. For all of the calculations in this work, a subset of this domain with dimensions of $0 - \pi/2$, $0 - \pi$, and $0 - \pi/2$ is used. All possible unique misorientations are contained within this volume, but there are still redundancies. Within this sub-domain, there are always more than one set of rotations that are equivalent to a unique misorientation. For cubic materials, there are 36 equivalent representations. Alternatively, misorientation between two adjacent crystallites can be described as a rotation about a common misorientation axis (crystallographic direction). This description is used frequently in the literature. Three parameters are required to specify a misorientation in this scheme as well. It is this description that will be used for the presentation of the data in this work.

Two spherical angles, θ and ϕ, are required to parameterize the domain of interface normal orientations. For centrosymmetric crystals, θ and ϕ range from $0 - \pi/2$ and $0 - 2\pi$, respectively.

The function that describes the distribution of grain boundaries in a material is then dependent upon the same five parameters required to define a grain boundary. This function is the five parameter grain boundary character distribution (GBCD), $\lambda(\Delta g, \mathbf{n})$. The five parameter GBCD describes the relative areas of internal grain surfaces as a function of lattice misorientation and grain boundary plane orientation. The GBCD is normalized by the random distribution of grain boundaries to highlight characteristics that are different from random. Grain boundary population is then reported using units of multiples of a random distribution, or MRD. If boundary types are distributed randomly, the $\lambda(\Delta g, \mathbf{n}) = 1$ for all boundary types. Throughout this work, the subdomain is partitioned into discrete cells [3]. This partitioning will affect the number of

distinguishable boundary types and will be discussed in more detail in the experimental section (Chapter 3, Section 3.4).

A common parameterization for grain boundary character is $\lambda(\theta)$, the relative populations of boundaries as a function of a single disorientation angle, θ. The disorientation is smallest possible rotation angle among any of the symmetrically equivalent rotation axis and angle pairs. When the grain boundary character distribution is based solely on misorientation, it is known as the misorientation distribution function (MDF). Another misorientation-based approach of describing grain boundaries is to determine the population of "special" configurations which result in coincidence of lattice positions in the adjacent grains. This is the "coincident site lattice" (CSL) model first proposed by Kronberg, et al. [15]. In this paradigm, boundaries are classified by a Σ number that represents the inverse of coincident lattice sites for a given misorientation. This system has its advantages, but also limitations that will be addressed in the next few sections.

It is sometimes convenient to describe the grain boundary character solely based on misorientation ($\lambda(\Delta g)$) or on boundary plane orientation ($\lambda(\mathbf{n})$), which is measured independently of lattice misorientation across a grain boundary. While neither is adequate to fully describe boundary types in materials, it can be instructive to consider these distributions separately.

All of these distributions will be used in this work, while never losing focus on the requirement of using the five parameter GBCD to most accurately describe grain boundary types in materials. The terms "grain boundary character," or "grain boundary

type," will be used interchangeably within the context of the parameters being considered in the given experiment.

2.3 Characteristics of the Grain Boundary Character Distribution and the Relation to Anisotropic Interfacial Energies

Recent measurements of the GBCD for a wide range of materials including ceramic systems such as MgO [9, 10], $SrTiO_3$ [11], TiO_2 [4], $MgAl_2O_4$ [16], and metallic systems such as Al [17], Fe-1%Si [18], Cu [19], α-brass [20, 21], and 316 stainless steel [22] have led to several important conclusions, as summarized by Rohrer [23]. First, in all observed cases, the distribution of grain boundary planes, $\lambda(\mathbf{n})$, is anisotropic. Second, it was observed that the preferred habit planes for grains within polycrystals correspond to the same low energy, low index planes that dominate external growth forms and equilibrium shapes of isolated crystals of the same phase [4]. It is noteworthy that topological connectivity constrains grains from being entirely bounded by these habit planes. A correlation between grain boundary energies and the sum of the energies of surfaces that comprise the boundaries is observed experimentally as well [12-14]. This correlation corresponds with results from earlier simulation work performed by Wolf [24, 25]. This leads to the important result that grain surface relationships are more important than misorientation relationships in determining grain boundary character. The CSL framework, which only depends upon misorientation relationships, does not suitably distinguish boundaries with respect to their properties. As an example, experimental measurements of the GBCD in Al [17] show that when considering the MDF, Σ3

misorientation boundaries (where the misorientation can be described as a 60° rotation about a [111] misorientation axis) occur with a frequency of 2 MRD, where MRD is multiple of random distribution. When looking at the full five dimensional space, though, coherent twins (characterized as a $\Sigma 3$ misorientation with {111} boundary planes) occur with a frequency of 25 MRD. This means that for those boundaries with $\Sigma 3$ misorientation, there is a much higher probability of finding {111} bounding planes. It can be assumed that this configuration has special properties, namely relatively low energy. This "special" configuration depends upon coincidence in the boundary plane and thus all five macroscopic parameters. This concept will be dealt with in more detail when defining "grain boundary engineering" as a method of affecting the evolution of the GBCD.

The aforementioned results suggest that knowledge of surface energy anisotropy may allow predictions of grain boundary energy anisotropy, a quantity that is much more difficult to characterize. The final important observation is that the GBCD shows an approximately inverse correlation to the anisotropic distribution of grain boundary energies, $\gamma(\Delta g, \mathbf{n})$. The population with respect to grain boundary energy for an MgO sample is plotted in Fig. 2.1 [10].

The population of low energy boundaries is greater than the population of high energy boundaries, roughly in proportion to the amount of anisotropy in the grain boundary energy distribution. The population of grain boundaries describes the relative areas of specific types of boundaries. An increase in relative area can be attributed to either an increase in the number of specific boundaries, an increase in length (area) of specific boundaries, or a combination of both. Experiments have shown that a

23

combination of both typically occur [11]. From these results captured at single points in time, it is clear that anisotropic properties affect the GBCD. The goal of this thesis is to determine how these distributions evolve with time.
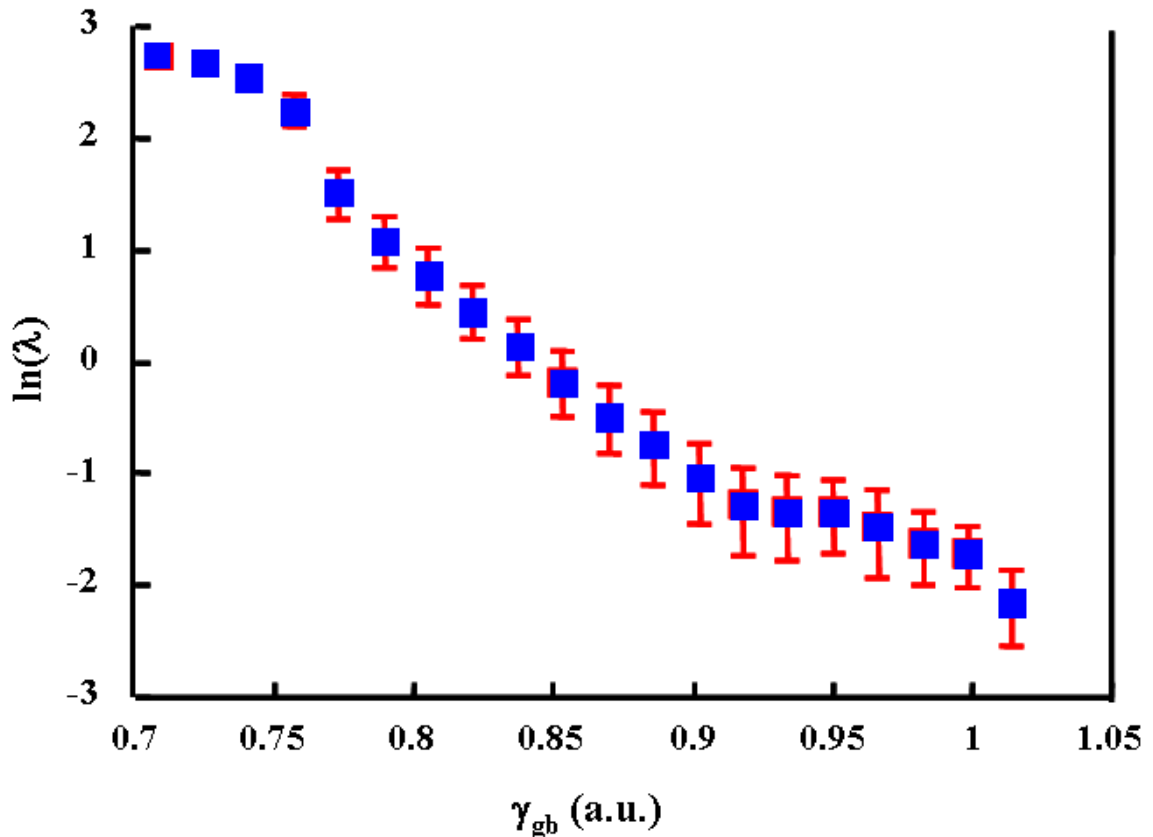
Figure 2.1 An approximately inverse correlation between $\ln(\lambda)$ and grain boundary energy, γ_{gb}, is demonstrated for an MgO sample. Figure reproduced from [10].

2.4 The GBCD and Materials Properties

Past treatments of microstructure/property relations tend to rely on an assumption of isotropic boundary properties or anisotropic boundary properties that are only based on misorientation. This is obviously an incomplete approach. Recent simulation works highlight the importance of considering anisotropic boundary properties and the

importance of five dimensional parameterization of grain boundary types when considering grain boundary classification and property relationships [26, 27].

Saylor and Fuller [26] attempt to establish a relationship between the crystallographic configuration of grains in calcite and dolomite and the thermoelastic response of the materials. Finite element modeling of two-dimensional microstructures mimicking the thermoelastic properties of calcite and dolomite was used to study the effects of both orientation and misorientation texture on thermoelastic properties. A model microstructure was generated and grains were assigned orientations such that a target orientation texture and misorientation texture were realized. A simulated temperature increase was then applied to determine the strain fields that result because of the thermal expansion mismatch between adjacent grains. This process was repeated, with varying target orientation and misorientation textures, such that 45 hypothetical microstructures were tested. It was determined that misorientation plays a much more important role in affecting the total strain energy density than orientation texture alone. In fact, the total strain energy density for the sample with maximum assigned misorientation texture was found to be as much as three times greater than the random orientation, low misorientation texture case. Local strain energy as a function of position also varied dramatically with the variations in the test microstructures. The observed maximum in local strain energy for a given sample was observed to decrease for microstructures that favored low angle boundaries. The length scale of continuous area with low strain was also observed to increase for microstructures with MDFs that favored low angle boundaries.

Kim et al. [27] also use OOF simulations with hypothetical 2D microstructures with anisotropic thermal expansion properties to calculate the local elastic energy density of quenched samples. In this case, the authors expand the description of grain boundaries to five parameters instead of the three that Saylor and Fuller [26] use. In other words, Kim et al. [27] studied the effects of misorientation texture and boundary plane orientation on thermoelastic properties. The elastic energy density was found to depend upon a combination of both the MDF and the grain boundary plane distribution. The main result of this work is that, as expected, misorientation alone is not enough to distinguish grain boundary type, nor grain boundary properties. The role of network connectivity in determining properties is briefly mentioned but not explicitly treated here; this is expected to play an influential role in property determination as well. All five macroscopic parameters and interface anisotropy must be considered for accurate predictions of how microstructures will evolve and what properties the microstructure will have.

.

2.5 Evolution of the Grain Boundary Character Distribution During Grain Growth

2.5.1 Experimental Characterization of GBCD Evolution During Grain Growth

Previous experimental work has focused almost entirely on determining the GBCD for materials in which the factors affecting the GBCD (mechanical processing, annealing or sintering temperature, purity, etc.), were fixed. While measurements of the GBCD have proven to be repeatable within experimental error, previous experimental

work has not addressed the question of whether there exists steady state, scale invariant

GBCDs for polycrystalline samples at fixed temperature, pressure and composition. The

term "self-similarity," which Mullins [28] defines as a state when all statistical

distributions of a microstructure are time (or average grain size) independent, can be

applied to describe such a case. A hypothetical schematic of steady state, or self-similar

behavior of the grain boundary plane distribution with normal grain growth is shown in

Fig. 2.2.
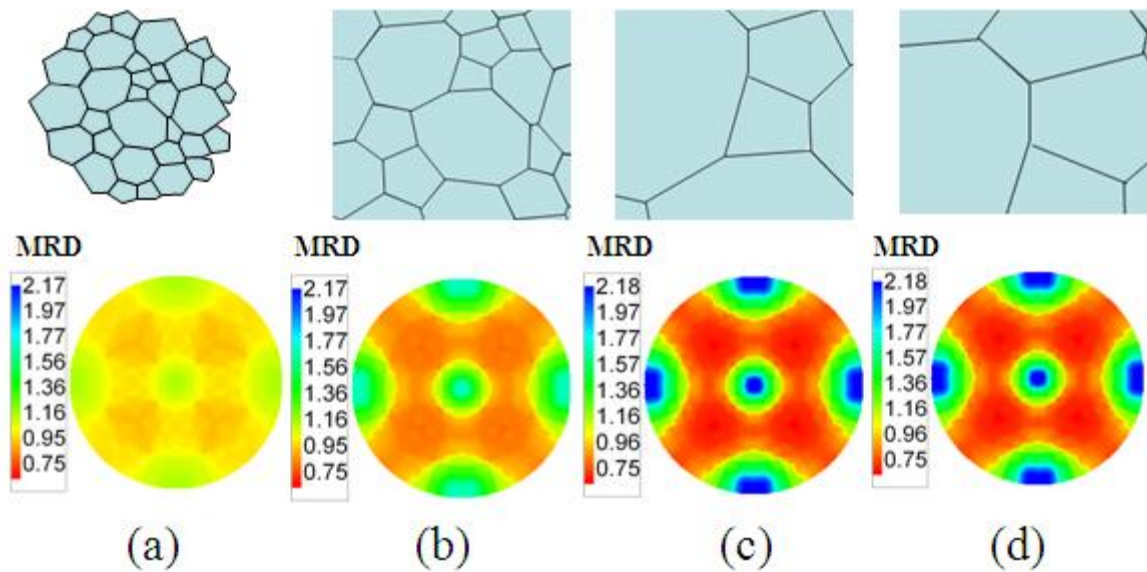
Figure 2.2 Hypothetical schematic of the evolution of the GBPD with normal grain growth for a sintered powder compact. A hypothetical microstructure that is undergoing normal grain growth at constant temperature is shown at four time points, with the GBPD for each plotted in units of multiples of a random distribution (MRD) on stereographic projections with the same scale. (a) A sintered powder compact with no significant particle shape anisotropy initially exhibits no anisotropy in the GBPD. (b) Anisotropy in the GBPD increases with grain growth during a transitory period. (c) Anisotropy in the GBPD achieves a maximum which is influenced by the interfacial energy anisotropy. (d) Anisotropy in the GBPD remains constant for continued self-similar growth of the microstructure.

A similar hypothesis can be made for the evolution of the five parameter GBCD with

normal grain growth, although the situation is likely to be more complex. Of course,

experimental evidence of such behavior is required. Knowledge of steady state behavior of the GBCD and the factors which contribute to it should make it possible to predictably influence the evolution of the GBCD and materials properties that are determined by microstructure.

There is little previous work concerning anisotropic boundary properties and microstructural evolution. Recent simulation and experimental work highlight the importance of considering anisotropic boundary properties for predictions of microstructural evolution [29]. Demirel et al. [29] reported results that show grain growth of simulated microstructures with anisotropic properties more closely match experimentally measured results than those of simulations assuming isotropic properties. These results show that anisotropic boundary properties affect how a microstructure evolves during grain growth, but they do not track how the GBCD evolves with grain growth.

The evolution of the GBCD during grain growth in liquid-containing ceramic systems has been measured [5, 30]. It is expected that this case will be different than the evolution of the GBCD for a dense polycrystal. The presence of a liquid phase may aid in diffusion to an interface, allowing a boundary to reconfigure itself to lower overall energy more easily than in a dense material. The liquid should also eliminate many of the topological constraints that connectivity in a dense sample imposes. Nevertheless, the results of such experiments lend insight into the process of the evolution of the GBCD during grain growth.

In the work cited above, the phase boundary plane distribution, $\lambda(\mathbf{n}_{\mathbf{phase}})$, was determined at various annealing times for liquid-containing PMNPT [30] and SrTiO$_3$ [5]

samples. The phase boundary plane distribution describes the relative areas of grain

boundary planes in contact with the second phase as a function of orientation. The

second phases in these cases are liquid at the chosen annealing temperatures. In each

case, the phase boundary plane distribution shows a propensity for {100}-type boundary

planes, with increasing anisotropy with grain growth. As in previous work, this

demonstrates an inverse correlation with measured (SrTiO$_3$ [13]) or assumed (PMNPT)

surface energy anisotropy. There is no evidence of steady state behavior in either case. It

is possible that there is some eventual limit to the amount of anisotropy in the plane

distribution, but the experiments performed do not address this. In SrTiO$_3$, Sano et al. [5]

report a measureable decrease in the population of {110}-type planes, which have a

higher energy than {100} type planes. Gorzkowski et al. [30] refer to other work on

single crystal growth of PMNPT with varying liquid content [31] to explain results.

Increased liquid content leads to faceting and general slowing of the growth of single

crystals in PMNPT. In their interpretation, interface evolution is then mobility-controlled

and not diffusion-controlled. In each case, the rate of growth slows as the interface

anisotropy increases. This is again explained in terms of mobility – it is assumed that the

more populous boundaries have lower mobilities and as a result remain in the distribution

as higher mobility boundaries move through the microstructure to be eliminated [32]. It

is difficult to separate mobility effects from interfacial free energy effects. Therefore,

some uncertainty remains in this conclusion. It is also possible that this conclusion will

not hold for dense, liquid-free samples.

The GBCD was also recently determined for several liquid phase sintered WC-Co

composites of varying composition and grain size [33]. In this work, Kim et al. [33]

determined the GBCD for seven different WC-Co grades. The carbide volume fraction

ranges from 0.69 to 0.88 and the average grain size ranges from 1.4 μm to 5.3 μm for the

seven samples. Different sintering temperatures were used as well. Despite these

differences, the observed GBCDs for each material are similar. The fraction of WC/Co

changes with changing carbide volume fraction, but the populations of WC/WC

boundaries were found to be similar. Specifically, boundaries that can be described as a

90 ° twist about $[10\bar{1}0]$, a 30 ° twist about [0001], and asymmetric 90 ° tilt boundaries

about $[\bar{2}110]$ are observed to be most prevalent in all the samples studied. results

suggest that the GBCD is indeed independent of grain size and may exhibit steady state

behavior with grain growth. This was not a controlled experiment as the samples were all

prepared in different ways. Therefore, it is not an unambiguous demonstration of scale

independent GBCD behavior.

Recently, Cockayne, et al. [34] have reported experimental observations of the

evolution of specific CSL boundaries with grain growth in polycrystalline $SrTiO_3$. EBSD

orientation mapping was used to measure the MDF of a hot isostatically pressed (HIP)

$SrTiO_3$ sample after one and sixteen hours of annealing in air at 1350 °C. CSL

boundaries with $\Sigma < 45$ were identified using the restrictive Palumbo- Aust criterion [35].

For classification as a CSL boundary within this criterion, boundaries must not deviate by

more than the tolerance angle, which is defined as $\Theta = K\Sigma^{-n}$, where n = 5/6. K is a

chosen acceptable angular deviation, typically taken to be 15 °. The orientation of the

boundary plane, and thus the full five parameter GBCD, was not determined in this work.

Average grain sizes of 0.42 μm and 7.3 μm were observed for the one and sixteen hour

samples, respectively. With grain growth, the density of grain boundaries (length/area)

was observed to decrease by nearly 92 %. Of the selected CSL boundaries, boundaries

with $\Sigma 5$, $\Sigma 7$, and $\Sigma 17$ misorientations are observed to be present with greater frequency

after grain growth, while the frequency of $\Sigma 3$ and $\Sigma 9$ boundaries decreases with grain

growth. Specifically, the density of $\Sigma 3$ boundaries decreases by nearly 99 %. $\Sigma 3$

boundaries appear to be decreasing at a faster rate than general boundaries during grain

growth. One of the major hypotheses of the current work is that grain boundary energy

will play an important factor in determining the equilibrium GBCD during grain growth,

with relatively higher energy boundaries being preferentially eliminated. As a result, $\Sigma 3$

boundaries in $SrTiO_3$ seem to be ideal candidates to test this hypothesis. There are

reports based on experimental and theoretical considerations that suggest that coherent $\Sigma 3$

boundaries in $SrTiO_3$ that are terminated by SrO_3 in the boundary plane are energetically

favorable compared to those that are Ti-terminated [36, 37]. However, these results do

not report the relative energies of $\Sigma 3$ boundaries in $SrTiO_3$ with respect to all other

boundaries. It is possible to estimate the relative energy based upon the sum of the

surface energies of the surfaces that comprise the grain boundary [12, 13, 14]. Using the

energies determined in [13], it is expected that all <111> twist boundaries, including

coherent $\Sigma 3$ boundaries, should be the boundaries with maximum energy. Thus, the

elimination of coherent $\Sigma 3$ boundaries in $SrTiO_3$ with grain growth would be consistent

with the main hypothesis of this work.

2.5.2 Simulations of GBCD Evolution with Grain Growth

Simulations of the evolution of the GBCD with grain growth are more numerous than experimental results. Three dimensional simulations with isotropic boundary properties are capable of reproducing conventional measures of microstructure such as the grain size distribution [36-39], but cannot realistically simulate experimentally determined anisotropic grain boundary distributions which are necessary for accurate modeling of evolution of the GBCD in real materials. Several research groups have published simulation results concerning the evolution of the GBCD for two dimensional hypothetical microstructures with anisotropic boundary properties [7, 42-45]. Upmanyu et al. [42] and Ono et al. [43] classify boundaries by misorientation only; Kinderlehrer et al. [44] and Kazarayan et al. [45] classify boundaries by misorientation and inclination. None of the work is based in three dimensions, however. While these simulations ignored the third spatial dimension and therefore rely on simplifications, they lead to some instructive results.

Ono et al. [43] report results from 2D Monte Carlo Simulations with misorientation-dependent energy in which they attempt to account for high coincidence boundaries as well. In this case, an approximately continuous energy function with a Read-Shockley type energy at low misorientation angles is assigned to low angle boundaries and select CSL boundaries are assigned energies lower than that of "random" boundaries. For a microstructure with initially random orientation texture, they report an increase in the population of low energy boundaries with grain growth.

Holm et al. [7] also report results from Monte Carlo simulations of 2D grain growth with anisotropic boundary properties. A summary of the results of this work are

32

presented in this paragraph and the next. Again, anisotropic, Read-Shockley type

boundary energies based on misorientation are assigned and the microstructure is allowed

to evolve by curvature driven grain growth. For microstructures with initially random

orientation texture, a brief transient period in the evolution of the MDF is followed by

steady state, anisotropic behavior which favors lower angle, lower energy boundaries.

These results are shown in Fig. 2.3. MDFs are plotted for simulations based on Read-

Shockley energies with cutoff disorientations of 15 °, 30 °, and 45 °, above which the

grain boundary energy is constant. When compared to the random "Makenzie

distribution," the MDFs of the simulated grain growth experiments exhibit enhancements

in the low disorientation angle regime and decreases in population for higher

disorientation angles.
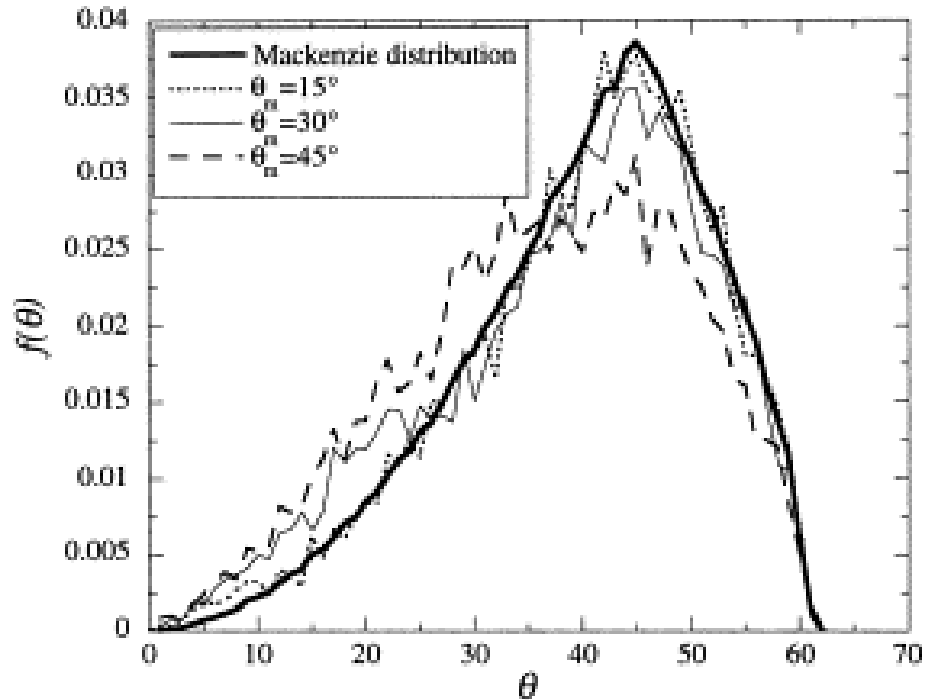
Figure 2.3 Plot of the MDF for grain growth simulations based upon Read-Shockley type
anisotropic energy functions, with disorientation cut off values of 15 °, 30 °, and 45 °,
above which the grain boundary energy is constant. In each case, an enhancement with
respect to a random distribution of boundaries (Mackenzie distribution) in population is

observed for boundaries with relatively low disorientation angles. A decrease is observed for boundaries with relatively higher disorientation. Figure is reproduced from [7].

For microstructures with initial single component orientation texture, the MDF continuously evolves with grain growth, exhibiting a narrowing distribution that shifts left to lower misorientation angles. There is no steady state behavior. A geometric-based model of boundary lengthening and reconfiguration of triple junctions is proposed as an explanation for the development of anisotropic distributions [7]. Topological events are not considered. This explanation only considers misorientation dependent anisotropy and only accounts for a fraction of the anisotropy observed experimentally when considering the full five parameter-dependent anisotropy. It is likely that grain boundary plane orientation dependent energy anisotropy also influences the evolution of the GBCD; however, little is currently known about this.

Kinderlehrer et al. [44] present results from 2D grain growth simulations that obey the Mullins equations with the Herring condition enforced at triple points. Critical events such as the creation and elimination of boundaries are considered, and anisotropic grain boundary energy as a function of lattice misorientation $[\gamma(\theta)]$ as well as boundary orientation $[\gamma(\alpha)]$ is employed. Simulations considering only $\gamma(\theta)$ reproduce results similar to those already discussed. When $\gamma(\theta,\alpha)$, the GBCD evolution is different. Two causes for development of anisotropy in the GBCD are presented. One process is the annihilation and creation of boundaries resulting from critical events. This will alter both $\lambda(\theta)$ and $\lambda(\alpha)$. This process should occur in each simulation case. The second process is changes in boundary orientation through rotations. This will only affect $\lambda(\alpha)$; $\lambda(\theta)$ will be preserved. Subject to the constraints of triple junctions, boundaries may tend to reorient to lower energy configurations. The distribution is then related to both

interfacial energy and gradients in the energy. It is hypothesized that this causes the differences in the GBCD from the two different simulation conditions. Further support comes from simulations with anisotropic boundary properties but isotropic triple junction configurations (effectively fixing the dihedral angles to be 180 °). In this case, the GBCD is isotropic. These results capture much of the previously reported results while uncovering more information about the evolution of the GBCD by operating within a more realistic framework. Finally it is reported that kinetic/mobility effects are less important than the energy anisotropy in determining the grain boundary character distribution.

To date, only Gruber et al. [46] have applied a full five parameter-dependent energy and mobility [$\gamma(\Delta g, n)$] anisotropy to 3D simulations of grain growth for the purpose of tracking the evolution of the grain boundary plane distribution, $\lambda(\mathbf{n})$. Equal volume partitioning of the five parameter space was employed, similar to previously reported experimental results [10]. For an initially random orientation and GBCD texture, $\lambda(\mathbf{n})$ evolves through an initially transient condition before steady state behavior is displayed. Orientation texture remains random. As in the other simulation results presented, lower energy boundary planes occur more frequently in the steady state anisotropic distribution. In fact, there is clear inverse (although not strictly one-to-one) correlation between energy and population, as in a previously referenced experimental work [10]. Mobility anisotropy is again shown to have little to no effect on the evolution of the GBCD for randomly oriented materials. These results are shown in Fig. 2.4. The implication of this result is that the evolution of the GBCD results from more than just "fast boundaries" moving out of the microstructure.
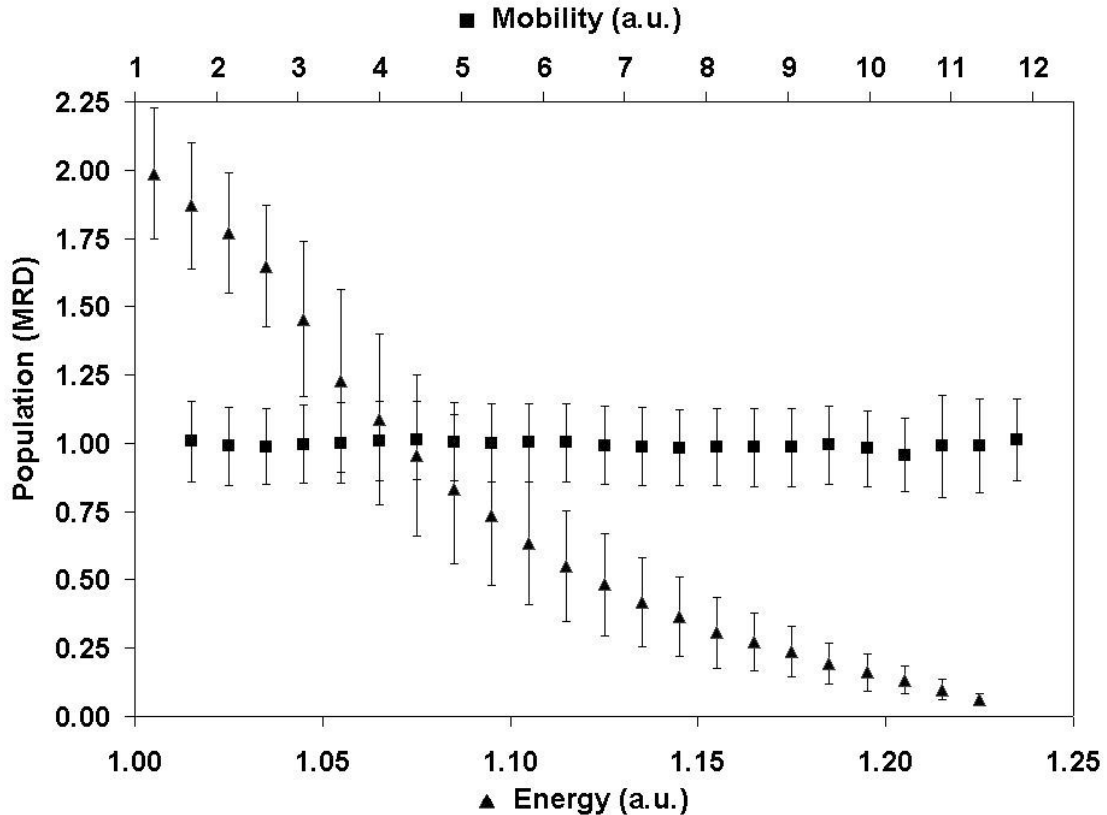
Figure 2.4 The population of grain boundaries with respect to grain boundary energy and mobility for simulated 3D grain growth dependent upon anisotropic grain boundary energy and mobility. In this example, mobility anisotropy is a factor of ten greater than grain boundary energy anisotropy. When anisotropic grain boundary energy is used, the microstructure evolves during grain growth to result in a population of boundaries that is approximately inversely correlated with grain boundary energy. This is consistent with experimental findings. Anisotropic grain boundary mobilities have little effect on grain boundary populations with grain growth. This figure is reproduced from [46].

The main result of all of the reviewed works is the same – lower energy boundaries occur more frequently in anisotropic grain boundary character distributions that result from normal grain growth. Simulation results in 2D and 3D with various energy considerations capture this general feature. For dense microstructures with no orientation texture, steady state behavior of the GBCD during grain growth was identified. Interface energy anisotropy was found to play a much larger role than mobility anisotropy in determining this state. Mobility effects have been used to explain

evolution of the GBCD in liquid containing ceramics. Finally, it is noted that when considering the evolution of the GBCD, it is necessary to account for anisotropic properties that are dependent upon all five macroscopic parameters and to account for changes in the relative numbers of grain boundaries, as well as changes in relative boundary area.

2.6 Influence of Composition on the GBCD

If grain boundary energy anisotropy is the main factor in determining the anisotropy of the GBCD, controlling the grain boundary energy anisotropy should allow for at least limited control of the GBCD. It is widely accepted that segregation of dopants to grain boundaries can change the grain boundary energy. For dopants to be used to control the GBCD, it is of course important to understand the effect of dopant segregation on the GBCD.

Cho et al. [47] investigated the effects of yttria doping on the population of low Σ CSL boundaries in Al_2O_3. In this analysis, grain boundary character is only defined by three misorientation parameters. For 1000 ppm yttria doping in Al_2O_3, there was no significant change in the population of low Σ CSL boundaries. However, Suzuki et al. [48] showed that P segregation in polycrystalline α-iron was correlated to the grain boundary plane character. Switanicki et al. [49] report results for Mg and Ti doped Al_2O_3 that also show that segregation is correlated to grain boundary plane character. These findings, however, do not address how segregation may be affecting the GBPD.

Recent work by Pang and Wynblatt [50] sought to address how dopant segregation affects the GBPD. In this work, the GBPD is reconstructed for a 2 mol %

Nb-doped TiO_2 and is compared to the reconstructed GBPD for an undoped TiO_2 sample. Relative grain boundary energy distributions were determined for each sample. For the undoped TiO_2, the surface energy distribution was determined based on first principle calculations performed by Ramamoorthy et al. [51]. For the Nb-doped TiO_2, the surface energy distribution was determined using a technique based on measuring the geometry of surface thermal grooves formed by diffusion at high temperatures where grain boundaries intersect a planar surface, similar to that of previous work by Saylor et al. [12]. Auger microscopy was used in conjunction with EBSD orientation mapping to measure the segregation anisotropy. Segregation was shown to be correlated with grain boundary energy. There tended to be more segregation to higher energy grain boundaries, and less segregation to lower energy grain boundaries.

To observe the effects of segregation on the GBPD, a stereological procedure [9] was used to determine the GBPD for each sample. In each case, there was an inverse correlation between preferred grain boundary termination planes and grain boundary energy. The maxima in the GBPD in each sample were located at grain boundaries terminated by {110} type planes. For 1000 ppm Nb doping in TiO_2, segregation appeared to increase the anisotropy of the GBCD, as the population of grain boundaries terminated by {110} planes increased from 1.36 MRD to 1.78 MRD. An argument was made to justify how decreasing grain boundary energy anisotropy could increase the GBPD anisotropy; this is certainly a possibility in this case, but may not hold true for all cases. It must also be remembered that the grain boundary energy was determined with two different techniques for the two different samples. Because of this, the result contains some ambiguities that should be addressed with further experimentation.

In this work, the effect of doping on the GBCD will be studied by comparing MgO and Ca-doped MgO. Doping effects on the MDF and GBCD will be studied. It is expected that there will be minimal effect on the MDF with doping, but there will be an appreciable effect on the GBCD. Relative grain boundary energies for both Ca-doped and undoped MgO will be determined using the thermal groove based technique.

2.7 Grain Boundary Engineering to Influence the GBCD

It has been nearly 50 years since Aust and Rutter first experimentally observed special properties of low-Σ CSL boundaries [2] and twenty five years since Watanabe first introduced the phrase "grain boundary design and control" [52]. Since that time, there have been many published examples of gains in materials properties through thermomechanical treatments aimed at changing the grain boundary character distribution (GBCD) in metallic systems with the fcc structure – an approach that has become known as "grain boundary engineering." Iterative thermomechanical processing is a well known method of manipulating the GBCD of face centered cubic metals and alloys. When the repeated cycles consist of relatively small levels of deformation and relatively low temperature annealing, the relative areas of grain boundaries with a $60°$ misorientation around the [111] axis (referred to here as $\Sigma 3$ grain boundaries, according to the coincident site lattice notation) increase while maintaining an approximately constant grain size and a random texture. When this processing improves the bulk properties of the material, it is referred to as 'grain boundary engineering' (GBE). Examples include achieving enhanced resistance to corrosion in nickel-based Alloy 600 and Alloy 800 [53, 54], enhanced

resistance to stress corrosion cracking in nickel-based alloys [55], resistance to creep [56, 57], and increased ductility [58]. In all cases, the results are based on empirically-derived processing conditions and researchers tend to rely on the CSL paradigm and specifically the concept of "special boundaries" (boundaries with specific simple geometries because of symmetry or a relatively high degree of coincidence of lattice sites either in the boundary plane or the lattices of adjacent grains) to explain the results.

Considering the previous conclusions from measuring the GBCD, it is expected that explanations based on misorientation alone will not provide sufficient insight to allow prediction of grain boundary engineering processing. This is emphasized in a recent paper by Randle [59] that calls for a more rigorous definition of what constitutes "special boundaries," and reiterates that not only must the boundary plane orientation be considered, it is also likely that it is the boundary plane, and coincidence confined to the plane, that will be more important in determining "special" properties.

Improvements in properties have been associated with increases in the populations of grain boundaries with the $\Sigma 3$ and $\Sigma 3^n$ (where n is 2 or 3) misorientations and, therefore, the evolution of the misorientation distribution as a function of processing has been well characterized [60]. However, the orientations of the $\Sigma 3$ boundaries introduced by GBE have not been extensively studied. A recent investigation of grain boundary engineered brass indicated that the new $\Sigma 3$ boundaries are mostly coherent twins, where a coherent twin is defined as a pure twist type $\Sigma 3$ interface comprised to two parallel (111) planes on either side of the grain boundary [20]. In this work, we will use the term incoherent $\Sigma 3$ to indicate any $\Sigma 3$ grain boundary whose plane trace is inclined by more than $10°$ from the ideal coherent twin orientation. One purpose of this work is to

determine the characteristics (crystallographic orientation) of the $\Sigma 3$ grain boundaries introduced by the grain boundary engineering process in Ni, and how they affect the structure of the grain boundary network.

A recent systematic study by Schwartz et al. [61] compares several processing routes for oxygen free, electronic grade (OFE) Cu. While the results are again interpreted within the CSL framework, extensions are made that acknowledge that misorientation alone is not enough to account for property observations. In particular, the $\Sigma 3^n/\Sigma 3$ ratio is referenced as an important characteristic of a microstructure. This ratio is shown to increase with GBE. They report experimental results that support the belief in sequential thermomechanical processing as a means for increasing "special" boundaries (in this case CSL $\Sigma 3^n$ boundaries, where $n = 1, 2,$ or 3), even though they fail to consider boundary plane orientation. It was also found that the "grain boundary engineered" state that is achieved is relatively stable with grain growth. In the current work, sequential thermomechanical processing will be employed and full five parameter characterization of the GBCD will be completed as a means of determining which boundaries truly are "special" with respect to energy and population and how these boundaries influence the evolution of the GBCD and the connectivity of the network.

Chapter 3

3. Experimental Characterization of the Evolution of the Grain Boundary Character Distribution

3.1 Introduction

In this chapter, experimental techniques used to track the evolution of the grain boundary character distribution during grain growth in $SrTiO_3$ and the effects of sequential thermomechanical processing on the GBCD of commercially-pure and high purity nickel will be described. Doping is explored as a technique for influencing the GBCD in MgO. Semi-automatic orientation mapping in an SEM, coupled with stereological techniques, will be employed as a method for determining the GBCD. Sample preparation is discussed. A quantitative study of the experimental uncertainties of this technique is presented. Atomic force microscopy is discussed as a technique for determining relative grain boundary energy anisotropy.

3.2 Measuring the Grain Boundary Character Distribution

To measure $\lambda(\Delta g, \mathbf{n})$, it is first necessary to measure the local orientations of many grains in a polycrystalline sample. Orientation maps can be collected from planar surfaces using electron backscattered diffraction mapping (EBSD) in a scanning electron microscope (SEM) [62]. When an electron beam is focused on a crystalline material, electrons are scattered in all directions. Optimal efficiency for the backscattering effect

occurs when the beam is at a low, glancing angle with respect to the surface. In practice,

a sample is tilted to approximately 60º- 70º with respect to a focused electron beam. Fig.

3.1 demonstrates the microscope geometry as used in this work.
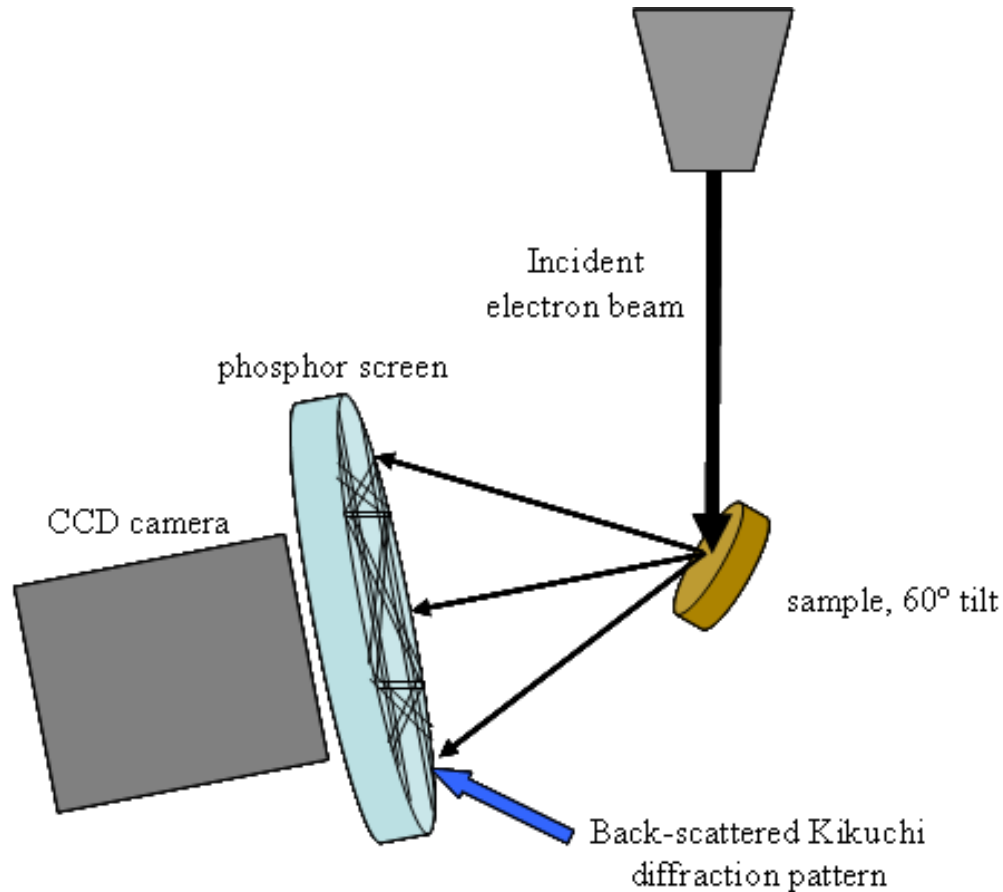
Figure 3.1 A schematic is shown of the experimental setup used in this work for EBSD orientation mapping in a Phillips XL40 SEM.

'Kikuchi' [63] diffraction patterns are formed and projected onto a planar detector. The

beam can be programmed to raster a regular grid covering an area on the surface of the

sample. In this work, all data was collected on a hexagonal grid. Patterns are collected at

each point and crystal orientations are assigned to each pixel as a result of

matching/voting routines based on ideal lattice parameters. A sample orientation map for

a $SrTiO_3$ is shown in Fig 3.2. This map is a [001] inverse pole figure map, where crystal orientations with respect to the sample normal are color coded with respect to the standard stereographic triangle legend on the right.
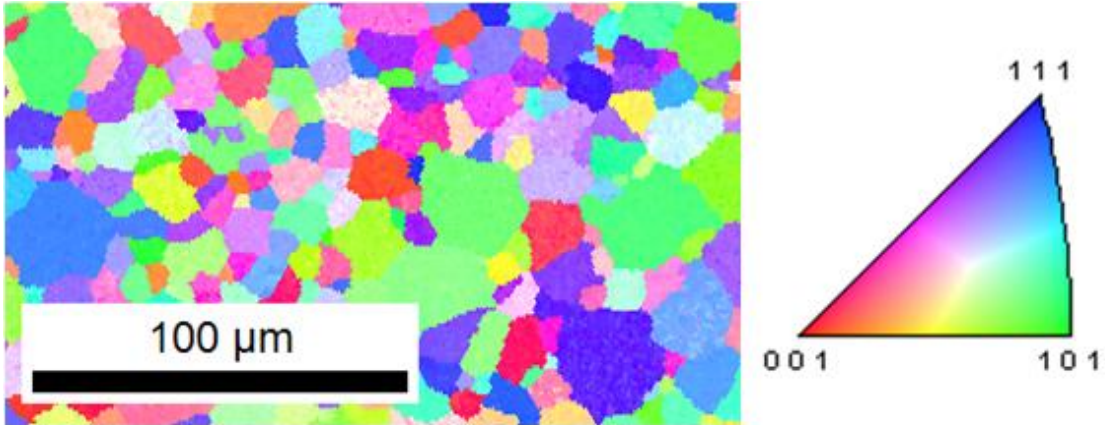
Figure 3.2 A [001] color coded inverse pole figure map, generated with TSL/OIM ver. 4.6, of a strontium titanate polycrystalline sample. Grain orientations with respect to the sample normal are colored according to the standard stereographic triangle on the right.

For all of the experimental results presented in this work, TSL/OIM (TSL/EDAX) orientation mapping software, coupled with a Phillips XL40 FEGSEM, was used. Data analysis was performed using TSL/OIM versions 4.5 and 4.6.

From these maps, it is possible to determine four of the five parameters required to describe the GBCD. The misorientation between grains accounts for three parameters, and the in-plane boundary orientation accounts for the fourth. The only unknown parameter is the boundary inclination with respect to the section plane. Calibrated serial sectioning [10, 11] and more recently focused-ion beam milling [64] can be used to explicitly determine boundary inclinations, but are experimentally challenging. A stereological procedure has been developed to estimate the distribution of boundary types in the interfacial network based on observations from a planar section [9]. This

procedure is an extension of a stereological approach for boundary planes described by

Hilliard [65] and Adams [66]. In-plane observed grain boundaries are discretized into

boundary segments that are associated with the adjacent grains. While the true

inclination of the boundary cannot be determined from the planar observation, it is known

that the direction of the boundary segment is the pole of a family of possible boundary

planes. After accumulating many observations on the same type of bicrystal in different

orientations with respect to the sample reference frame, the true boundary plane should

comprise a relatively larger fraction of the accumulated data. After subtraction of the

background of randomly contributed observations, the true grain boundary plane

distribution remains. Details of the subtraction routine can be found elsewhere [9].

Several versions of the reconstruction software, each with minor differences, exist. For

this work, version 12/12/2007 is used throughout.

3.3 Quantifying Experimental Uncertainties in Stereological GBCD Determination

Before using a stereological based technique to quantitatively compare GBPDs

for the same material, it is necessary to quantify potential sources of experimental

uncertainty. Knowledge of the experimental variability of the technique allows for

definition of data collection parameters required to minimize errors and facilitate fair

comparison between measured GBCDs. A threshold below which measured differences

are indistinguishable from experimental errors can also be identified.

3.3.1 Orientation Mapping for Stereological GBCD Determination

The core of the stereological technique for GBCD determination is orientation mapping. From hexagonal-grid orientation maps, reconstructed grain boundary segments are extracted that contain misorientation and in-plane boundary plane orientation information. These segments are then used for the stereological reconstruction of boundary inclination information. Obviously, the quality of the orientation information is important to this technique.

Orientation mapping is a grid-based, discrete technique. For stereological GBCD determination, a hexagonal grid is used. Kikuchi patterns are collected and indexed for each pixel of the grid, building an orientation map of the grains on the sample surface. The quality of these patterns, and thus of the indexing, is primarily determined by surface preparation. However, there is often a time dependence to the pattern quality as well. Because of the large amounts of data required for the stereological technique, collection speed should be maximized. It is not necessary, though, or desired, to correctly index the Kikuchi pattern collected for every pixel of the grid. In fact, even for the slowest of collection speeds, it is often impossible to correctly index the pattern at every pixel. Instead, there are a variety of data clean up procedures that enable the correction of un-indexed or mis-indexed pixels. Of course, there is a limit to the amount of correction that should be done to a data set. As such, there must be a balance between data collection speed versus required data quality. This is a subjective determination that must be made by the experimenter. In this work, the desired quality was such that no more than approximately 15 % of the points in a given orientation map should require correction.

As an example, the clean up of a representative $SrTiO_3$ sample data set is detailed. A typical [001] IPF orientation map of raw data is shown in 3.3a.
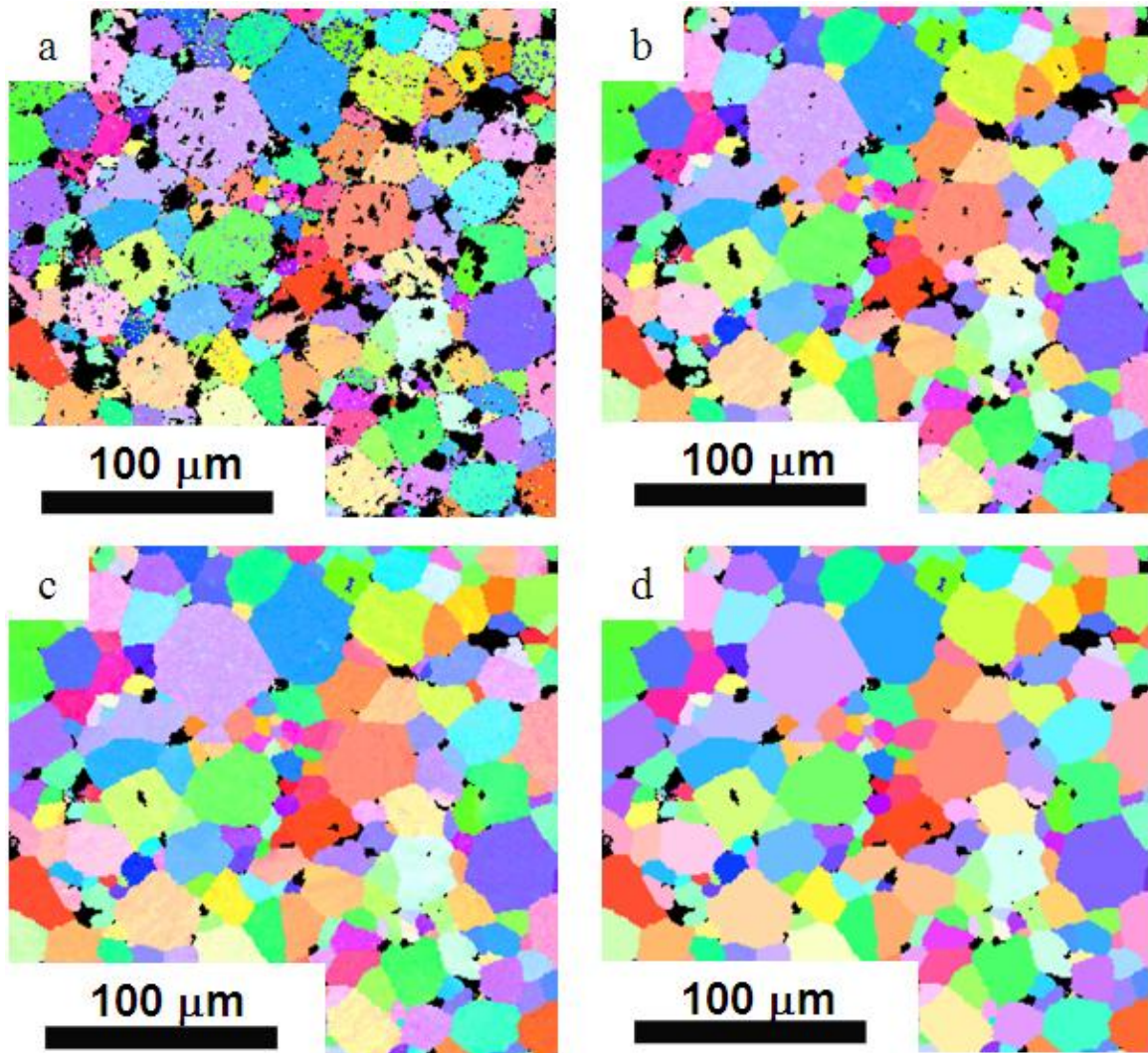
Figure 3.3 A series of [001] inverse pole figure orientation maps for $SrTiO_3$ representing a typical multi-step data clean up procedure for raw orientation mapping data. (a) The data in raw form. (b) The data after a single pass of grain dilation clean up. Less than 10 % of the data is changed from state (a) to state (b). (c) The data after a second pass of grain dilation clean up. Less than 3 % of the data was changed. (d) A map of the data after a single average orientation is assigned to each grain.

In this case, grain dilation was chosen as the initial clean up method. In this method, pixels are assigned to grains based on a misorientation tolerance and minimum cluster size. All pixels that do not belong to a grain based on these parameters are allowed to change orientation to that of the nearest grain, either in single or multiple iterations. The map in Fig. 3.3b represents the raw data (Fig. 3.3a) that was processed with single iteration grain dilation. Single iteration was chosen so that real pores located on grain boundaries in the material did not end up being represented by imaginary orientation information. There was a $5°$ misorientation tolerance and grains were chosen to be a minimum of ten pixels in size. Approximately 9% of the data was changed with this clean up procedure. Much of the changed data was located within the bulk of grains and not at boundaries. At this point, a second single iteration grain dilation with the same parameters was performed. This time, less than 3% of the data was changed. These points are not necessarily independent of the points changed in the initial dilation clean up. Thus, it is not accurate to assume that a total of 12 % of the data has been changed. 12 % represents the maximum amount of change that may have occurred for the data clean up of this specific area. The true test of the efficacy of the clean up procedure comes from comparing the first iteration to the second iteration. Relatively small change in the second iteration shows that data clean up has been performed sufficiently and judiciously. In fact, comparing microstructural characteristics such as grain size after one and two iterations of grain dilation shows minimal differences. Fig. 3.3c shows an [001] IPF map of the resultant data. Finally, an average orientation is assigned to each grain (Fig 3.3d). These clean up parameters were chosen after inspection of the data and will vary from experiment to experiment. The results in this work are based on large datasets

which are comprised of many individual orientation mappings. However, the clean up procedure is constant for a given data set.

Next, digital representations of grain boundaries are created. A procedure known as "grain boundary reconstruction," described by Wright and Larsen [67], is used. In this procedure, the TSL^{TM} software first groups pixels of like orientation together as grains, based on misorientation and minimum pixel cluster size tolerances input by the user. The software then identifies triple junctions, which in this case are hexagonal lattice nodes that are surrounded by three pixels from adjacent distinct grains. Then, triple junctions are logically connected to estimate in plane grain boundary geometry. First, straight segments are used to connect triple points. If these segments deviate from the boundary position by more than a specified number of pixels, the segments divide to better match the curvature of the boundary. The minimum deviation for division is two pixels; a one pixel deviation would merely result in a saw tooth representation of the boundary, which would not accurately represent grain boundary plane geometry. An example of a reconstructed grain boundary is shown in Fig. 3.4.
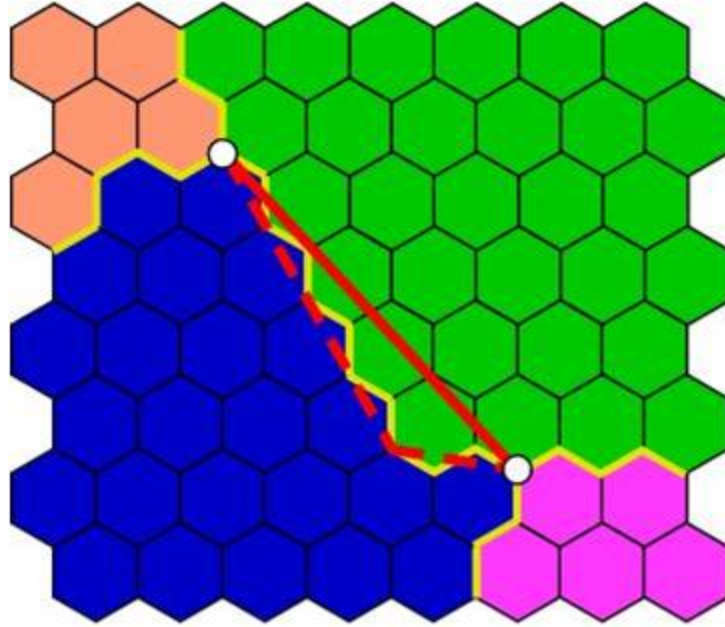
Figure 3.4 Schematic of a reconstructed boundary created with TSL^TM software (from TSL help files). Triple junctions are connected with a straight line, and the maximum deviation from the recorded boundary position is calculated. If the segment deviates from the recorded boundary position by more than the maximum, the segment will divide to more accurately represent the boundary curvature. With a default maximum deviation of two pixels, the boundary will not divide.

The solid red line represents the initial grain boundary segment used to connect two adjacent triple points. The dotted red line shows a potential division of the reconstructed boundary to match the curvature of the boundary. As the minimum deviation of the reconstructed segment from the actual boundary position is two pixels, this segment will not divide.

The accuracy of the determination of in plane grain boundary geometry is obviously important for accurate stereological GBCD determination. Fig. 3.5 shows reconstructed boundaries with a maximum deviation of two pixels plotted for the cleaned SrTiO$_3$ example orientation map from Fig 3.3d.
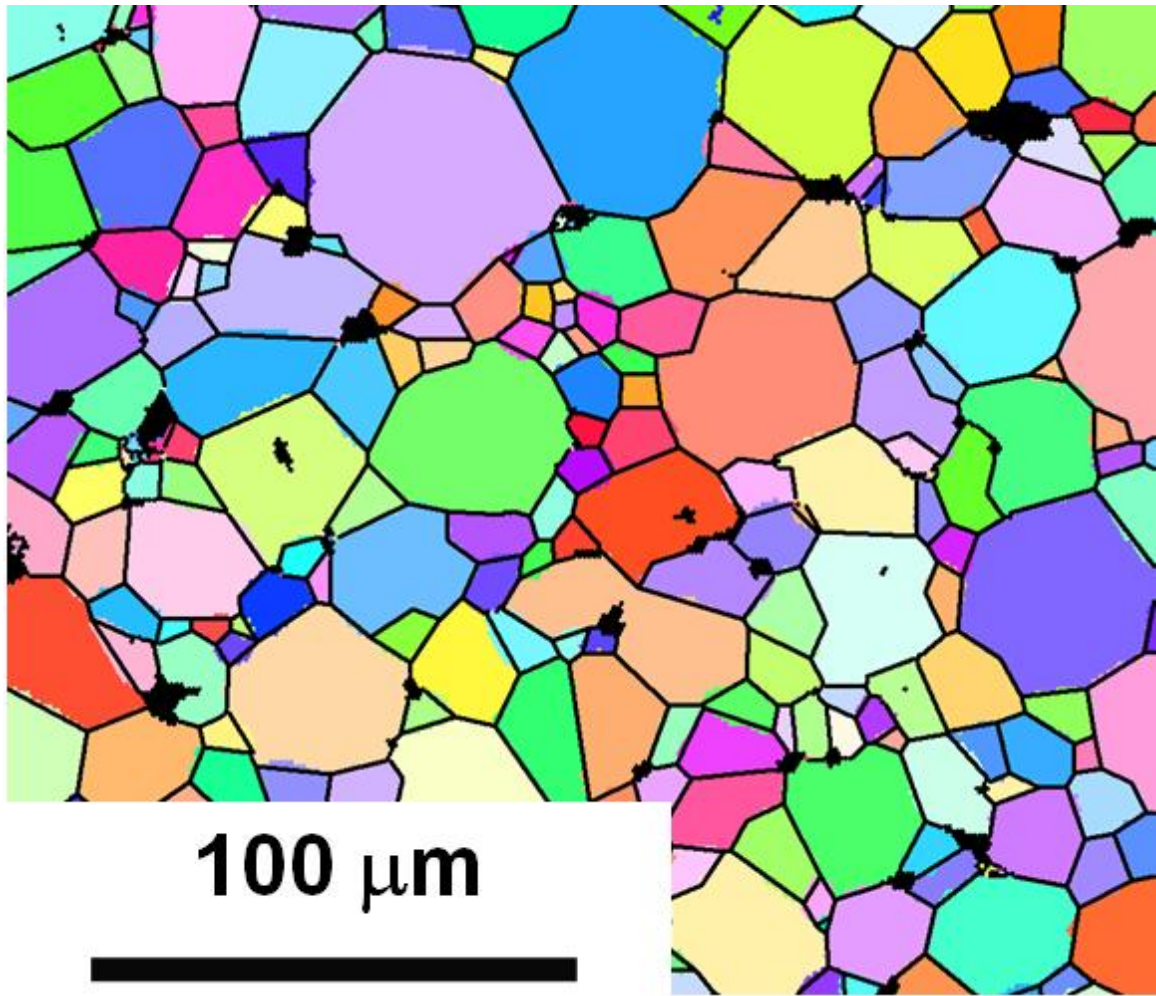
Figure 3.5 A cleaned $SrTiO_3$ data set plotted as an [001] inverse pole figure with reconstructed boundaries as bold black lines. The reconstruction procedure is not exact, but guidelines can be established to ensure minimal effect upon the stereological GBCD reconstruction.

There are obvious grain boundaries where the reconstructed boundary does not exactly trace the mapped grain boundary. The importance of such errors will depend upon the resolution of the GBCD calculation. The effect of these errors, and any other systematic errors in the stereological reconstruction of the GBCD, will be addressed in the following sections. Guidelines for minimizing the effects of these errors will be established.

3.3.2 Uncertainties Associated with GBCD Reconstruction

It is useful to first explore inherent errors in the stereological determination of the GBCD. To estimate errors associated with the reconstruction technique, a random (isotropic) GBCD was used as a test case. Beginning with a simulated random GBCD, 100,000 grain boundary segments that were consistent with the GBCD were generated. These boundary segments were then used as input for the stereological reconstruction method. A perfect reconstruction method should result in the output of a reconstructed GBCD the same as the random target GBCD. Instead of a perfectly random GBPD, the result was a calculated GBPD that exhibited approximately 10 % anisotropy, with a maximum at {100} type boundary planes. This result is plotted in units of multiples of a random distribution (MRD) on the stereographic projection in Fig. 3.6. In this case, 10 % anisotropy amounts to 0.1 MRD. For real materials, a 10 % error will likely represent a value in MRD greater than 0.1.
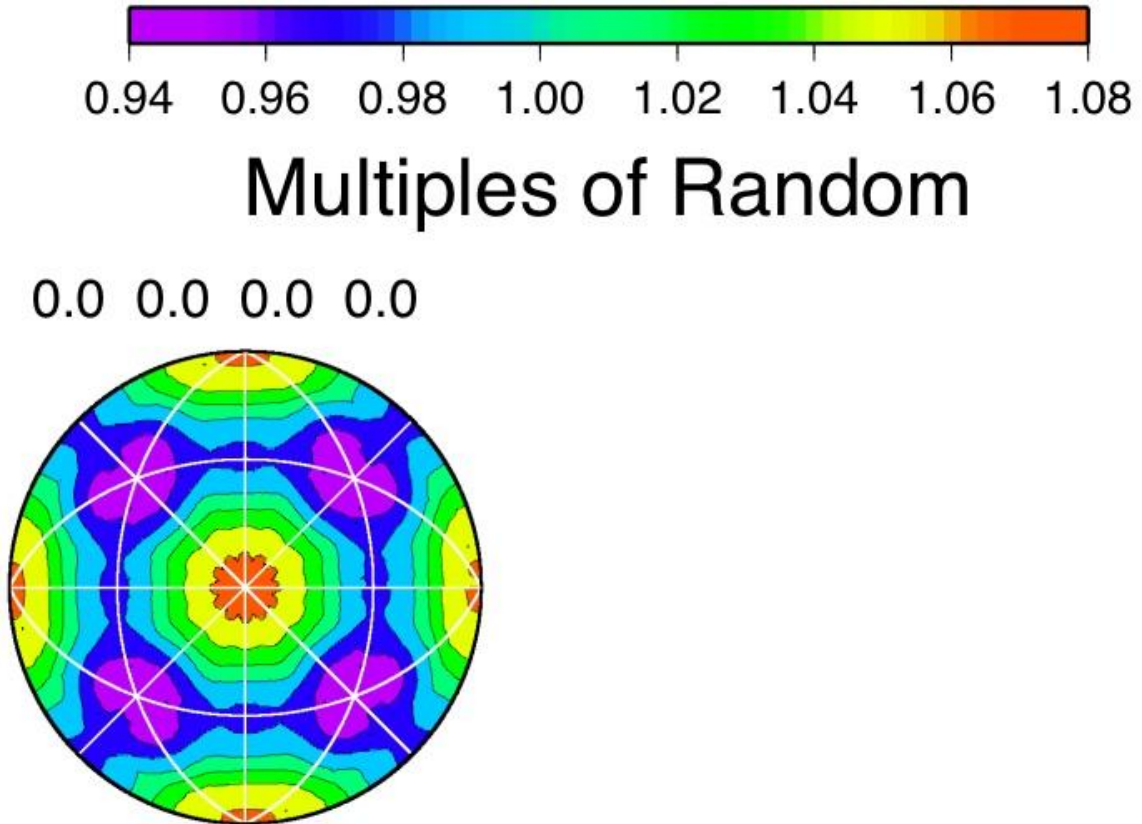
Figure 3.6 Stereological reconstruction of the GBPD for a simulated isotropic GBPD. The reconstructed GBPD exhibits approximately 10 % anisotropy, showing an inherent bias in the stereological technique. Experimental work will require that a stereologically reconstructed GBPD should vary more than 10 % from random before being considered as an anisotropic distribution.

As a result, it has been determined that it is incorrect to interpret GBPDs that deviate less than 10 % from random, as these differences cannot be separated from inherent bias in the technique. Anisotropies greater than 1.1 MRD are likely to be real, whereas anything less cannot be interpreted, especially if the distribution peaks for {100} planes. This bias will also show up in the determination of truly anisotropic distributions and will have a varying effect on the observed GBPD depending on the symmetry of the material and the position of local maxima in the distribution with respect to "false" maxima observed because of bias. Similar but likely more complicated effects should be

observed for the situation of determining the five parameter GBCD; however, quantitative evaluations of such effects are still required. It was assumed that since 50,000 segments were sufficient to minimize the error in previous calculations of the five parameter GBCD, 100,000 boundary segments should be sufficient to accurately determine the two parameter GBPD. This assumption will be tested in the next section.

3.3.3 Effect of Number of Observations on the Stereological GBPD Reconstruction Technique

The stereological technique has been validated by computing the GBCD for a simulated microstructure with a known GBCD, and through comparison of stereological and serial-sectioning based determinations of the GBCD for $SrTiO_3$ [11]. It was shown that the accuracy of the technique depends on the number of observations made. 95 % of quantified errors are less than 0.6 MRD and do not substantially change for greater than 50,000 observations for cubic materials at a resolution of 10 °. Generally, the technique reproduces trends from the true GBCD but underestimates peaks in the true GBCD because of binning/averaging effects and because of subtraction bias near peaks. It should be noted that the technique requires the sample to have little to no orientation texture, or results may be biased. It is expected that more observations will be required for materials that have a high level of anisotropy in the GBCD, such as for the case of nickel that has a high population of coherent twin boundaries. To ensure statistical significance with the stereological technique, all boundary types need to be sampled with statistical significance. The guidelines for the number of required observations assume that all misorientations are equally represented. For the case of Ni, which twins

extensively, more than 50 % of the boundaries may be of the coherent twin type. Thus, more measurements will be required to ensure that all boundary types are being sampled sufficiently and many more than 50,000 boundaries will have to be sampled.

These considerations will be used as guidelines when determining the GBCD. It is also necessary to quantify inherent biases in the technique and to determine the effects of the number of observations on the calculation of the misorientation independent grain boundary plane distribution. It is expected that because of the averaging used in this technique, fewer observations should be required for a consistent answer.

To quantify the number of observations required to consistently determine the misorientation-independent GBPD, calculations were performed to show the variation in the reconstructed GBPD with respect to the number of observations included. For this analysis, The GBPD was calculated for an increasing number of boundary segments from the previous simulated isotropic case. The first N lines of the data set (where N = 500, 1,000, 2,000, 10,000, 20,000, 25,000, 50,000, or 75,000) were used to calculate the reconstructed GBPD and the maximum and minimum in the distributions, in units of MRD, were recorded and plotted as a function of number of segments. Fig. 3.7 shows that the maximum and minimum values of the GBPD distribution are nearly constant for datasets of 10,000 segments or larger.
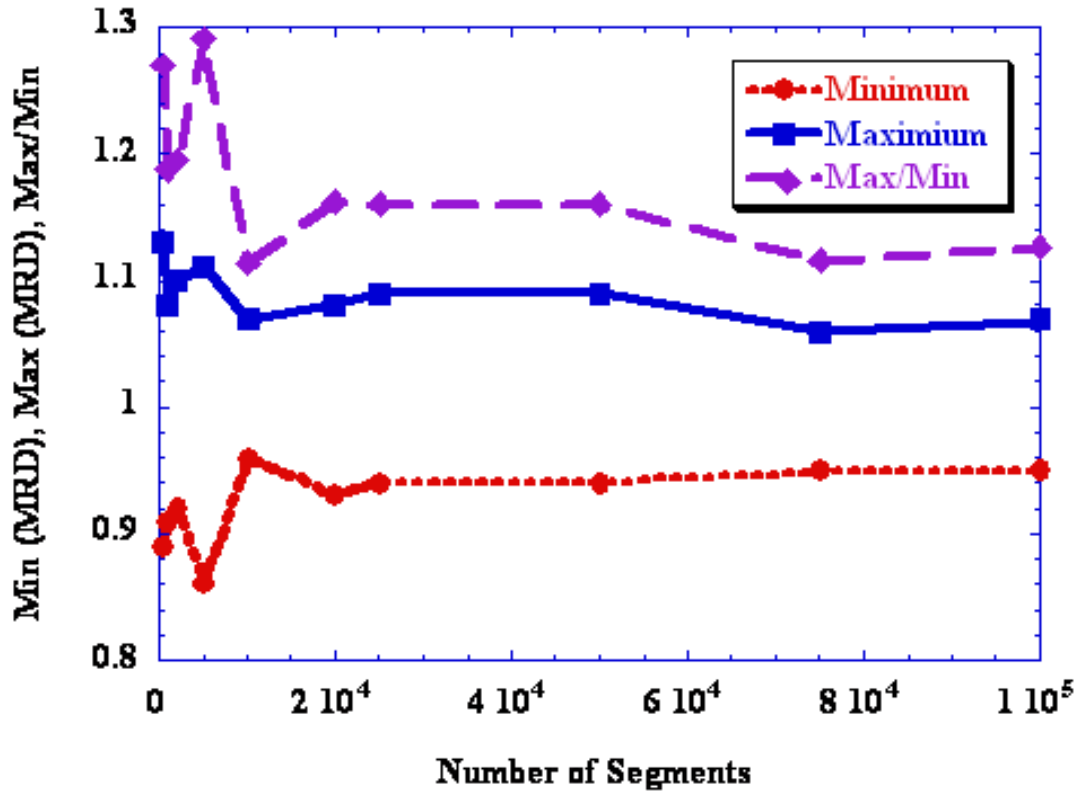
Figure 3.7 The maximum (MRD), minimum (MRD) and maximum/minimum ratio of the GBPD with respect to the number of reconstructed boundary segments used in the stereological procedure for a simulated random GBPD. Anisotropy is observed as described in Chapter 3, Section 3.2. The anisotropy is minimized for an increasing number of observations, until it remains relatively constant when more than 10,000 segments are used.

A similar analysis was performed for an anisotropic grain boundary character distribution. A simulated anisotropic GBCD was created and the grain boundary plane distribution was calculated for an increasing number of simulated grain boundary segments that were consistent with the simulated GBCD. The simulated GBCD was created such that it mimicked the previously measured GBCD of $SrTiO_3$ [11]. A preferred misorientation and associated amplitude, along with a preferred boundary plane orientation and associated amplitude were chosen. The value for a given bin in the five

dimensional GBCD is then calculated based on the proximity of the given bin to the

chosen preferred MDF and boundary plane orientation, according to Eqns. 3.1 and 3.2.

In these equations, a_i is the MDF component of the GBCD, determined only by the

misorientation, θ_{mis}, from the preferred misorientation, the chosen amplitude of the

misorientation preference, A_{mis}, and the chosen width of the spread of the peak, W_{mis}.

This value is then used to calculate the value of a given bin, V, based on Eqn. 3.2. In

Eqn. 3.2, the variables A, θ, and W, have similar meanings as in Eqn. 3.1, except they

now refer to deviation from the chosen boundary plane orientation, amplitude of the

chosen peak, and width of the chosen peak. In both Eqn. 3.1 and 3.2, "amplitude" does

not equate directly to MRD values, but is related.

$$a_1 = 1 + A_{mis} \bullet \exp(-(2\theta_{mis}/W_{mis})) \qquad \textbf{Eqn. 3.1}$$

$$V = a_1 + a_1(A_{plane} \bullet \exp(-(2\theta_{plane}/W_{plane})) \qquad \textbf{Eqn. 3.2}$$

For this example, $A_{mis} = 10$, the chosen favored misorientation is a 2 ° rotation

about [100], and the width of the peak is 10 °. $A_{plane} = 400$, the chosen favored boundary

planes are {100}-types, and the width of the peak is 10 °. Next, simulated reconstructed

boundary segments, consistent with the simulated GBCD, were created. To simulate

reconstructed boundary segments, random segment lengths are selected and assigned

associated misorientations and boundary plane orientations consistent with the simulated

GBCD. The in plane orientation of the segment is determined from the intersection of a

randomly selected section plane with the grain boundary plane. Segments are then

constrained to begin and end on lattice nodes or triple junctions and must fit on a 50x50

lattice. It was assumed that this grid size was more than sufficient to mimic experimental

results. This assumption will be tested in Chapter 3, Section 3.4. The reconstructed

GBPD was then calculated for an increasing number of reconstructed boundary segments.

A plot of the misorientation-independent, GBPD of the ideal function, along with the

reconstructed GBPD calculated with 10 ° resolution from 50,000 boundary segments, is

shown in Fig. 3.8. As seen in Fig. 3.8, the resultant function is sharply peaked for {100}-

type boundary planes. The reconstructed GBCD does not succeed in reproducing large

anisotropies, but does reproduce the general trend and is similar to the observed GBPD of

the earlier $SrTiO_3$ work [11].
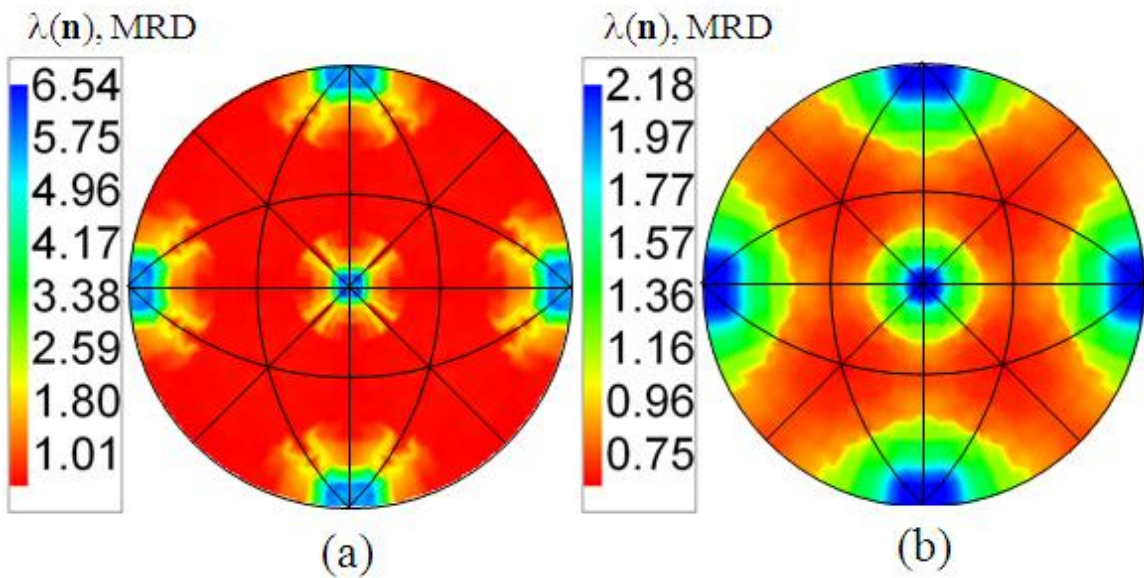
Figure 3.8 Misorientation-independent GBPD for a simulated, $SrTiO_3$-like GBCD (a) and for the reconstructed GBCD calculated with 10 ° resolution based on the simulated function (b). The reconstruction process is unable to capture the sharpness of the simulated GBCD because of averaging as a result of the resolution of the calculation, but does reproduce the general trend of boundary planes terminated by {100}-type planes being favored.

Results plotted in Fig. 3.9 show that after approximately 20,000 segments, the

anisotropy of the reconstructed GBPD varies by less than 10 %. From this result, and the

one plotted in Fig. 3.7, we conclude that for quantitative comparisons of several
experimentally determined grain boundary plane distributions, at least 20,000
observations should be made. In addition, similar analysis should be made for each
individual dataset to ensure that sufficient observations are being used for reliable
determination of the GBCD and GBPD.
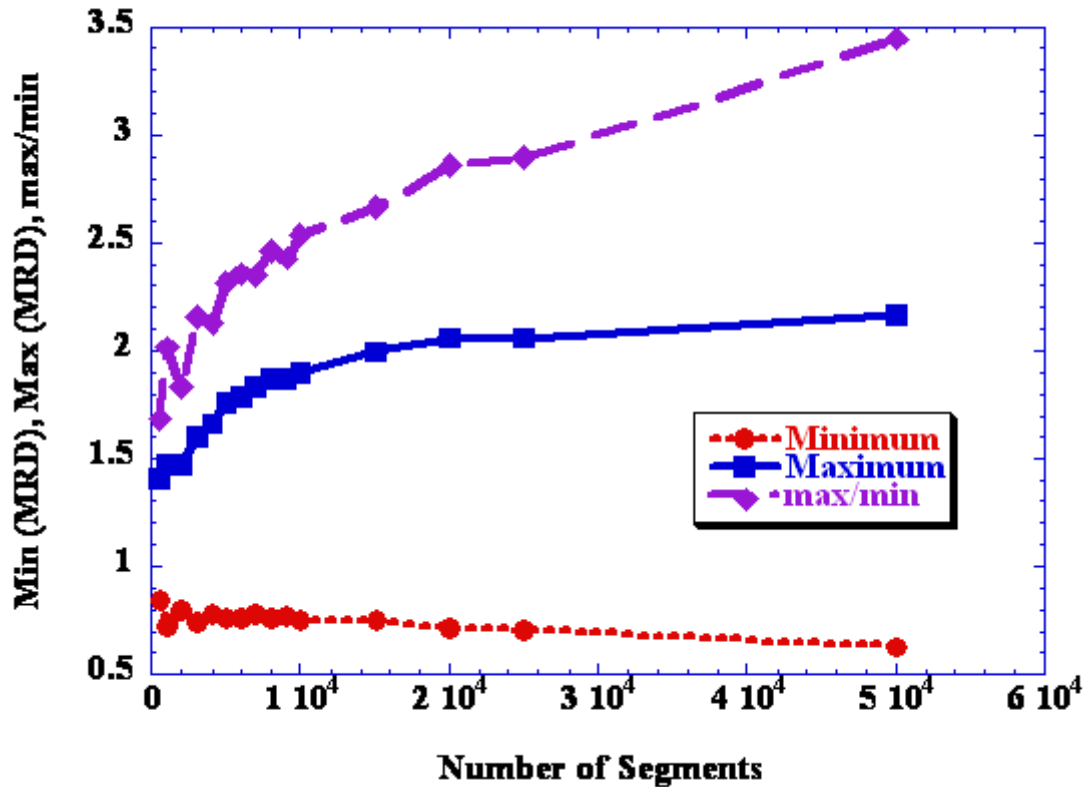
Figure 3.9 The minimum, maximum, and maximum/minimum ratio of the GBPD for a
simulated anisotropic GBCD with respect to the number of segments used in the
stereological calculation. Results based on a small number of segments appear
marginally anisotropic. Anisotropy is observed to increase with increasing number of
segments used to calculate the GBCD until approximately 20,000 segments. Observed
anisotropies differ by less than 10% for greater than 20,000 segments used.

The maximum/minimum ratio appears to be continually increasing with an increasing number of segments used in the calculation. However, the ratio is overly sensitive to small decreases in the minimum value. Thus, differences in the absolute maximum and minimum values are a much more reliable indicator of experimental differences.

3.3.4 Determination of In-Plane Grain Boundary Geometry Using EBSD Orientation Mapping

Orientation mapping with EBSD is a discrete, grid-based technique. In the current work, grain boundary segments are extracted from the hexagonal grid orientation maps. Hexagonal gridding of orientation maps is required for the identification of triple points. As a result, the accuracy of the estimation of in-plane geometry of grains is dependent upon the resolution of the orientation map with respect to the average grain diameter [67]. Observed geometries are constrained by the limitation that reconstructed boundary segments must begin and end on lattice points. This constrains observed in-plane dihedral angles. As an example, a hypothetical grain boundary is super-imposed upon 3x3, 5x5, and 10x10 hexagonal grids in Fig. 3.10. In this example, the black line represents the true location of a boundary, and the red line represents the nearest possible reconstructed boundary segment that begins and ends on a lattice triple junction. This simplistic example is merely meant to show that the variation of the length and position of a reconstructed boundary segment from the true in plane geometry of the grain boundary can increase significantly as the grid resolution decreases.
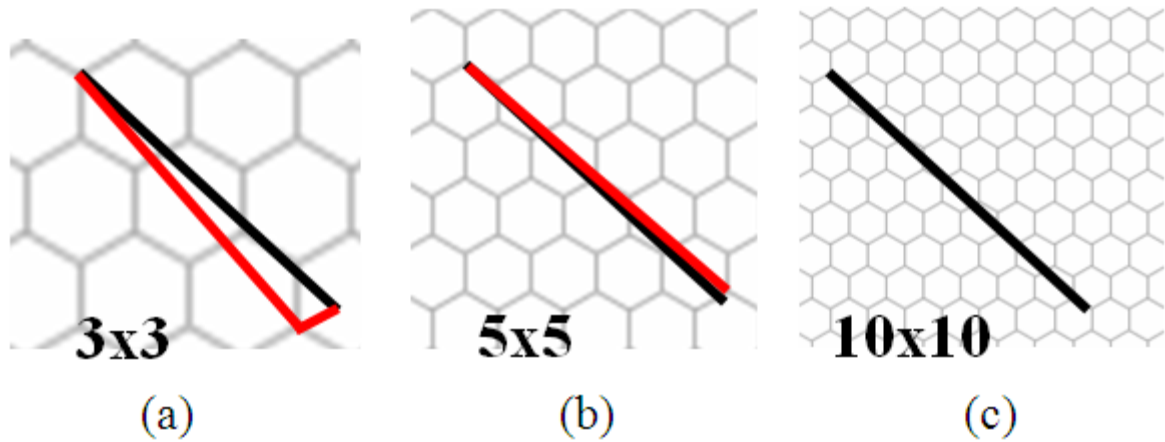
Figure 3.10 The same hypothetical grain boundary is plotted as a black line on a 3x3, 5x5, and 10x10 hexagonal grid. The red lines represent a likely reconstructed boundary segment that must begin and end at grid triple points. The deviation from the true in plane boundary geometry can be larger for lower resolution gridding.

Grid resolution with respect to segment length also constrains the angular resolution of reconstructed boundaries. It is possible to calculate the minimum resolvable angle based on segment length in terms of grid steps. A simple schematic, again based upon 3x3, 5x5, and 10x10 grids, is shown in Fig. 3.11. The minimum resolvable angle will be one-half of the open angle, which is defined as $\tan^{-1}(1/l\sqrt{3})$, where l is the length of the segment in terms of grid steps. In this example, for the same physical length segment, the minimum angular resolution of the segment when placed on a 3x3 grid is 5.45 °, compared to 3.3 ° for a 5x5 grid and 1.65 ° for a 10x10 grid.
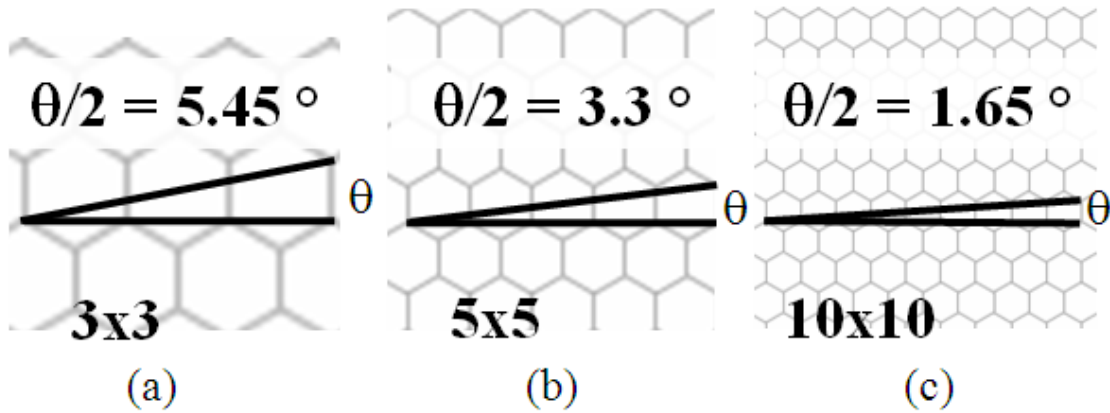
Figure 3.11 Schematic showing the minimum resolvable angle for a reconstructed boundary segment with length measured in terms of grid steps. The angular resolution increases for increasing grid resolution of a segment of a given physical size.

To test the effect of this factor on the determination of the GBPD, the same simulated GBCD described in Chapter 3, Section 3.3 was used. 50,000 segments, constrained to hexagonal lattices of 3x3, 5x5, 10x10, and 50x50, were generated based on this simulated GBCD. Simulated data sets were generated as described in Chapter 3 Section 3.3. From these segments, the GBPDs were calculated as a function of lattice size and the maximum and minimum values of the distributions were recorded. In Fig. 3.12, it is seen that for grid sizes of 10x10 pixels and larger, the ratio of maximum to minimum of the distribution remains within 10 % deviation. GBPDs calculated for segments on grids smaller than this tend to underestimate the anisotropy of the distribution.
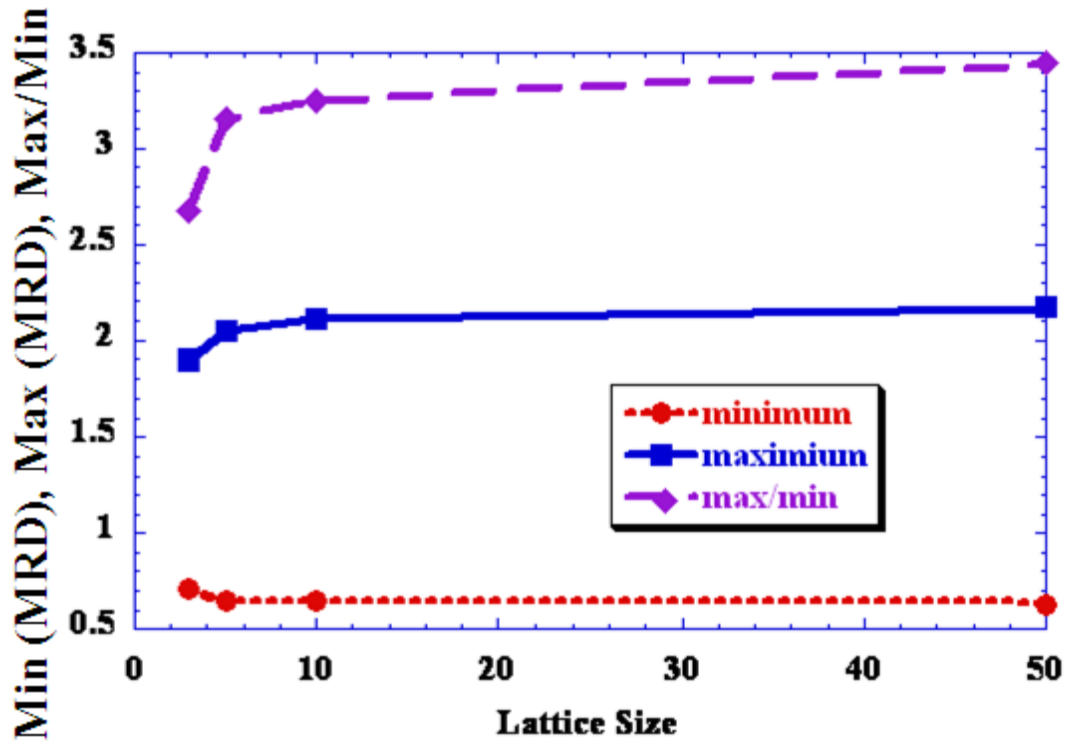
Figure 3.12 Minimum, maximum, and maximum/minimum ratio of the reconstructed GBPD calculated for simulated reconstructed boundary segments based upon a simulated anisotropic GBCD and constrained to 3x3, 5x5, 10x10, and 50x50 lattices. Anisotropy in the GBPD, as quantified by these values, is constant for lattices 10x10 or larger.

It is useful to test this effect experimentally as well. If we consider an equiaxed microstructure, there will be a grain size distribution. It is thus necessary to quantify the "constrained grid" effect on the calculation of the GBCD with respect to the average grain size of a real microstructure.

An experimental test of this effect involved the measurement of the grain boundary plane distribution for a $SrTiO_3$ sample of fixed area with varying orientation map step size. A grain orientation map of area approximately 0.4 mm^2 was collected using the OIM system with a 0.5 μm step size. At this lateral resolution, 3,176 grains with an average diameter of 11.4 μm were identified. Approximately 11,400

reconstructed grain boundary segments were extracted using the OIM software. At this resolution, the step size/average grain diameter ratio is approximately 1:23. This dataset was then sampled, discarding points to result in an orientation map of the original area with an effective 1 μm step size resolution. It is expected that as a result of this procedure, some small grains that were originally identified may be lost. At this resolution, 2,945 grains with an average diameter of 11.9 μm were identified. This reflects a 7 % loss of observed grains. The step size/average grain diameter ratio for this case is 1:12. Approximately 9,000 reconstructed grain boundary segments were extracted. The dataset was then sampled one more time, resulting in an orientation map with an effective step size of 2 μm. At this resolution, 2,389 grains with an average grain diameter of 13.6 μm were observed. This represents a 25 % loss of original observed grains. The step size/average grain diameter is 1:7. 6,900 reconstructed grain boundaries were extracted. Representative IPF orientation maps of the three datasets are shown in Fig. 3.13. Each of these maps represents approximately 1/16th of the total scanned area. There are many observable instances of smaller grains no longer being identified with decreasing resolution. Eliminating the relatively small reconstructed boundary segments associated with these grains will likely have little effect on the calculation of the reconstructed GBCD. However, triple point locations will be determined with decreasing accuracy as a result of these "missing" grains, which will affect GBCD determination.
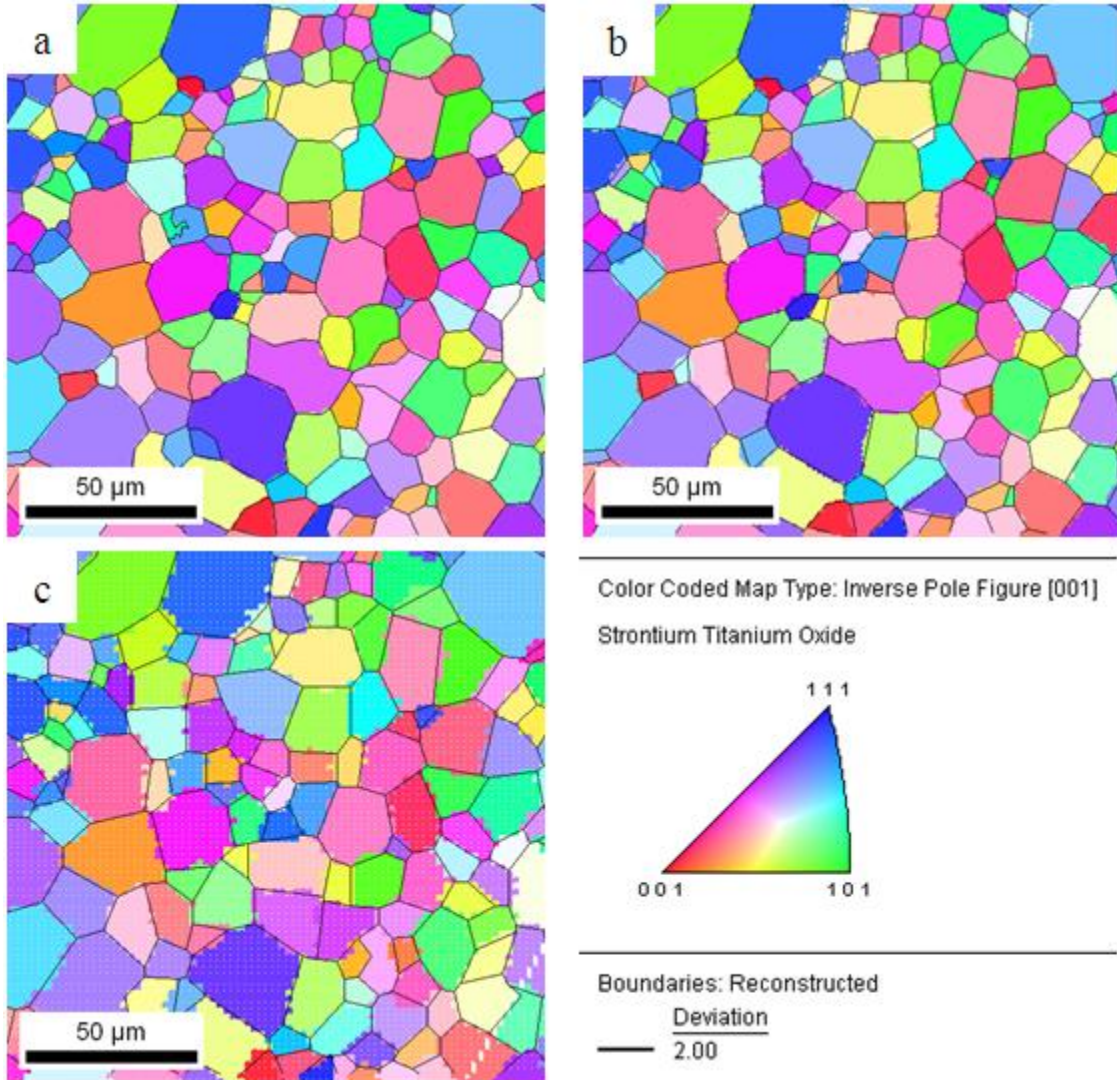
Figure 3.13 Representative IPF orientation maps of the 0.5 μm (a), 1.0 μm (b), and 2.0 μm (c) datasets, with grain orientation with respect to the sample normal colored according to the legend. With decreasing resolution, the effective loss of relatively smaller grains is observable. Reconstructed grain boundaries are increasingly comprised of single straight lines which do not accurately represent boundary curvature or position.

The misorientation independent grain boundary plane distribution was calculated for each dataset. Populations are plotted in units of multiples of a random distribution (MRD) on stereographic projections below, in Figs. 3.14 a, b, and c respectively.
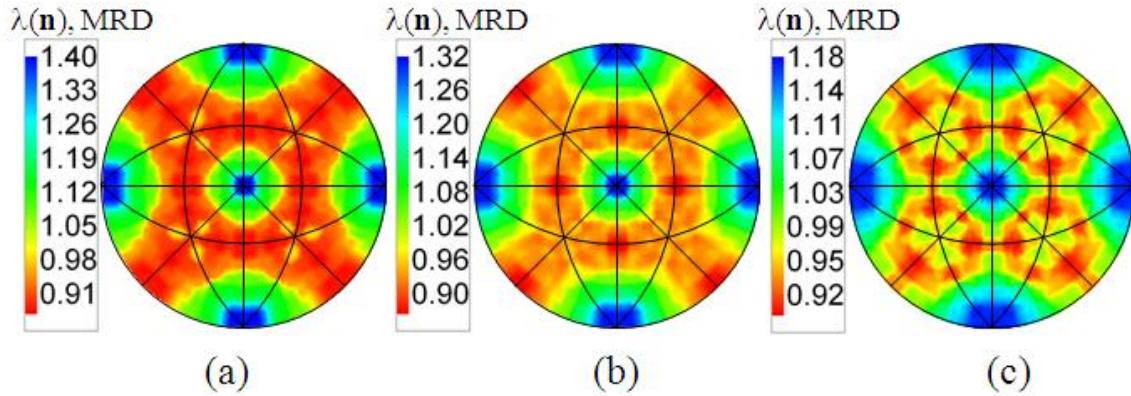
Figure 3.14 Stereographic projections of the misorientation independent grain boundary plane distribution for $SrTiO_3$ determined for the same sample scan area at different orientation map step sizes. Figures (a) and (b) show negligible differences (less than 6 %) while figure (c) shows appreciably less anisotropy and is beginning to lose features observable in (a) and (b).

The $\lambda(\mathbf{n})$ distributions for the 0.5 μm and 1 μm datasets are obviously anisotropic and similar. In fact, the maxima differ by less than 6 % and are indistinguishable according to our 10 % tolerance level. For these two datasets, the observed average grain sizes are very similar, indicating that while we may be losing a small amount of information by increasing the step size/average grain diameter ratio from 1:23 to 1:12, we are observing nearly the same in-plane geometry of the microstructure with respect to the resolution of the binning used for the calculations. It is likely that most of the non-identified grains were too small to yield accurate in-plane grain boundary geometry as well. The results for the 2 μm dataset, however, are noticeably more isotropic. We must first determine if this result is due to a lack of observations. Using analysis similar to that used in Chapter 3, Section 3.1, it is possible to quantify the effect of the number of observations used on the reconstruction of the GBPD for this specific experimental case. For this case, the first N lines of the reconstructed boundary segments file for the 0.5 μm dataset (where N = 500, 1,000, 2,000, 5,000, 6,900 and 11,400) were used to calculate

the reconstructed GBPD. The maximum and minimum in the distributions were recorded

and plotted as a function of number of segments in Fig. 3.15. It is observed that the

maximum of the distribution, and thus the max/min ratio, is apparently still increasing

with the number of segments used to calculate the distribution for this dataset. However,

the rate of changes is low enough such that after 6,900 segments, the calculated values

are differing by less than 5 %. With this number of observations, we are capable of

consistently determining the GBPD for this dataset.
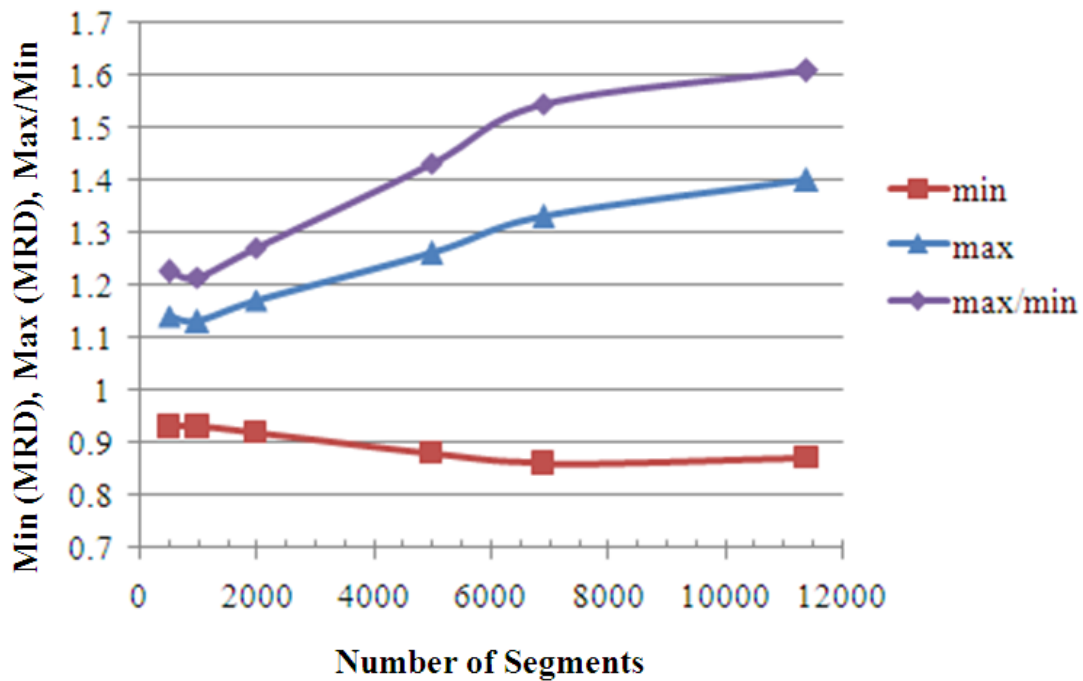
Figure 3.15 The maximum, minimum, and maximum/minimum ratio of the calculated
GBPD for the 0.5 μm step size SrTiO$_3$ data set plotted with respect to the number of
segments used in the calculation. Observed differences are less than 5 % when more than
6,900 segments are used in the GBPD calculation.

A similar analysis of the 2 μm dataset is useful for comparison. Again, the first N

lines of the reconstructed boundary segments file (where N = 500, 1,000, 2,000, 5,000,

and 6,900) were used to calculate the reconstructed GBPD. The maximum and minimum

in the distributions were recorded and plotted as a function of number of segments in Fig.
3.16.
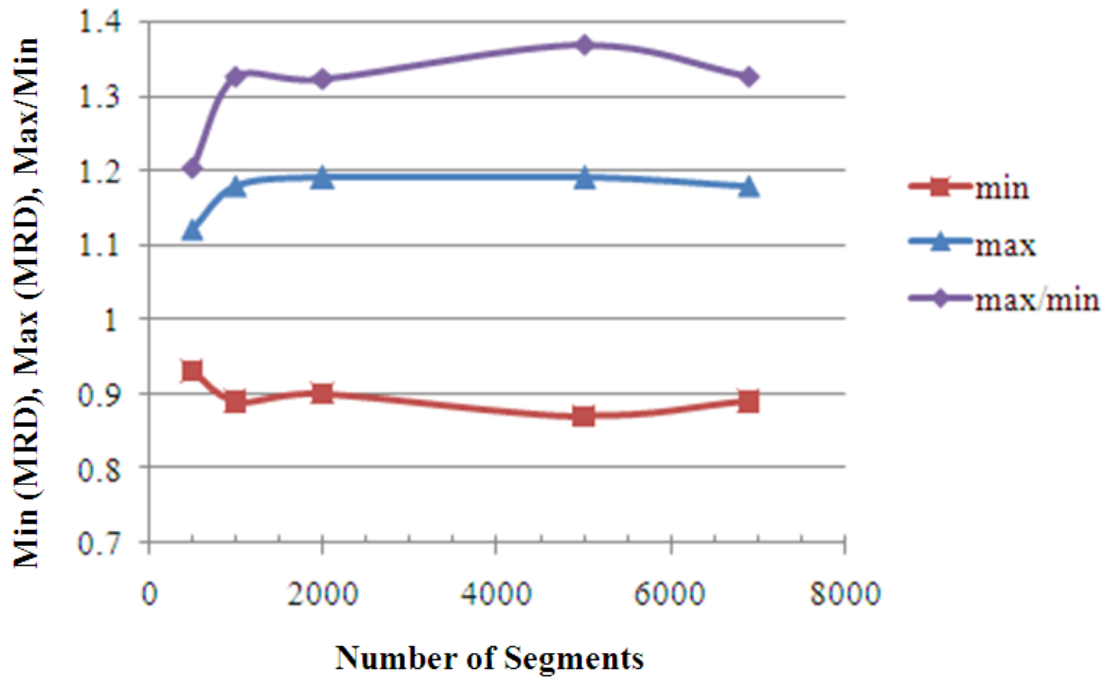
Figure 3.16 The maximum, minimum, and maximum/minimum ratio of the calculated
GBPD for the 2.0 μm step size SrTiO$_3$ data set plotted with respect to the number of
segments used in the calculation. Observed differences are less than 5 % when more than
1,000 segments are used in the GBPD calculation. The observed GBPD exhibits weak
anisotropy.

For the 2 μm case, there is less than 5 % variation in the calculated populations
based on greater than 1,000 segments. Therefore, 6,900 reconstructed boundary
segments are more than sufficient to determine the GBCD if they truly represent the in-
plane geometry of the microstructure. The differences between the grain boundary plane
distributions derived from the 0.5 μm dataset and the 2 μm dataset are, therefore, a result
of the grid resolution and not the number of segments used in the calculation. The
significantly larger observed average grain size for the 2 μm dataset is a result of under-

sampling the microstructure. As a result, the approximation of the in-plane geometry of the grain boundary network is poor enough to create random grain boundary segments that result in a measured GBCD that is more isotropic than reality.

Finally, a comparison must be made between the 0.5 μm dataset and the 1 μm dataset to judge how similar they are and to aid in determining the ideal step size/average grain diameter ratio. Results of the effect of the number of segments used in the calculation of the GBPD for the 1 μm sample are plotted in Fig. 3.17.

There will always be grains that are smaller than the average grain size. Under-sampling of these small grains (not enough points/grain) will always lead to an underestimation of the anisotropy of the GBCD. The fraction of the dataset that these grains represent will determine to what extent the observed GBCD will be affected. Increasing point density will only help to a certain extent. In addition to making collection time significantly slower (halving the step size of a hexagonal grid results in a collection time nearly four times longer for the same area), new "small" grains will be identified at the higher resolution that will still not have enough points/grain.
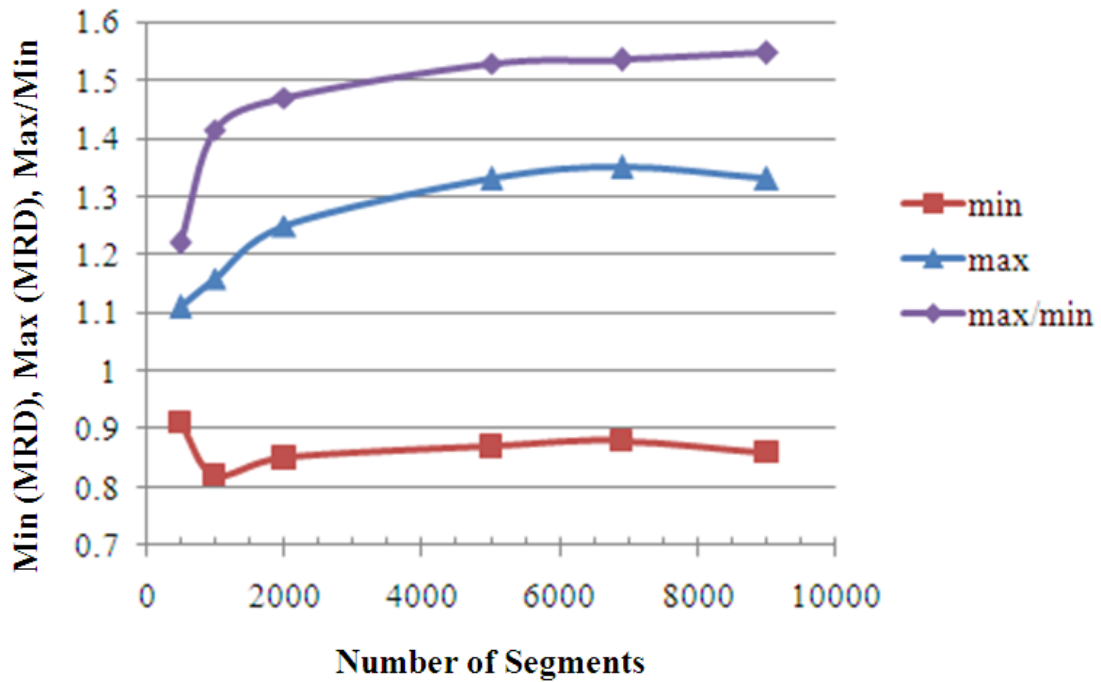
Figure 3.17 The data in Fig. 3.13 show that increasing the number of observations beyond 2,000 changes the distribution by less than 6 %. At this grid spacing, we are consistently measuring a GBPD that differs by less than 5 % of that calculated from the 0.5 μm dataset. For this sample, a step size/average grain diameter ratio of 1:12 is acceptable for consistent determination of the GBPD.

This analysis also assumes a relatively equiaxed microstructure. While no step size/average grain diameter analysis has been completed for microstructures with elongated grains, the previous result can be generalized to the requirement that enough points/grain should be recorded to adequately represent the grain boundary curvature. In practice, all of these factors need to be considered and a balance must be achieved. For the present work, an approximate 1:10 step size/average grain diameter ratio will be considered sufficient for the desired resolution.

As previously mentioned, discretization, and especially resolution of the discretization, affects the number of distinguishable boundaries for a given crystal symmetry. In the complete five parameter domain, the five angular parameters used for

discretization, $\phi_1, \Phi, \phi_2, \theta, \phi$, range from 0 to $2\pi, \pi, 2\pi, \pi$, and 2π, respectively. The total volume of the space is then $8\pi^5$. For equal angular binning, if each parameter is known with accuracy Δ, the total number of distinguishable boundaries is found by dividing the total volume $(8\pi^5)$ by the volume of one bin, Δ^5, and accounting for crystal symmetry. Allowing for crystal interchange and the direction of the boundary normal introduces a factor of 4 into the denominator. The number of distinguishable boundaries will then be:

$$N = (8\pi^5)/4M^2\Delta^5 \qquad \textbf{Eqn. 3.3}$$

where M is the number of proper symmetry operators.

Another conclusion based on these results is that the number of required segments for reliable GBCD reconstruction is resolution dependent. If relatively low angular resolution determination of the GBCD is desired, a relatively high step size/average grain diameter can be used and fewer reconstructed boundary observations will be required. For higher angular resolution determination of the GBCD, however, it is necessary to increase both orientation map spatial resolution and the number of reconstructed boundary segments used in the calculation. Merely increasing one will not compensate for the other.

It is known that there are variations in boundary properties for angular deviations less than 10 ° [68]. However, it is experimentally difficult to measure boundary normals with accuracy better than 5 °. For the majority of this work, 10 ° binning will be used. At this resolution, there are approximately 6.5×10^3 distinct boundaries for a cubic system [10]. Higher resolution results will be presented for datasets large enough to allow for

statistical significance. These results will show that there are many instances when it is indeed useful to reconstruct the GBCD at resolutions higher than 10 °.

Presently, estimates of the amount of data needed for such analysis are based upon the benchmarking experiments of Chapter 3, Section 3 and Eqn. 3.3, which determines the number of distinguishable boundaries for a given resolution. As an example, doubling the resolution increases the number of distinguishable boundaries by a factor of 2^5, or 32. A simplistic estimate of the number of observations required for statistical significance at 5 ° resolution, then, can be found by multiplying the number of observations required for significance at 10 ° resolution by 32. The effect of higher resolution binning of the GBCD space will be explored in Chapter 6, Section 3. It is, of course, important to extend the quantitative benchmarking to the full five parameter GBCD determination, as well.

3.3.5 Quantifying Differences in Five Parameter GBCDs

As previously mentioned, it is expected that the number of observations required for reliable determination of the GBCD will be significantly more than the number that is required for reliable determination of the GBPD. The required number of observations will also likely be sample, or at least material, specific. The number of grain boundary observations used in the calculation of the GBCD will also affect the variation within a given dataset. As with the comparisons of GBPDs, it will be inappropriate to interpret differences between unique datasets that are less than experimental uncertainties that are inherent to the individual datasets. It is also expected that experimental uncertainties within a dataset will be spatially specific within the five dimensional space – that is, the

uncertainties will not be uniform throughout the space. This is a result of inherent bias in the sampling of the material, as well as in the binning of the space for the calculation of the GBCD. Because of these factors, it is not possible to establish specific guidelines for quantitative GBCD comparison that will apply to all materials and all boundary types. As a result, it will be necessary to determine experimental uncertainties at specific points of interest in the five parameter space to determine whether perceived differences between datasets are distinguishable from the uncertainties. These issues will be addressed in Chapter 4, Section 2.2.

3.4 Evolution of the GBCD with Grain Growth in SrTiO$_3$

Interrupted grain growth experiments in which the GBCD was determined with 10 ° resolution at three time intervals during fixed temperature grain growth were performed on a polycrystalline SrTiO$_3$ sample. Aldrich SrTiO$_3$ (< 5 μm, 99 %) powder was dry-ground for approximately ten minutes in an alumina mortar and uniaxially compacted at 1000 psi to form a ½ " diameter pellet. The sample was fired in a Lindberg Blue/M High Temperature furnace in air using the following heating schedule:

i)   10 °C/minute to 900 °C with a 10 hr dwell

ii)   5 °C/minute to 1340 °C with a 10 hr dwell

iii)   20 °C/minute to 1470 °C; furnace cool to room temperature

This sample was used as the reference point and is referred to as the "zero-hour" sample. To achieve a surface finish suitable for EBSD measurements, the sample was lapped flat using 3 μm alumina slurry and a Logitech PM5 with a flat cast iron plate. The sample

was then polished on the PM5 using 0.02 μm colloidal silica (Buehler Mastermet II) for approximately thirty minutes. Next came a brief, relatively low temperature anneal at 1100 ºC for one hour to heal any residual surface deformation. A thin carbon-coating was then evaporated onto the sample to eliminate charging effects in the SEM (SPI-Module Carbon Coater). Orientation maps were recorded at a 60 ° tilt with a 25 kV beam. The step size for the orientation mapping was 0.35 μm in the x-direction, with a hexagonal grid. In total, 26 orientation maps were collected, covering an area of 0.57 mm^2. The orientation data were then processed to remove spurious observations using a "grain dilation clean up" in the OIM software (see description in Chapter 3, Section 3.1). In this case, a single iteration dilation with a minimum grain size of five pixels was used to avoid filling actual pores with fictional orientation data. A pseudosymmetry correction which eliminated false boundaries defined as a 45 ° rotation around [001] was also employed to correct for a very specific mis-indexing problem involving difficult to distinguish orientations [69]. The GBCD was determined for the resultant dataset comprised of 48,089 grains with an equivalent area diameter of 2.89 μm. This results in a step size/average grain diameter of 1:8.2. It is expected that this may result in an underestimated GBCD for reasons discussed in Chapter 3, Section 3.3. Because of the bimodal nature of the grain size distribution, it was difficult to achieve a step size:average grain diameter of 1:10 – scans with slightly smaller step sizes led to smaller observed average grain diameters. As a result, it was not possible to experimentally achieve a 1:10 ratio. 120,938 reconstructed grain boundary line segments were used to calculate the GBCD for this sample state. As will be seen in Chapter 4, this did not change any of the conclusions that were reached.

Grains were grown in the same pellet using the following heating schedule to create the next sample state, referred to as the "one hour" sample:

i)   10 ºC/minute to 900 ºC with no dwell

ii)   5 ºC/minute to 1470 ºC with a 1 hr dwell

iii)   5 ºC/minute to 25 ºC (room temperature)

The same sample preparation routine was used to collect a dataset of eight orientation maps with a hexagonal grid with 1.0 µm spacing, covering 6.05 mm^2. A similar clean up procedure using ten pixels as the minimum grain size (two passes of single iteration) yielded a dataset that included 29,200 grains an equivalent area diameter of 11.9 µm. This resulted in a step size/average grain diameter ratio of 1:11.9. 81,429 reconstructed grain boundary line segments were analyzed. The following firing cycle was then used to create the third sample state, which will be referred to as the "three hour" sample.

i)   10 ºC/minute to 900 ºC with no dwell

ii)   5 ºC/minute to 1470 ºC with a 2 hr dwell

iii)   5 ºC/minute to 25 ºC (room temperature)

Fig. 3.18 shows the full thermal history of the sample, and indicates the point in time that the datasets were recorded.
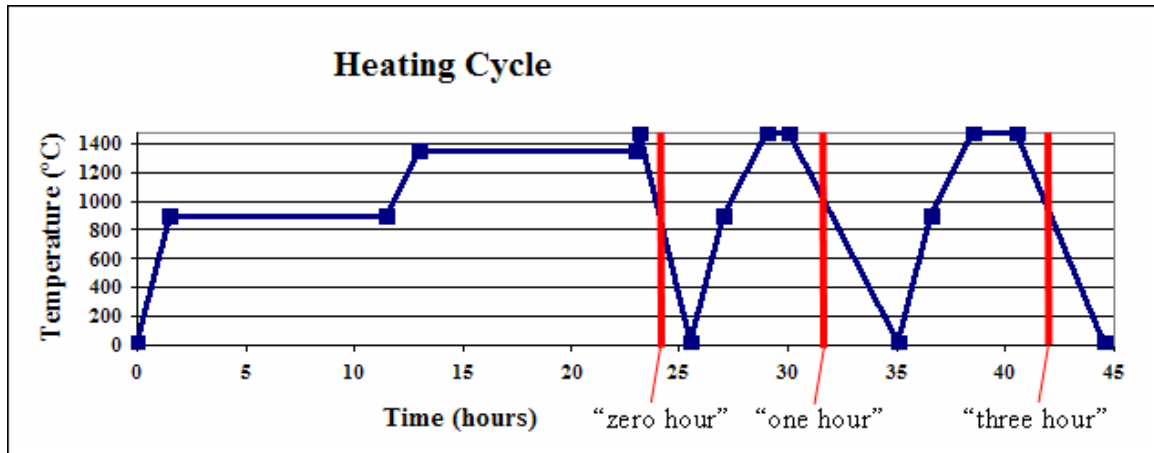
Figure 3.18 Shown is a schematic of the furnace cycle used to create the SrTiO$_3$ samples used in the GBCD evolution experiments. The labels "zero hour," "one hour," and "three hour" refer to the three datasets recorded.

Eight orientation maps on a hexagonal grid with 2 µm lateral resolution were collected covering an area of 14.5 mm^2. After clean up (single pass dilation with 20 pixel minimum, followed by a single pass with a 5 pixel minimum), 25,909 grains, with an equivalent area diameter of 23.2 µm, remained. This resulted in a step size/average grain diameter ratio of 1:11.6. 77,445 reconstructed grain boundary line segments were used in the reconstruction of the GBCD. A summary of the data collected for the three samples is found in Table 3.1

Table 3.1 Summary of Data for SrTiO$_3$ GBCD Evolution Experiment

Sample	scan area, mm^2	# grains	<d>, μm	step size: <d>	# reconstructed boundary segments
zero hour	0.57	48,089	2.89	1:8.2	120,938
one hour	6.05	29,200	11.9	1:11.9	81,429
three hour	14.5	25,909	23.2	1:11.6	76,445

3.5 Influencing GBCD Formation with Doping in MgO

Doping of ceramics has proven effective at changing the grain boundary energy anisotropy [50]. It is expected that this will cause changes in the observed steady state behavior of the GBCD when compared to the undoped material. A 3000 ppm Ca-doped MgO sample was created for the comparison of the GBCD with a previously studied nominally pure MgO sample that was prepared in a similar fashion [70]. High purity carbonates (Alfa Aesar Puratronic MgCO$_3$Mg(OH)$_{2+}$XH$_2$O 99.996 %, Alfa Aesar Puratronic CaCO$_3$ 99.999 %) were carefully dry-ground in an alumina mortar to promote mechanical mixing and uniform distribution of the dopant. The combined carbonates were then calcined at 1100 ºC for five hours in three nested MgO crucibles to avoid contamination in the furnace. The resultant powder was again dry-ground and then compacted to approximately 1000 psi in a ½ ” diameter cylindrical die using a Carver uniaxial press.

The pellet was placed on a bed of mother powder in three nested MgO crucibles and fired using the program:

i)   5 ºC/min to 900 ºC with a 10 hr dwell

ii)   5 ºC/min to 1200 ºC with a 7 hr dwell

iii)   5 ºC/min to 1600 ºC with a 7 hr dwell

iv)   5 ºC/min to 25 ºC (room temperature)

The sample was then prepared for EBSD. Rough grinding was completed using progressively finer SiC paper, using Buehler Metadi fluid as a lubricant because water tends to degrade MgO specimens. Final polishing was accomplished using 1 μm and 0.1 μm diamond in oil on Buehler Mastertex cloth. The sample was then annealed at 1200 °C for two hours and carbon coated (SPI-Module Carbon Coater) to eliminate charging under the electron beam. Maps were collected on a hexagonal grid with 1 μm spacing in the x-direction. In total, twenty scans were collected that cover 18.84 mm^2. Preliminary processing of the data included three passes of single iteration grain dilation clean up in the OIM software and assigning of an average orientation to each grain. At this point, 41,636 grains with an average diameter of approximately 20.4 μm were identified. However, these results include a significant number of falsely identified small interior grains. This data was converted to square grid format and the number weighted and area weighted MDFs were calculated.

For calculation of the five parameter GBCD for the Ca-doped MgO sample, false grains were manually identified and reassigned correct orientations. This dataset represents 17.4 mm^2 of scan area and is comprised of approximately 34,000 grains with an average diameter of 21.9 μm. This resulted in a step size/average grain diameter ratio

of 1:21.9. 113,749 reconstructed grain boundary line segments were used in the reconstruction of the GBCD.

3.6 Evolution of the GBCD with Grain Boundary Engineering in Nickel

3.6.1 Experimental Approach

To better understand the effects of sequential thermo-mechanical processing on the microstructure of fcc metals, orientation mapping will be used to characterize commercial and high purity nickel in both reference and "grain boundary engineered" states. One objective of this work is to determine the grain boundary plane orientations of the $\Sigma 3$ boundaries that are created during processing. Conventional metrics based on misorientation, such as the length and number fractions of $\Sigma 3$, $\Sigma 9$, and $\Sigma 27$ boundaries, will be calculated. It is expected that there will be a relatively high proportion of $\Sigma 3$ boundaries in both reference and "grain boundary engineered" states, and that the populations of these three types of boundaries will increase with processing. The $\Sigma 3^n/\Sigma 3$ ratio will be calculated for each material in an attempt to differentiate between microstructural changes comprised only of twin generation and those of a more complex nature where multiple twinning events can lead to the generation of $\Sigma 9$ and $\Sigma 27$ boundaries.

In addition to metrics based solely on misorientation, the orientation of grain boundary planes will be considered as well. Five parameter GBCD analysis will allow for the determination of the relative coherency of twin boundaries. Population with respect to coherency is calculated and compared for the reference and grain boundary

engineered states. This will allow for the determination of the types, or orientations, of the twins that are being formed with processing. Comparisons of boundary populations based upon the full five parameter space will also be included.

It is likely that the connectivity of the grain boundary network affects microstructure-dependent properties. Crystallographic constraints may restrict allowed boundary geometries. In this case, grain boundary energy may not be the main determining factor of boundary geometry. To observe the effects of grain boundary engineering on the connectivity of the grain boundary network, triple junction analysis will be performed. In this analysis, triple junctions will be classified according to the types of boundaries from which they are composed. Comparisons between reference and grain boundary engineered states will be made. It is expected that there will be an increase in triple junctions that contain $\Sigma 3^n$ boundaries and a decrease in triple junctions comprised only of random, non-$\Sigma 3^n$ boundaries. This would seem to be a natural result of an increase in $\Sigma 3^n$ boundaries. As another measure of network connectivity, the average diameters of twin related areas will be calculated and compared.

3.6.2 EBSD Mapping of Commercially-Available GBE Nickel

The commercially available polycrystalline Ni samples used in this study were obtained from Integran Technologies, Inc. [71]. The samples were provided in a reference state (before GBE) and in a final state following the GBE process. The two samples will be referred to as Integran reference and Integran GBE, respectively. The samples were prepared by first grinding the surface with SiC and diamond abrasives, then

polishing using a vibratory chemomechanical process with a 0.02 μm SiO_2 slurry, and finally electropolishing in a chilled 9:1 methanol:perchloric acid solution.

Crystal orientation maps on planar sections were obtained as described previously. Orientation maps were recorded at a 60 ° tilt with a 20 kV beam. The step sizes for the orientation mapping were between 2 μm and 4 μm, and were recorded over individual areas of 1 to 4 mm^2. In total, 64.0 mm^2 of the reference sample were mapped (an area containing approximately 20,000 grains) and 67.3 mm^2 of the GBE sample were mapped (an area containing approximately 25,000 grains). The orientation data were then processed to remove poorly indexed points using an iterative 'grain dilation clean up' in the OIM software that fills all space logically. This approach was chosen so that the maps would represent the fully dense nature of the sample. A single orientation was then assigned to each grain by averaging all of the orientations belonging to a single grain. The OIM analysis software was then used to extract 86,335 reconstructed boundary segments from the reference sample and 115,231 reconstructed boundary segments from the GBE sample. The number of observations recorded should be sufficient to determine the GBCD at a 10 ° resolution. A summary of the data collected for the Integran reference and GBE nickel is presented in Table 3.2. The guidelines established in Chapter 3, Section 3 were not strictly followed in the data collection for these samples, as the guidelines were not fully established prior to this experiment. Nevertheless, the data follows the guidelines reasonably well. Potential experimental errors caused by this will be addressed during discussion.

Table 3.2 Summary of Data for GBCD Reconstruction of Integran^{TM} Reference and GBE Nickel

Sample	scan area, mm^2	# grains	$\langle d \rangle$, μm	step size: $\langle d \rangle$	# reconstructed boundary segments
reference	64.0	20,000	40 μm	variable	86,335
gbe	67.3	25,000	40 μm	variable	115,213

3.6.3 Iterative Thermomechanical Processing of High Purity Nickel and EBSD Mapping

Iterative thermo-mechanical processing of high purity nickel (Alfa Aesar Puratronic 99.999 %, 5 mm rod) was performed in-house. Reference and GBE samples were studied to observe the effects of grain boundary engineering on the GBCD of high purity nickel in controlled experiments with known sample processing conditions.

The reference sample was created by cutting a ¼ " thick disc from the rod and annealing at 416 °C in flowing dry H_2 for 24 hours to homogenize the microstructure. The sample was prepared for EBSD orientation mapping by hand grinding with progressively finer SiC paper, followed by polishing with 6 μm, 3 μm, and 1 μm diamond slurries, and final finishing polishes of 0.02 μm colloidal SiO_2 on a wheel and in a vibratory polisher.

Grain orientation maps were collected from three layers separated by a thickness of at least the average grain diameter. In total, 34 maps no larger than 750 μm x 750 μm were collected, covering a total area of 17.4 mm^2. After grain dilation with a minimum grain size of 10 pixels and assignation of an average orientation to each grain, 76,848 grains with an average diameter of 12.7 μm were identified. This resulted in a step

size/average grain diameter ration of 1:12.7. 293,623 reconstructed grain boundary line segments were extracted.

To produce the "grain boundary engineered" sample, a ¼ " thick disc was cut from the rod and annealed at 413 ℃ in flowing dry H_2 for 24 hours. Although there was a nominal 3 ° difference in the annealing temperatures, we will assume that the samples are comparable.

Exact GBE parameters such as annealing time, temperature, and amount of deformation are not published for commercially available materials. Instead, ranges of temperatures or amounts of deformation are frequently reported. To determine an annealing time and temperature for sequential thermo-mechanical processing for this study, annealing experiments were performed. A decrease in hardness is one indicator of recrystallization. Hardness is expected to decrease rapidly and approach a constant value with recrystallization. For this study, a deformation level of 25 % was chosen after consulting literature values [71]. Cold rolling was used to accomplish the deformation. Annealing temperatures of 550 ℃ and 700 ℃ were chosen based on ranges found in the literature [72, 73]. In each of these works, grain boundary engineering of copper is explored. Similar deformation levels were chosen for nickel for this work. Annealing temperatures were determined based on the relative melting points of copper and nickel. Three micro-hardness measurements were then completed and averaged after zero, one, five, and ten minutes during annealing to determine the annealing time required for recrystallization at a given temperature. The Vicker's hardness with respect to annealing time at 550 ℃ is plotted in Fig. 3.19.
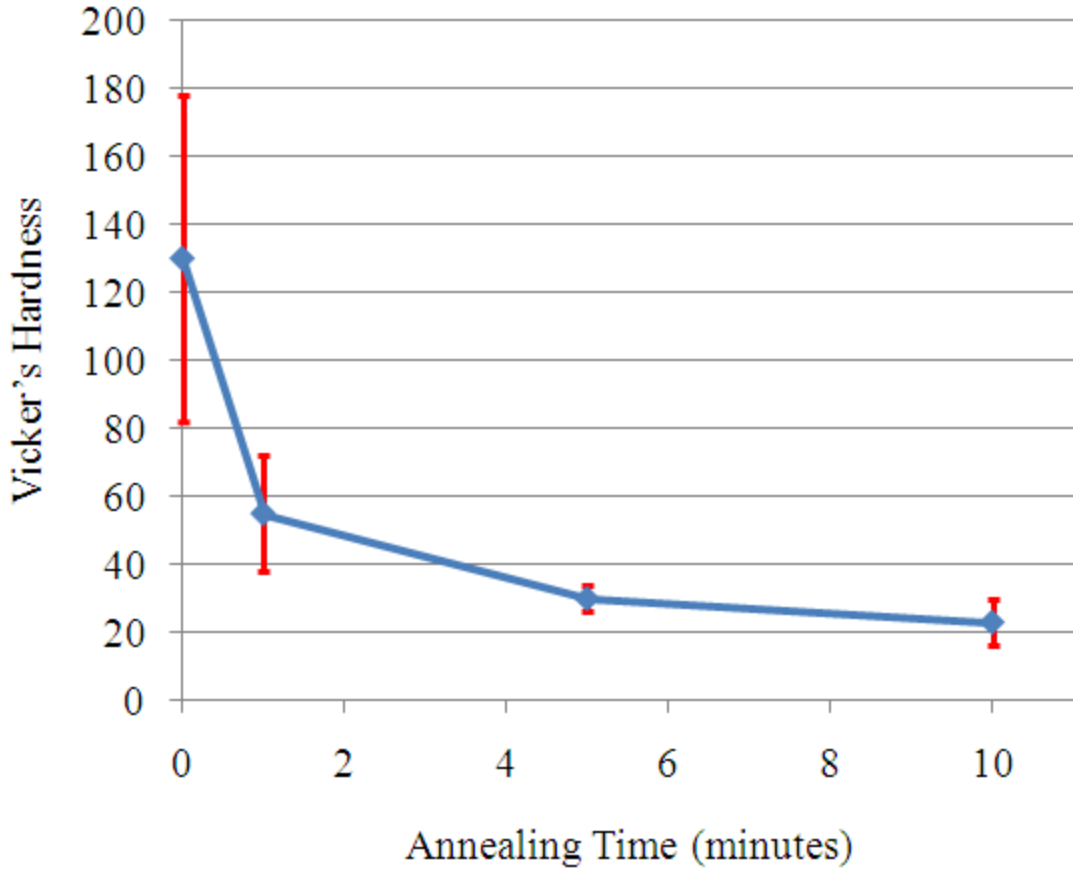
Figure 3.19 Vicker's hardness with respect to annealing time at 550 °C for a 25 % cold-rolled high purity (99.999 %) nickel sample. Hardness decreases rapidly and approaches a near constant with recrystallization after annealing for ten minutes. Three measurements were made at each time point and were averaged. Error bars represent one standard deviation from the mean. Significant spatial variations in hardness were observed for the as-deformed sample, but hardness became much more uniform as recrystallization proceeded.

Vicker's hardness decreases from 130 Hv to 23 Hv after ten minutes annealing at 550 °C.

A precipitous drop in hardness occurs during the first five minutes of annealing, after

which hardness remains relatively constant (albeit slightly decreasing as grain growth

presumably occurs). From these results, it was determined that the deformed material

should be fully recrystallized after ten minutes annealing at 550 °C. Significant

(unwanted) grain growth occurred during short-time annealing at 700 °C. As a result, 25

% cold deformation followed by a ten minute anneal at 550 °C were chosen as parameters for a single strain-recrystallization cycle for this study.

The sample was then subjected to five thermo-mechanical processing steps that involved cold rolling to 25 % reduction in thickness followed by ten minute annealing at 550 °C. Micro-hardness measurements were made after deformation and after recrystallization. Results of micro-hardness with respect to strain-recrystallization cycle number are plotted in Fig. 3.20. Results plotted at integer values represent hardness after complete strain-recrystallization cycle, i.e. after deformation and annealing, while values plotted at 0.5, 1.5, etc. were recorded after deformation. There is an anomalous value found for the hardness after the fifth deformation. At present, no explanation can be offered for this result. However, the hardness after the fifth annealing is comparable to the previous four cycles. As the goal of this work was not the optimization of the grain boundary engineering procedure, it was decided to continue the study using this sample to determine the effects of sequential thermo-mechanical processing on the GBCD of nickel.
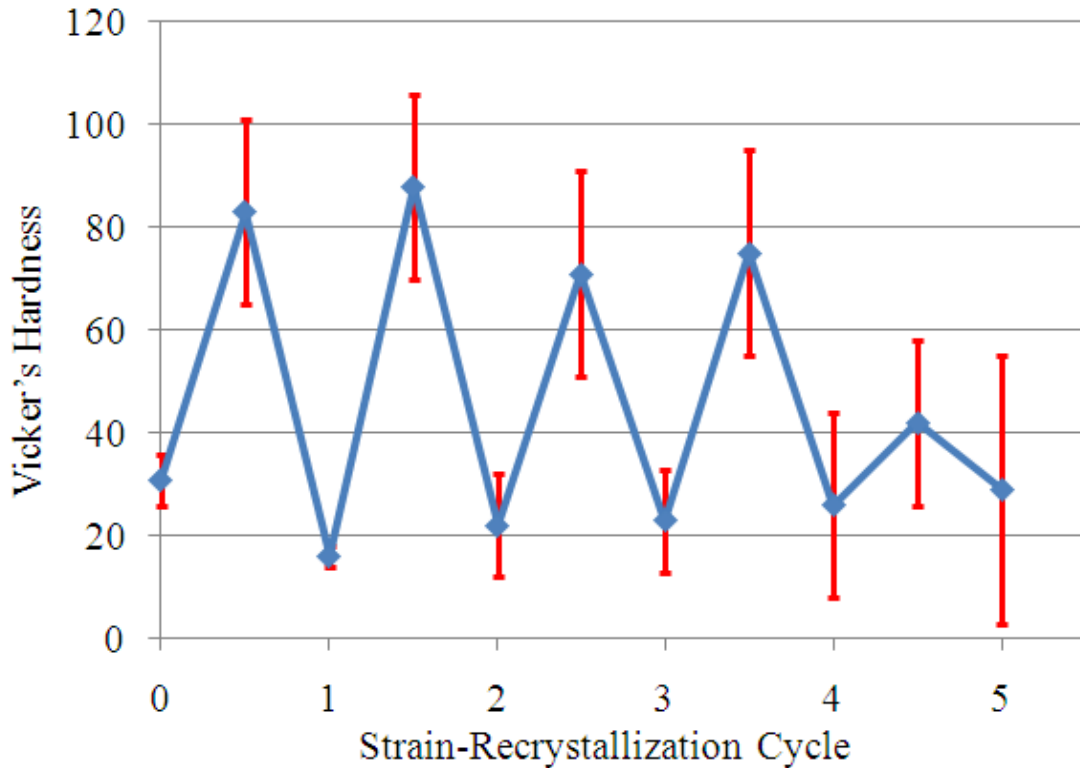
Figure 3.20 Vicker's hardness with respect to strain-recrystallization cycle. For one cycle, the sample is cold-rolled to 25 % deformation and annealed at 550 °C for ten minutes.

The sample was prepared for EBSD following similar procedures as for the reference sample. In this case, data was recorded from five layers separated by more than an average grain diameter. For three layers, electropolishing with a dilute (40:60) H_2SO_4:H_2O electrolyte was employed to improve the surface finish. This sample will be referred to as the SR5 sample.

The full dataset for the SR5 sample includes 64 orientation maps collected from the five planar sections. A total area of 199 mm^2 was mapped. After grain dilation cleaning of the data (minimum grain = 20 pixels) and assignation of an average orientation to each grain, 63,933 grains with an average grain diameter of 40.57 μm were identified. This resulted in a step size/average grain diameter ration of 1:27. 331,730

reconstructed grain boundary line segments were extracted. A summary of the data

collected for the reference and SR 5 sample is presented in Table 3.3.

Table 3.3 Summary of Data for GBCD Reconstruction of Reference and SR5 High-Purity Nickel

Sample	scan area, mm^2	# grains	$<d>$, μm	step size: $<d>$	# reconstructed boundary segments
reference	64.0	76,848	12.7	1:12.7	293,623
SR5	199.0	63,933	40.57	1:27	331,730

The large datasets collected for these two samples will allow for higher resolution

binning of the five parameter space than has previously been possible. This will provide

insight into the magnitude of the underestimation of the anisotropy of the GBCD when

determined at 10 ° binning. Higher resolution binning will also allow features that are

less than 10 ° apart in five parameter space to be differentiated.

In this work, we will determine the characteristics (crystallographic orientation)

of the $\Sigma 3$ grain boundaries introduced by the grain boundary engineering process in Ni,

and how they affect the structure of the grain boundary network. The results indicate that

while the misorientation distributions created by grain boundary engineering are similar

in brass and Ni, the orientations of the grain boundary planes, and their effect on the

structure of the polycrystalline network are very different. Conventional metrics such as

length and number fraction of $\Sigma 3^n$ boundaries will be presented. Total length and length

per area of these specific boundaries will also be presented. Finally, triple junction

analysis will be performed to quantify the effects of modification of the connectivity of

the grain boundary network.

3.7 Determining Relative Grain Boundary Energies

3.7.1 Relative Grain Boundary Energies of SrTiO₃

Our hypothesis states that interfacial energies are the main contributor to determining steady state GBCD behavior for untextured materials. The most common technique for determining relative grain boundary energies involves measuring the geometry of thermal grooves that form upon heat treatment where grain boundaries intersect a free surface. Herring [74] was the first to quantify the relationship between interfacial energy and interface geometry for such a configuration, using following force balance.

$$\sum \gamma^i \hat{t}^i + \partial \gamma^i / \partial \phi^i = 0 \qquad \textbf{Eqn. 3.4}$$

Atomic force microscope measurements of thermal grooves provide a relatively simple experimental technique for inferring relative grain boundary energies [12]. If a sufficient number of observations of groove geometries for crystals of known orientations are made, it is possible to know the true distribution of interfacial energies. This typically requires model microstructures such as bicrystals and typically ignores the so-called torque terms, which are proportional to the gradient of energy with respect to the inclination angle. Assuming isotropic surface energy and that the grain boundary energy is a function of misorientation only, a simplification of the Herring equation can be expressed as:

$$\frac{\gamma_{gb}}{\gamma_s} = 2\cos(\Psi_S/2) \qquad \textbf{Eqn. 3.5}$$

It is possible to measure the width and depth of thermal grooves with AFM, and solve for the diherdral angle, ψ, using the Mullins equation (Eqn. 3.6) [75] for the equilibrium, scale-invariant grain groove profile formed my surface diffusion. Fig. 3.21 is a schematic which defines the variables used in Eqns. 3.6 and 3.7

$$\frac{w}{d} = \frac{4.73}{\tan \beta} \qquad \textbf{Eqn. 3.6}$$

where

$$\beta = 90 - \frac{\Psi_S}{2} \qquad \textbf{Eqn. 3.7}$$
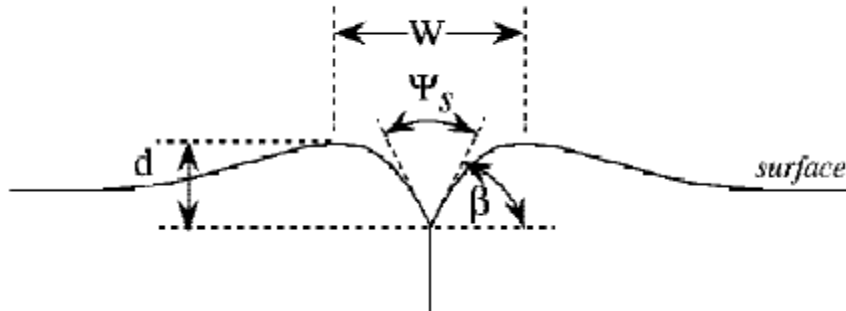
Figure 3.21 Schematic of an idealized thermal groove formed by diffusion during annealing at the intersection of a grain boundary and a polished surface. W represents the full width of the groove from peak to peak, d represents the depth of the groove measured from a peak to the groove root, β represents the angle of inclination of the groove with respect to the polished surface, and Ψ_s represents the dihedral angle of the groove. The idealized groove is shown as being symmetrical with the grain boundary perpendicular to the surface – this configuration rarely occurs. This figure is reproduced from [76].

Using Eqn. 3.3, it is possible to calculate the ratio of γ_{gb}/γ_s assuming average

surface energy properties. Eqn. 3.5 also assumes that the grain boundary is perpendicular

to the surface and this will rarely be the case. It is possible, however, to average over this

source of error by measuring a distribution of many grain boundary grooves. Cumulative

probability plots can then be used to estimate the interfacial energy anisotropy for a

material [12]. This technique compares favorably with the metal reference line (MRL)

technique, as employed by Handwerker et al. [77], to measure estimated interfacial

energy anisotropy in Al_2O_3. In the current work, measurements of thermal grooves of

general boundaries, along with grooves of coherent and incoherent $\Sigma3$ boundaries, will be

compared for a $SrTiO_3$ sample prepared in a similar manner as the sample in the grain

growth experiment. The same Aldrich $SrTiO_3$ used for the GBCD evolution experiment

($< 5\ \mu m$, 99 %) powder was used, and compacted in the same manner as the previous

sample. The pellet was subjected to the following furnace cycle:

  i)   10 ℃/minute to 900 ℃ with a 10 hr dwell

  ii)   5 ℃/minute to 1340 ℃ with a 10 hr dwell

  iii)   20 ℃/minute to 1470 ℃ with a 0.5 hr dwell

  iv)   furnace cool to 25 ℃ (room temperature)

The sample was polished in a similar manner as for the GBCD evolution experiment and

then placed into the furnace at 1400 ℃ for 0.1 hour for thermal grooving. Using EBSD,

an orientation map was collected to identify incoherent and coherent $\Sigma3$ boundaries.

Thermal groove geometries of incoherent and coherent twin boundaries, as well as

general boundaries, were measured. As mentioned in Chapter 2, these boundaries were

chosen for investigation based on existing literature results [34] that showed a decrease in

$\Sigma 3$ boundaries with grain growth in $SrTiO_3$. These boundaries are also readily identifiable with orientation mapping. AFM measurements were made on a CPII AFM (Veeco Instruments) using contact mode and Si_3N_4 triangular cantilevers (ML06 type, Veeco Instruments). Scans were collected at a pixel resolution of 512 x 512 and varied in field of view. Scans were kept as small as possible while capturing the full shape of the groove to maximize lateral resolution. Maximum scan sizes were 50 μm x 50 μm; minimum lateral resolution was then approximately 0.1 μm. A minimum of three measurements were made per groove and reported results represent the average. In total, the grooves of 37 general boundaries, 27 incoherent $\Sigma 3$ boundaries, and 5 coherent $\Sigma 3$ boundaries were measured.

3.7.2 Relative Grain Boundary Energies of Undoped and 3000 ppm Ca Doped MgO

Grain boundary groove geometries were measured on the same 3000 ppm Ca-doped MgO sample used in the GBCD evolution experiment. The experimental procedure was similar to that for the $SrTiO_3$ sample. In total, 31 grain boundary grooves were measured and compared to similar measurements (performed by Dr. Francine Papillion) of 36 grain boundary grooves recorded for the nominally pure MgO sample. The number of observations recorded will be enough to show trends in the data. It is expected that the distribution of relative grain boundary energies will be different for the two samples. The main hypothesis of this work predicts that it is this difference that will lead to observable differences in the GBPD and GBCD.

3. 7.3 Determining Relative Energies from Serial Sections

Relative grain boundary energies were also determined from three dimensional microstructures recorded by serial-sectioning. A dual-beam focused ion beam (FIB) was used for sectioning and orientation imaging to reconstruct the 3-D microstructure. SrTiO3 and high purity Ni were both examined. Relative grain boundary energies were determined the techniques described by Dillon and Rohrer [78] based on work by Morawiec [79].

Chapter 4

4. Evolution of the GBCD with Grain Growth in SrTiO$_3$

4.1 Introduction

The purpose of this experiment was to measure the five parameter grain boundary character distribution at several time points during isothermal grain growth to observe the development of anisotropy in the distribution. It was hypothesized that grain boundary energy anisotropy would determine the evolution of the distribution and that the distribution would eventually achieve a self-similar state that was scale invariant. Lower energy boundaries should occur more frequently than in a random distribution. Quantitative comparisons of the GBCD at several time points are presented. Relative grain boundary energies were determined to support the hypothesis that the GBCD is experiencing an enhancement of lower energy boundaries through the preferential elimination of higher energy boundaries and an increase in area of lower energy boundaries.

4.2 Results

4.2.1 Misorientation-Independent Grain Boundary Plane Determination and Steady State Evaluation

The microstructure was not scale invariant at the three time intervals studied. The shape of the grain size distribution is not self-similar for the three time steps. Plots of the area fraction and number fraction grain size distributions for representative subsets of the zero hour and three hour data sets, which are comprised of approximately 27,000 grains and 4,400 grains, respectively, are shown in Fig. 4.1. The grain size distribution in the zero hour sample was bimodal, with peaks in the area fraction grain size distribution near 3 μm and 20 μm (Fig. 4.1a).
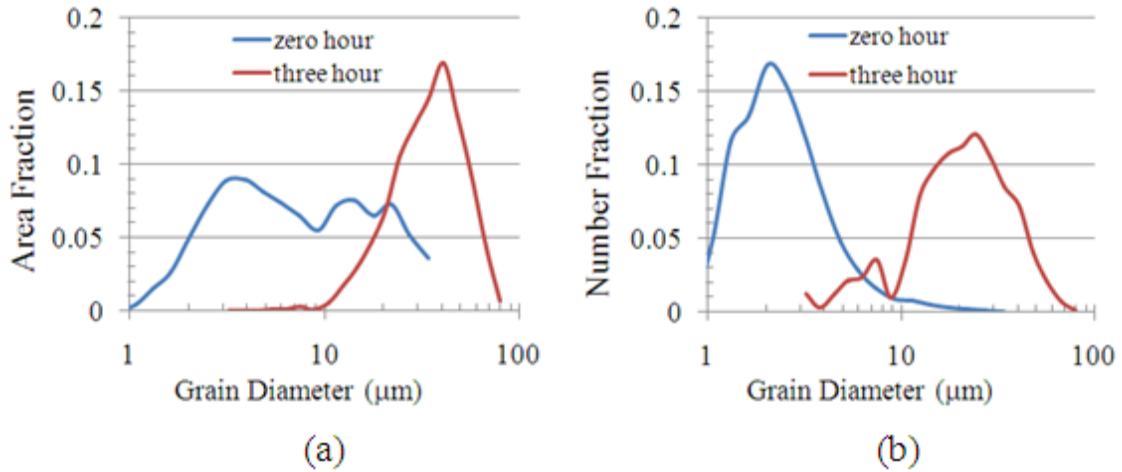
Figure 4.1 The area (a) and number (b) fractions of grains with respect to average grain diameter are plotted for representative areas of the "zero hour" and "three hour" sample. A peak near 3 μm for the area fraction of the "zero hour" data set shows that the bulk of the grains are approximately of this size, while a peak near 20 μm shows that there are an appreciable number of these grains as well. The areas of each are approximately equal, though the numbers are not.

With grain growth, the area fraction grain size distribution evolves to one that is relatively broad, with grain diameters ranging from 8 μm − 80 μm, but which is singularly peaked for grains that are approximately 40 μm in diameter. The population of grains less than 10 μm in diameter is decreased as grains grow or are consumed by other growing grains. As a result, the area fraction of such grains is necessarily lower. In Fig.4.2, OIM [001] inverse pole figure maps show the evolution of the microstructure with grain growth. Although the grain size distributions in Fig. 4.1 are not normalized by the average grain size, it is clear that they differ by more than a scale factor and normalization will not show them to be self-similar.

The hypothesis of steady state behavior during the evolution of the GBCD was based on the assumption of normal grain growth and scale invariant grain size distributions. The grain size distribution was not scale invariant at the times analyzed. Nevertheless, the grain boundary character distribution was measured for the zero, one, and three hour samples.
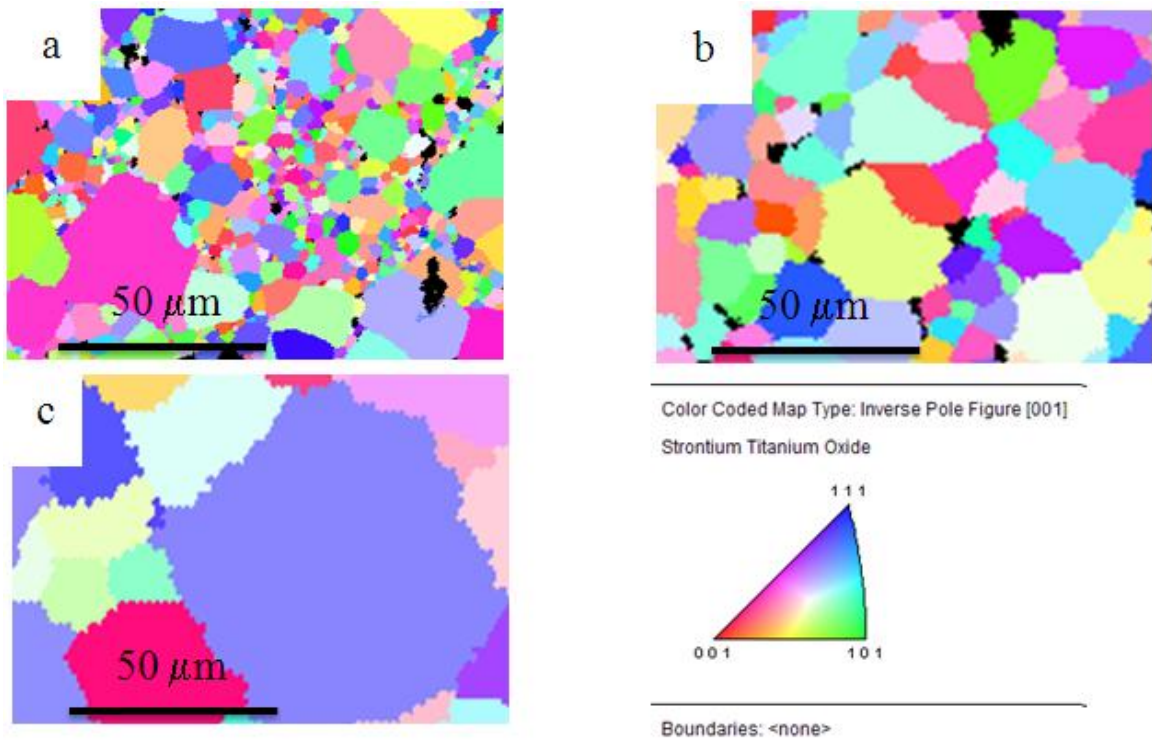
Figure 4.2 The [001] inverse pole figure orientation maps of crystal orientations with respect to sample coordinates colored according to the legend. (a) A representative area from the "zero hour" sample, (b) a representative area from the "one hour" sample, and (c) a representative area from the "three hour" sample.

The grain boundary plane distribution, $\lambda(n)$, for each is plotted in Fig. 4.3. As in previous measurements of the GBCD for $SrTiO_3$ [11], there is a peak in the distribution for {100} planes that is near 2 MRD. For dramatically different microstructures, within experimental error, these distributions differ by less than 10 % from the average value of 2.04 MRD and appear qualitatively similar.
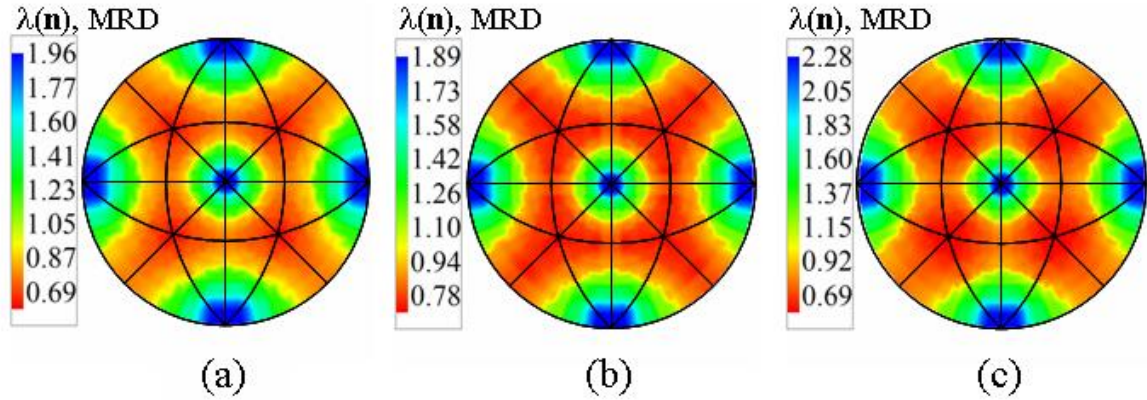
Figure 4.3 The misorientation independent grain boundary plane distribution is plotted for the zero hour (a), one hour (b), and three hour (c) samples. The distributions are quantitatively the same within experimental uncertainty.

Quantitative comparisons parallel to those already discussed in Chapter 3, Section 3 can be applied to this analysis. It is most important to determine how much variation there is within one dataset. This will determine whether the observed variation between several datasets is significant. For this analysis, the "three hour" dataset was chosen. First, the GBPD was calculated using an increasing number of reconstructed boundary segments. Results plotted in Fig. 4.4 show that the calculated values of the maximum and the minimum of $\lambda(\mathbf{n})$ is consistent after approximately 20,000 segments.
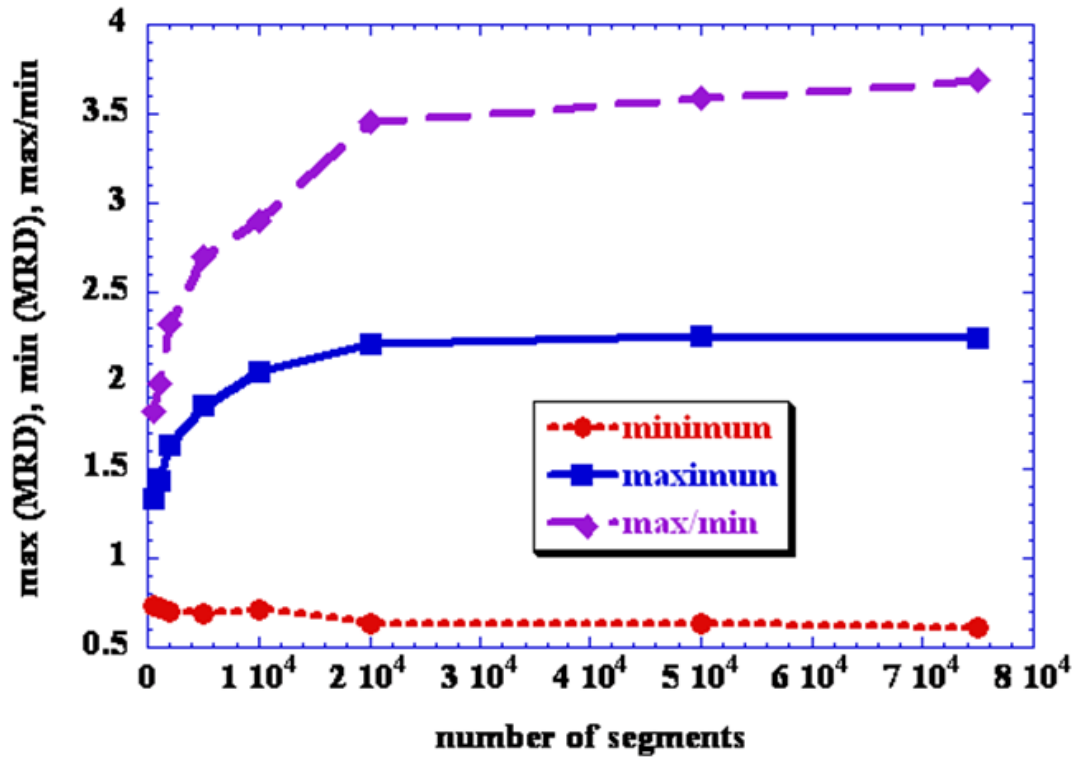
Figure 4.4 Maximum, minimum, and maximum/minimum ratio of the GBPD with respect to the number of segments used in the stereological calculation for the three hour SrTiO$_3$ sample. Each of the three values remains relatively constant when greater than 20,000 reconstructed grain boundary segments are used in the stereological reconstruction of the GBCD.

Significantly more than 20,000 segments were used in the calculation of the GBPD for the three time points. Therefore, there should not be any experimental uncertainties caused by a lack of observations.

There is, however, a possibility of variation within one dataset. To check this, the GBPD was determined for subsets of the "three hour" dataset that were comprised of approximately 26,000 reconstructed boundary segments. The results are plotted in Fig. 4.5. These subsets were not chosen randomly; they were merely selected from the first,

middle, and last third of the dataset to check for any systematic differences within the dataset.
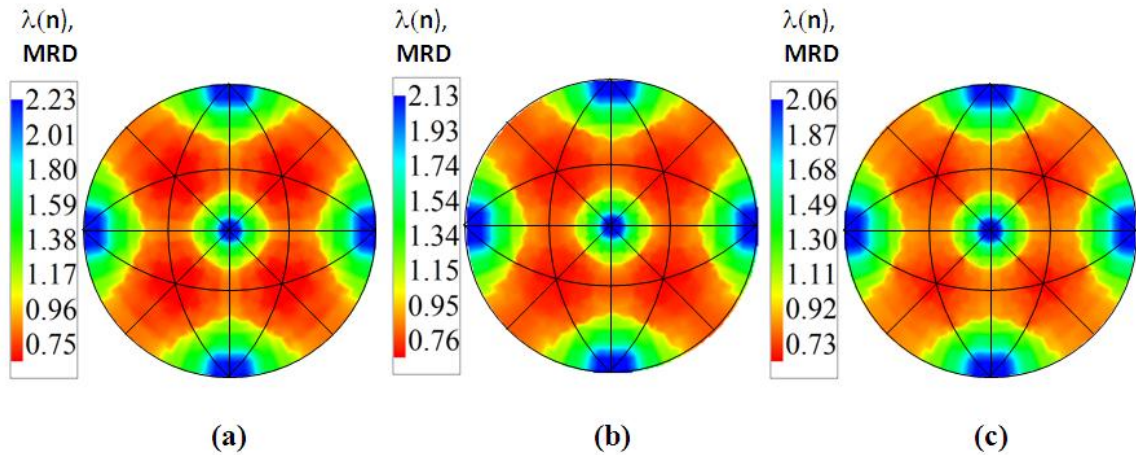
Figure 4.5 Stereographic projections of the GBPD for three subsets of the $SrTiO_3$ three hour data set. Approximately 26,000 reconstructed grain boundary segments are used to calculate the GBPD in each case. The maxima and minima of the subsets vary by less than 5 % from the average values, showing that variations within the dataset are negligible.

In this case, the maxima and minima of the subsets differ by less than 5 % from the averages. This 5 % is a measure of the uncertainties in the procedure. While there seems to be a slight systematic decrease in the anisotropy, in reality these differences are significantly less than the chosen 10 % threshold and will not be interpreted. As a result, it is determined that the GBPDs of the three time steps are experimentally indistinguishable and steady state behavior of the GBPD is observed. It was anticipated that the anisotropy would increase from an initially isotropic state but this was not observed. The implication is that the processes that occur during sintering and the earliest stages of grain growth already determine the GBPD.

4.2.2 Quantifying Uncertainty in Five Parameter GBCDs

Anisotropy in the GBCD cannot be described by anisotropy in the grain boundary plane distribution alone. Simulation and experimental results show misorientation dependent anisotropy in the GBCD [80]. Specifically, an enhancement of low-angle boundaries is observed.

These observations direct our investigation of the full five parameter GBCD. The GBCD was determined for the zero, one and three hour samples to observe the misorientation and boundary plane dependency of the distribution. Before quantitative comparisons of GBCDs can be made, however, it is important to establish guidelines, such as those presented in Chapter 3, Sections 3.2-3.4.

It is important to first determine the amount of variation within individual datasets. For this analysis, the "zero hour" and "three hour" datasets were used, as we would like to be able to compare GBCDs of the initial and final states. The GBCD was calculated for two halves, or subsets, of each dataset. For the "zero hour" comparison, there were approximately 60,500 reconstructed boundary segments in each subset. For the "three hour" comparison, there were approximately 38,700 reconstructed boundary segments in each subset. In one technique for quantifying the differences within each full dataset, the two GBCDs calculated from each half-dataset are compared bin-by-bin and fractional differences are calculated. This technique gives a global understanding of uncertainties within, or differences between, GBCDs. First, one bin is chosen in subset one. Second, all symmetrically equivalent bins are located. Next, populations in each bin are averaged and this average population is assigned to the bin. Then, the equivalent bin is selected in subset two, and the process is repeated to find an average population for

the equivalent bin. It is these average values that are compared for the two subsets. If either average value is below a pre-defined threshold population, the bins are excluded from the rest of the analysis. Otherwise, small absolute changes in small populations would be disproportionately represented as large fractional differences. The excluded data is tracked as a measure of the quality of the dataset. If both average values are above the pre-defined threshold, a fractional difference, *fd*, is calculated, according to Eqn. 4.1. Results will be plotted as "percent deviation."

$$fd = (<MRD_{subset1}> - <MRD_{subset2}>)/<MRD_{subset1}> \qquad \textbf{Eqn. 4.1}$$

The process is then repeated for each bin in the five dimensional space and the data is binned with respect to the fractional difference. In Fig. 4.6, comparisons of the subsets of the "zero hour" and the "three hour" datasets are plotted, along with a comparison of the full "zero hour" dataset to the full "three hour' dataset. The minimum threshold population for this analysis was chosen to be 0.45 MRD. For this plot, the "percent deviation bins" are named by the maximum deviation for that bin. Thus, the "10 %" bin includes all data that deviates by zero to ten percent. The "100 %" bin includes all data that differs by 100 % or greater. In all three cases, approximately 40 % of the data is excluded.

From this plot, it can be observed that there are appreciable differences between the subsets and the full datasets. As an example, for the included data, more than 30 % of the GBCDs calculated for the "zero hour" data subsets differ by 50 % or more, and more than 55 % of the GBCDs differ by 30 % or more. As a reminder, these values are only based upon included data, which should minimize effects caused by small perceived differences in already small populations. Interestingly, the trend of variation between the

"zero hour" and "three hour" GBCDs appears to follow the trend of differences found within each individual dataset. From these results, it appears that it will not be possible to use this technique to differentiate experimental uncertainties in five dimensions from true differences. It is possible to judge whether or not datasets are of comparable quality or which dataset would likely limit the accuracy of comparisons between two or more datasets.
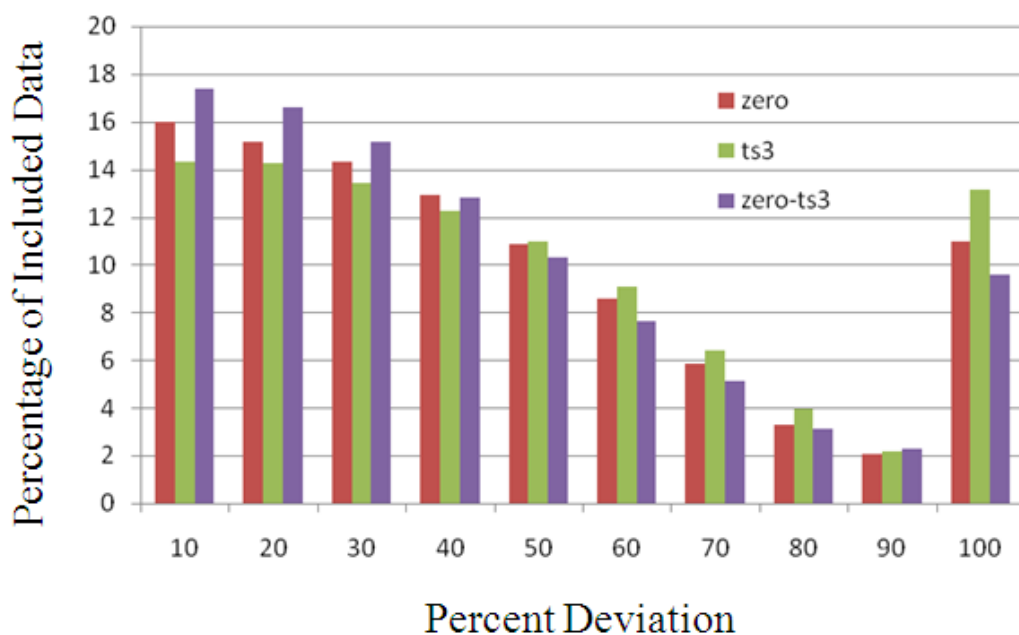
Figure 4.6 Percent deviation of the averages for equivalent boundaries for included data for the comparisons of subsets of the "zero hour" and "three hour" experimental $SrTiO_3$ datasets, as well as for the comparison of the full "zero hour" dataset with the full "three hour" dataset. Significant experimental uncertainty exists for datasets of this size when comparing bin-by-bin in the five dimensional space.

It is of course expected that the number of reconstructed boundaries used to calculate the GBCD will likely have an effect on the observed variation within a dataset. To ensure that the observed variations were not simply a result of too few reconstructed grain boundaries being used in the GBCD reconstruction, the percent deviation of

average for equivalent boundaries was calculated for two halves of a much larger

reconstructed boundary dataset. For this case, 1,000,000 simulated reconstructed

boundaries consistent with the simulated GBCD described in Chapter 3, Section 3.3 were

created. It should be noted that it would be time-prohibitive to collect an experimental

dataset of this size, even at the current highest possible data collection speeds.

Reconstructed GBCDs were then calculated for two subsets of 500,000 reconstructed

boundary segments and compared using this technique. Approximately 30 % of the data

was excluded from this calculation. The result for the percent deviation of average for

equivalent boundaries for this case is plotted in Fig. 4.7, along with the results from the

experimental $SrTiO_3$ data, for comparison. From this result, it is clear that even for a

prohibitively large dataset, there are still appreciable deviations within the dataset when

you apply bin-by bin comparison. While the result is significantly better than for the

much smaller experimental datasets, more than 25 % of the data still varies by 20 % or

greater. Thus, a threshold guideline for comparison of five parameter GBCDs cannot be

determined from this analysis alone.
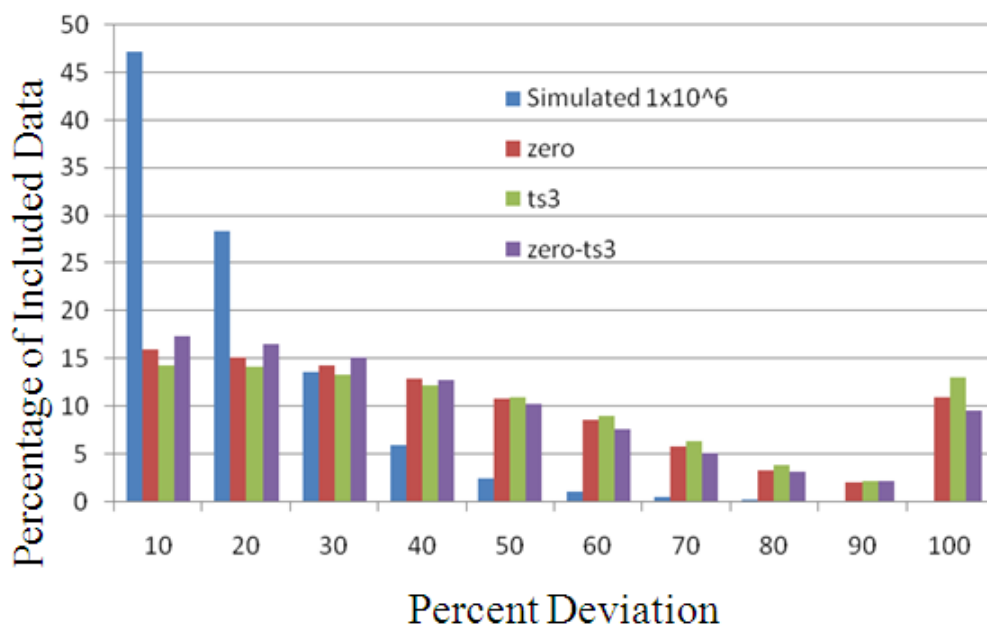
Figure 4.7 Percent deviation of the averages for equivalent boundaries for included data for two subsets of a simulated GBCD reconstructed from 1,000,000 simulated grain boundary segments. Plotting with the experimentally-based $SrTiO_3$ results, it is obvious that uncertainty is decreased for significantly larger datasets, but appreciable uncertainty still remains for this type of analysis. Specific threshold guidelines for quantitative comparisons of five parameter GBCDs cannot be determined from such analysis. The quality of the dataset used for the calculation can be judged, however.

Another problem with the previous technique is that it ignores possible variations in uncertainty within the five parameter GBCD. It is likely that because of sampling and binning of the data, that the amount of experimental uncertainty can vary with respect to location in misorientation or boundary plane space. As an example, there may be a specific location in misorientation space for which a 20 % difference is indistinguishable from experimental uncertainty, while at another specific location a 40 % difference is indistinguishable from experimental uncertainty. To explore this possibility, it is useful to consider how uncertainty is distributed with respect to misorientation.

The area-weighted MDF can be calculated for the zero, one and three hour sample states. The results with respect to absolute population and multiples of a random distribution are plotted in Fig. 4.8. It is seen that changes in the population with grain growth are difficult to distinguish from experimental deviations or fluctuations. Minor fluctuations in the low angle regime with grain growth end up being represented as relatively large differences when plotted in MRDs. As a result, it appears that there is a decrease in low angle boundaries with grain growth. However, it is more likely that experimental uncertainties are effecting determination of the MDF and that the distributions do not differ significantly from random. Number weighted-MDFs are also similarly inconclusive. These uncertainties likely vary within the misorientation space.
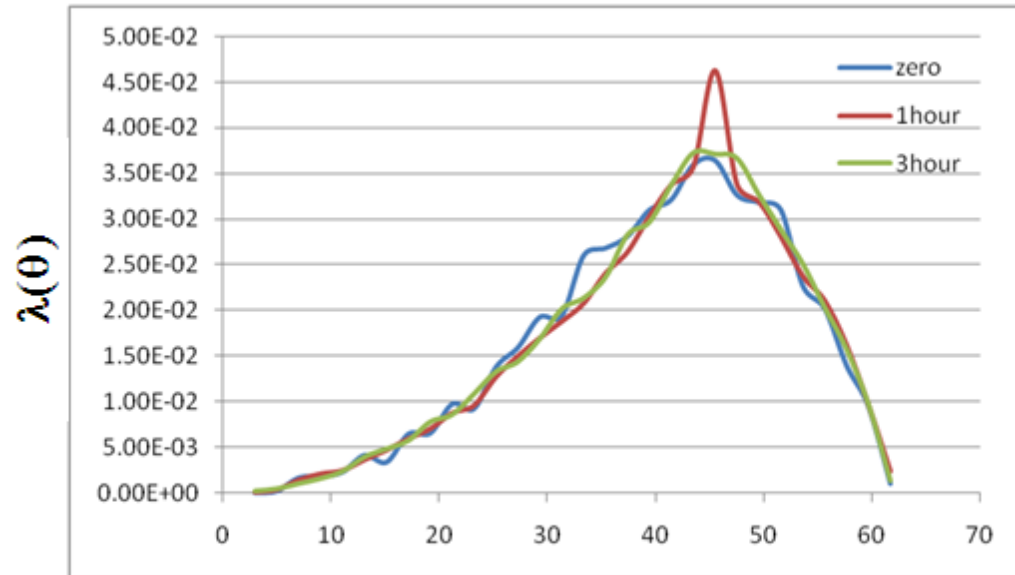
(a)
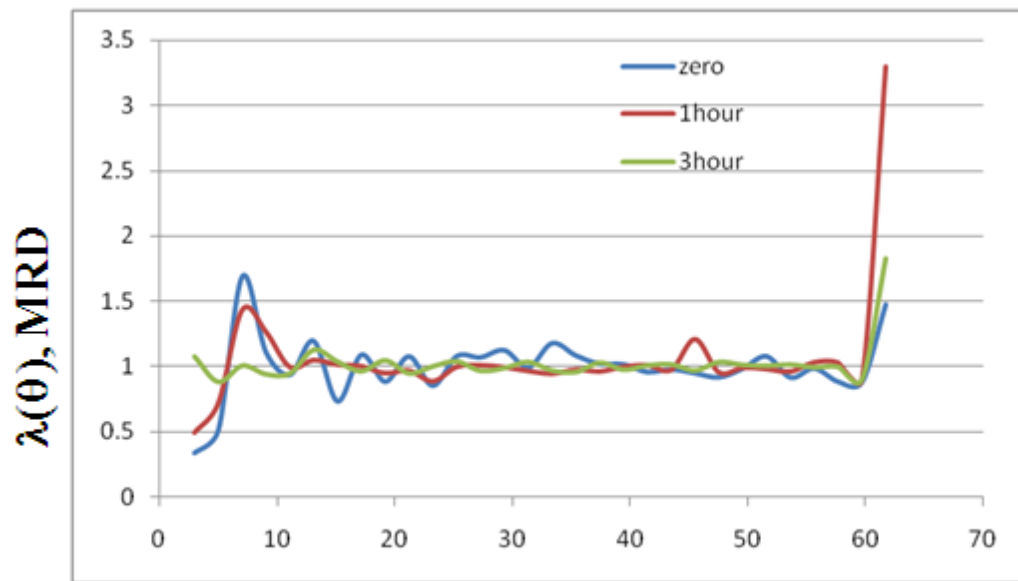
(b)

Figure 4.8 Area weighted MDFs for the zero hour, one hour, and three hour $SrTiO_3$ sample states, plotted as absolute population (a) and with respect to a random distribution (b). Minor fluctuations in population are reflected as relatively large peaks with respect to a random distribution. Trends in the MDF with respect to grain growth are inconclusive at best. Experimental uncertainties likely mask any real differences. A different technique is required in this case to understand differences in boundary population in misorientation space.

While calculating fractional differences in a bin-by-bin fashion, it is possible to fill a GBCD-like data structure with fractional differences in each bin instead of populations. This "fractional difference GBCD" can then be analyzed or plotted similarly to any other GBCD. By plotting the maximum and minimum of the deviation of the grain boundary plane populations for misorientations about fixed misorientation axes, it is possible to ascertain whether or not there are predictable trends in uncertainty with respect to misorientation. In Fig. 4.9, the maximum and minimum of the fractional difference GBCD are plotted for increasing misorientation about the [100], [110], and [111] misorientation axes for comparison of the two "three hour" datasets. While no clear trend with respect to misorientation is observed, it is noted that there are significant differences in the peak populations for both misorientation axis and angle. This analysis may also be misleading, because minima or maxima in fractional deviation may not correspond with actual peaks or locations of interest in the five parameter space. As for the one-dimensional case, it is impossible to establish a threshold guideline for experimental uncertainty based on such an analysis.
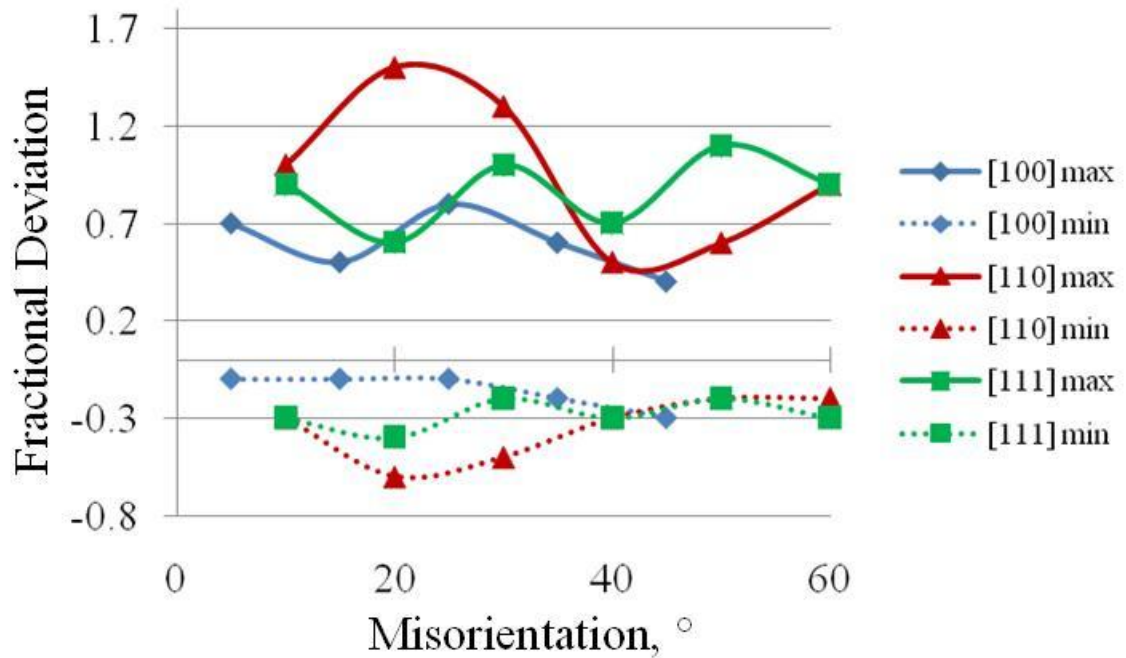
Figure 4.9 Maxima and minima fractional deviations in grain boundary plane population between two equal subsets of the "three hour" SrTiO3 dataset for specific misorientation axes with respect to misorientation . While there are no predictable trends, experimental uncertainty does vary appreciably with respect to misorientation axis and misorientation angle. It is decided that a three dimensional approach for analyzing uncertainty in the five parameter GBCD is inappropriate and no threshold guidelines can be established.

Clearly, comparisons based on one dimensional or three dimensional information

are insufficient for quantitative analysis of five parameter GBCDs. For quantitative

comparisons of GBCDs, it will be necessary to locate specific areas of interest in the five

parameter space and determine experimental uncertainties for those specific areas, based

upon all five parameters. This will be addressed in the next section.

4.2.3 Five Parameter GBCD Evaluation

Following our initial hypothesis, it is predicted that the five parameter GBCD
will evolve with grain growth in such a way that the population of higher energy
boundaries is preferentially decreased. The population of lower energy boundaries will
thus make up a greater fraction of the total boundary area, and their relative population
will increase. Thus, to test the hypothesis, it is necessary to locate boundary types whose
populations appear to be increasing or decreasing with grain growth. While the five
parameter space is very large, it is possible to consider some common misorientation axes
and angles based on previous observations and probe the grain boundary plane
populations at these locations as an initial attempt to locate such changing populations.
Typically, boundary plane populations are plotted at 10 ° misorientation angle increments
for [100], [110], and [111] misorientation axes. These plots are then visually compared
to identify locations in the five parameter space that may be worth investigating in more
detail. In this work, grain boundary plane populations for fixed misorientations are
plotted on stereographic projections along [001]. For every such plot presented in this
work, the [100] direction is to the right in the plane of the page. One such example is
presented in Fig. 4.10, where plots of $\lambda(n|20°/[111])$ for the zero (a) and three hour (b)
samples appear to show an enhancement of low angle boundaries bounded by one {100}
plane with grain growth. The population of these types of boundaries increases from a
frequency of 2.6 MRD to 3.2 MRD, an approximately 23 % increase.
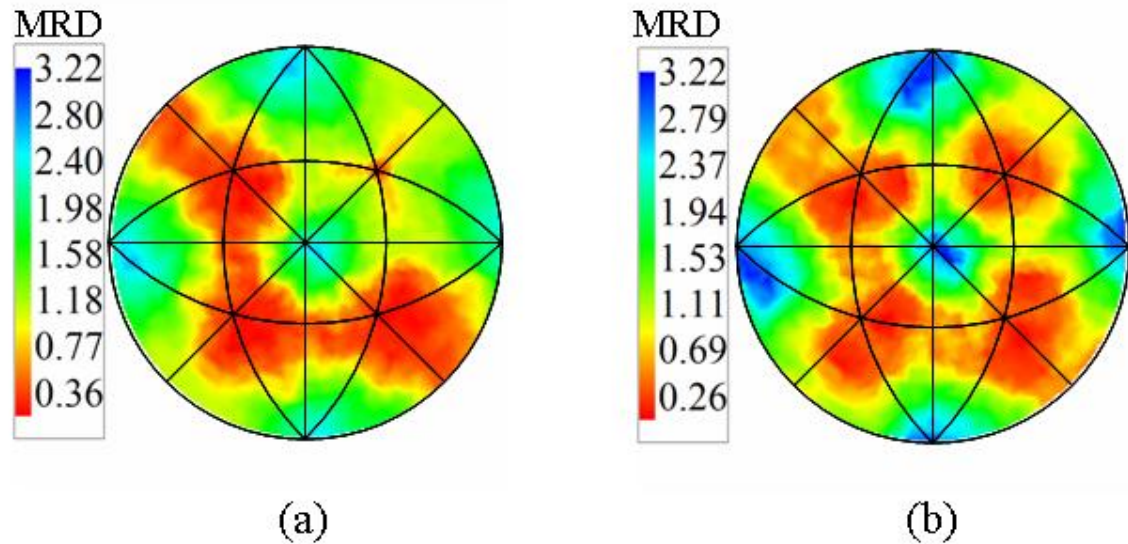
Figure 4.10 Plots of the grain boundary plane population for boundaries with a 20 ° misorientation around [111] for the zero and three hour $SrTiO_3$ samples. The population of boundaries with this misorientation that are terminated by {100} planes increases by approximately 23 %.

Of course, it is necessary to determine whether or not this difference is distinguishable from experimental uncertainty at this location within the five parameter space for these samples. To do this, the "fractional difference GBCD" is calculated for equal size, half-subsets of the "zero hour" and "three hour" datasets. The "fractional difference GBCD" is then calculated for the comparison of the full "zero hour" dataset with the "three hour" dataset. The population of fractional difference is then plotted for the fixed misorientation of interest – in this case, 20 °/[111]. Fig. 4.11 shows the fractional difference for boundary planes at this misorientation for the "zero hour" and "three hour" subsets, as well as for the comparison of the two datasets, plotted on the same scale. The absolute difference in MRD for boundaries with these fixed misorientations is plotted as well. From the analysis presented in Chapter 4, Section 4.2, it is known that the uncertainties within the two datasets are at least comparable, and that an additive effect does not appear to exist. That is, the amount of uncertainty in each

dataset is similar and the uncertainty does not increase when comparing the two full

datasets with each other. This makes it possible to observe the uncertainty for a specific

boundary type in each dataset and use this as a guideline to determine whether or not

differences observed when comparing the "zero hour" and "three hour" sample states are

distinguishable from experimental uncertainty. Considering the peak of interest – the

population of boundaries with this misorientation terminated by boundary planes near

{100}, it is observed that the fractional difference for the comparison of the "zero hour"

and "three hour" datasets is on the order of the differences found within each dataset.

Therefore, while the data suggests that the population of these boundaries is increasing

with time, it is not possible to make a definitive conclusion. It is observed that the

absolute difference in population for this boundary type in the two samples is

approximately 0.5 MRD (Fig. 4.11d).
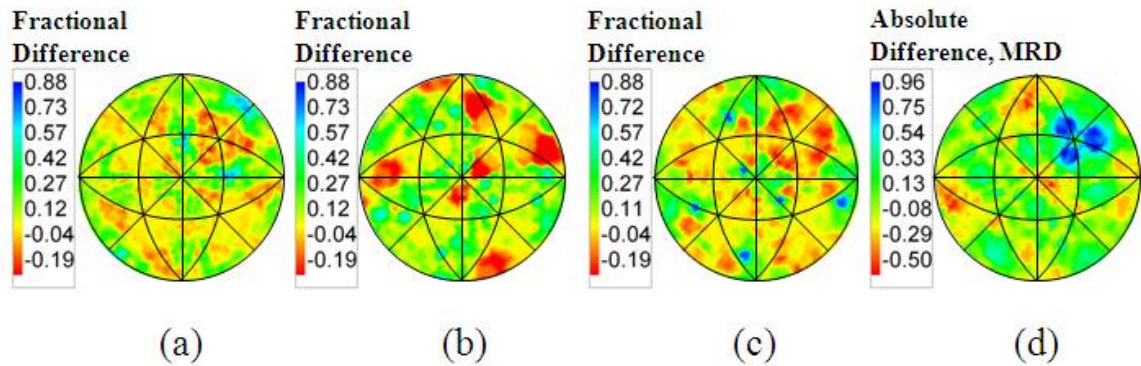
Fig 4.11 Fractional difference of boundary populations at a fixed misorientation of 20 ° / [111] for equal half subsets of the "zero hour" (a) and "three hour" (b) datasets, as well as for comparison of the "zero hour" and "three hour" full datasets (c). The absolute difference in MRD is plotted as well (d). The fractional difference between the "zero hour" and "three hour" datasets for the population of boundaries terminated by planes near {100} is nearly indistinguishable from experimental uncertainty.

An apparent decrease in population can be found in the higher angle regions of the space. An example can be seen in the distribution of grain boundary planes for bicrystals with misorientation of 60 ° around [111] for the zero, one and three hour samples (Fig. 4.12). When considering the distribution of grain boundary planes with the Σ3 misorientation, a dramatic difference between the samples is observed.
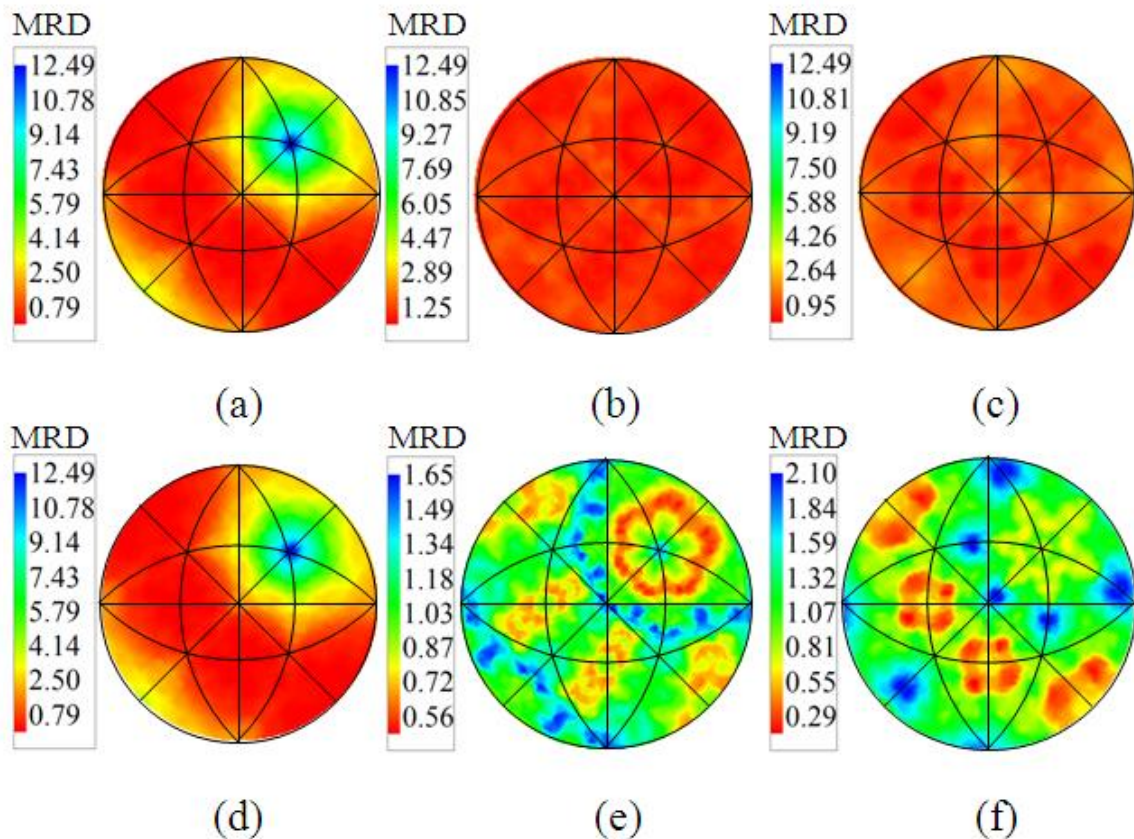
Figure 4.12 The distribution of grain boundary planes with a misorientation of 60 ° around [111] (Σ3 misorientation) are plotted on stereographic projections for the zero (a, d), one (b, e), and three hour (d, f) SrTiO$_3$ samples. Stereograms a-c are plotted on the same color scale and stereograms d-f are plotted so that the minimum of each distribution is represented by the color red and that the maximum is represented by the color blue. The population of boundaries with this misorientation that are terminated by {111} planes (coherent twins) decreases from 12.5 MRD to 0.8 MRD with grain growth.

In the zero hour sample, grain boundaries with a Σ3 misorientaton bounded by (111) planes, commonly referred to as coherent twins, are present with a frequency of

12.5 MRD. With grain growth, the population of this specific boundary type decreases to approximately 1.4 MRD in the one hour sample, and to approximately 0.8 MRD in the three hour sample. Again, fractional difference analysis should be employed to ensure that the perceived difference between the two datasets is distinguishable from experimental uncertainty at this location in the five parameter space.

In Fig. 4.13, the fractional difference is plotted for the fixed misorientation of interest, 60 ° / [111], for the half-subsets of the "zero hour" and "three hour" datasets, as well as for the comparison of the two full datasets. Considering the fractional difference at the location of the coherent twin – boundaries of this fixed misorientation terminated by (111) planes – it is obvious that the perceived decrease in population of coherent twin boundaries is indeed discernable from experimental uncertainty and is, therefore, real. The experimental uncertainty within each dataset for this boundary type is actually very near 0 %, while the fractional difference between the two datasets represents an almost 70 % decrease. Averaging in the binning procedure for plotting the stereogram results in a slight under-representation of the decrease for this specific boundary type.
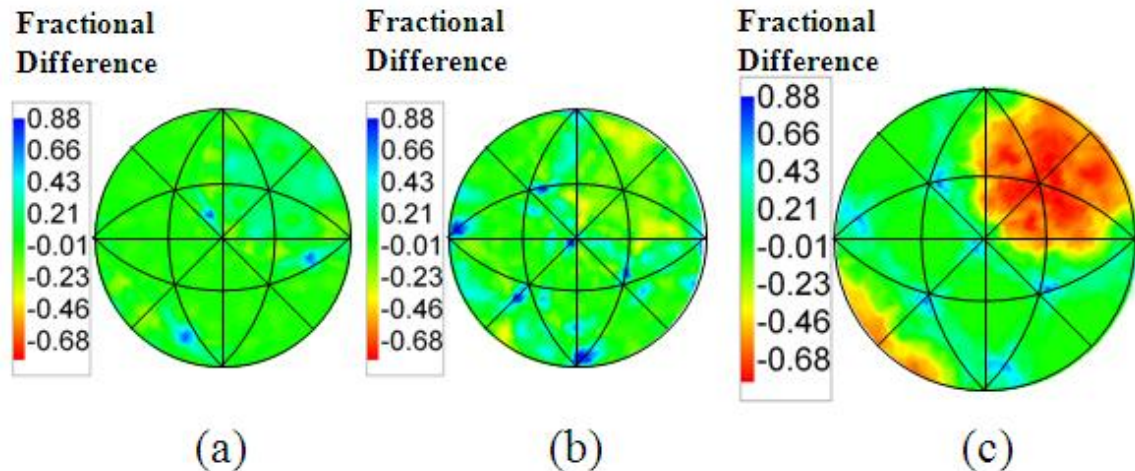
Fig. 4.13 Fractional difference of boundary populations at a fixed misorientation of 60 ° / [111] for equal half subsets of the "zero hour" (a) and "three hour" (b) datasets, as well as for comparison of the "zero hour" and "three hour" full datasets (c). The fractional difference between the "zero hour" and "three hour" datasets for the population of coherent twins, boundaries terminated by (111) planes, is definitely distinguishable from experimental uncertainty within the two datasets at this specific boundary. The observed decrease in the population of boundaries of this type with grain growth is determined to be real.

During the grain growth experiment, total grain boundary length/area decreased by approximately 80 %, while the length/area of $\Sigma 3$ boundaries decreased by approximately 83 %. It is obvious that the GBCD is not random in our initial condition and that the five parameter GBCD evolves with grain growth. While coherent twins are prevalent in low stacking fault energy metals such as copper, it appears that they are a relatively unfavorable boundary configuration for $SrTiO_3$ and are being eliminated with grain growth. Although the statistics are rather limited, this has been observed experimentally in other work as well [34]. In the work by Cockayne [34], however, grain boundary plane orientation was not considered. It was only observed that all $\Sigma 3$ boundaries decreased with grain growth.

4.2.4 Relative Grain Boundary Energies and the Correlation with Grain Boundary Character

To test the idea that coherent $\Sigma 3$s are being eliminated because they have relatively higher energy, it is necessary to measure relative grain boundary energies.

For one technique of measuring relative grain boundary energies in $SrTiO_3$, another sample (sample two) was created as described in Chapter 3, Section 4. Sample one refers to the sample used for the GBCD evolution experiments. The population of coherent twins in this second sample was found to be approximately 4 MRD. The combined results from the two $SrTiO_3$ samples are shown in Fig 4.14, comparing the population of coherent twins at various times during grain growth. This comparison shows that the high $\Sigma 3$ population was not an anomaly of the original sample, and that the second sample has a population of coherent twins that is consistent with the original sample.
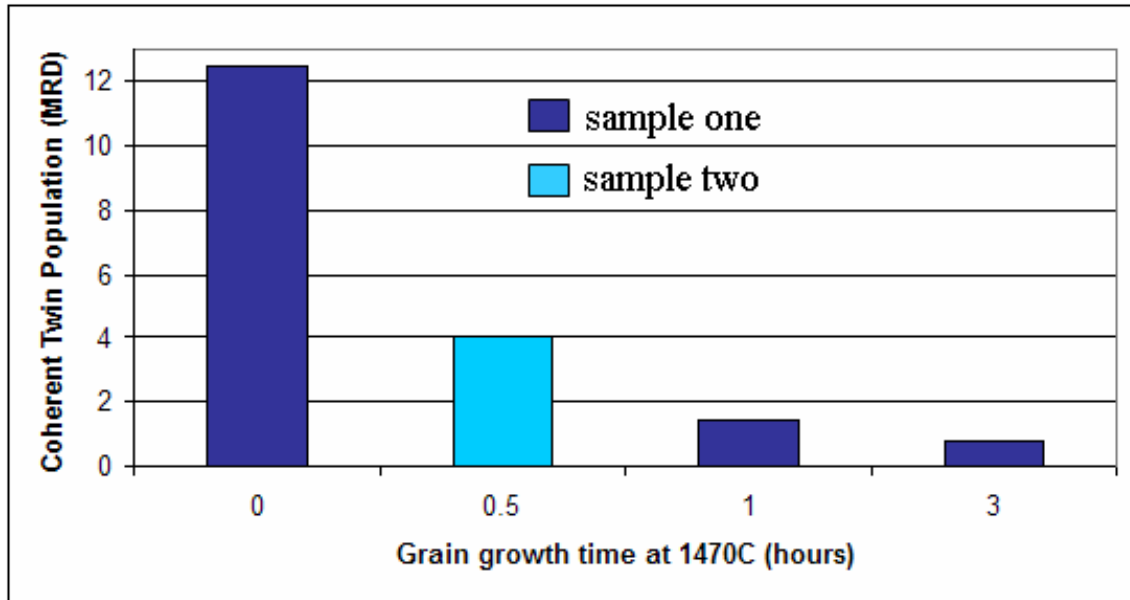
Figure 4.14 The population of coherent twins, in units of MRD, found in two $SrTiO_3$ samples at several times during constant temperature grain growth. The population of coherent twins decreases dramatically with grain growth. The population of coherent twins for a second similar $SrTiO_3$ sample is consistent with the first sample which suggests that the observation is not an anomaly confined to one sample.

The thermal-groove geometry based technique for determining relative grain boundary energies is admittedly susceptible to inconsistencies, especially when dealing with samples that are comprised of small grains or exhibit a tendency for surface faceting at the temperatures used for thermal grooving. These issues make accurate determination of the groove profile challenging. Unfortunately, both of these issues are a factor for the $SrTiO_3$ sample used in this analysis. It is therefore useful to visually compare actual groove profiles to see what effects these issues may have on groove profile determination. In Fig. 4.15, example groove profiles are plotted for random, incoherent and coherent $\Sigma 3$ boundaries. The grooves are certainly not ideal – there is evidence of faceting and it is challenging to pinpoint the maxima of the humps which are used to determine the groove width. It is likely that these effects contribute to experimental

uncertainty in the results. However, it is observed that the groove profile for the coherent

$\Sigma 3$ boundary shows the deepest trough. This suggests the conclusion that coherent $\Sigma 3$

grain boundaries have the highest relative grain boundary energies.
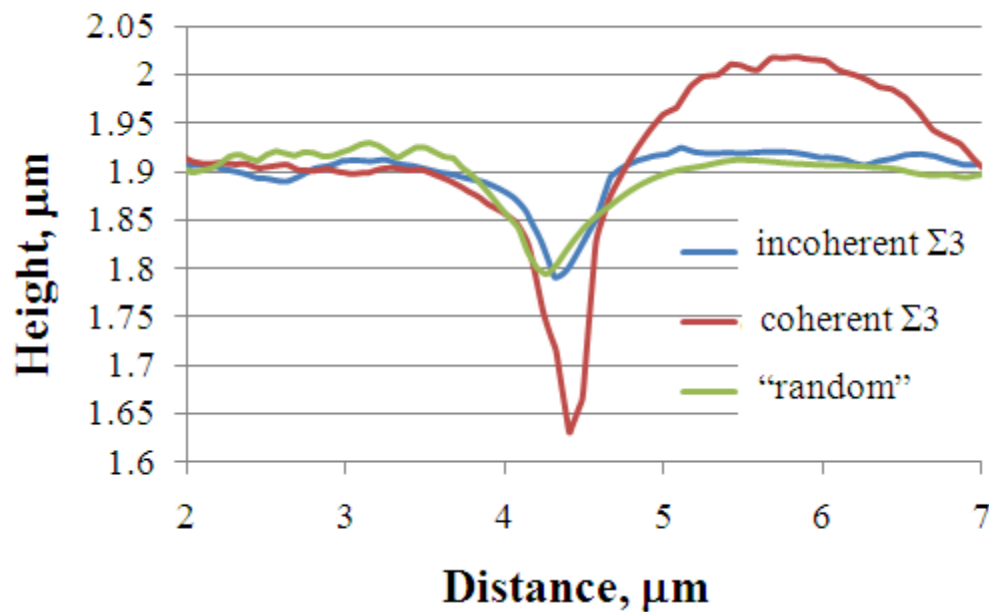
Fig. 4.15 Example grain boundary groove profiles for random, incoherent and coherent $\Sigma 3$grain boundaries, as measured with an AFM. The profiles show inconsistencies which can affect the accuracy of the technique. However, the relatively deeper trough of the coherent $\Sigma 3$ grain boundary groove profile suggest the conclusion that coherent $\Sigma 3$ grain boundaries have the highest relative grain boundary energies.

Assuming that the surface energy is constant, it is possible to plot cumulative

probability plots of the γ_{gb}/γ_s ratio for qualitative comparison of the grain boundary

energy anisotropy. As seen in the plot in Fig. 4.16, the lowest γ_{gb}/γ_s ratio recorded for a

coherent $\Sigma 3$ boundary is higher than 75 % of the recorded values for incoherent $\Sigma 3$

boundaries. Mean values are reported in the chart in Fig. 4.17.
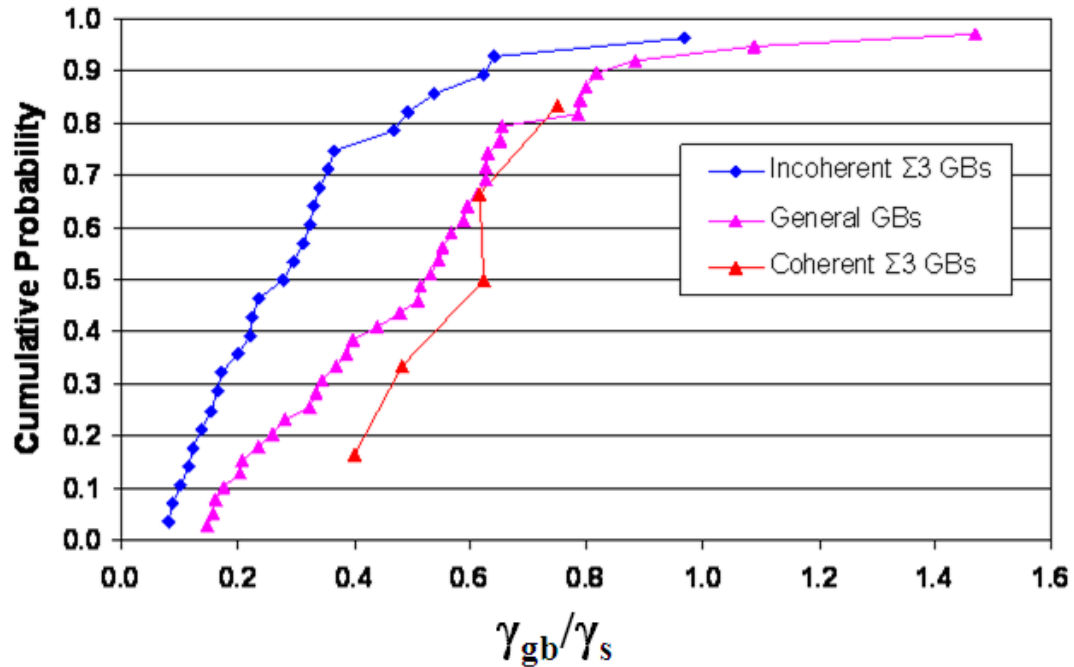
Figure 4.16 Cumulative probability plots of the relative grain boundary energy (γ_{gb}/γ_s) for incoherent $\Sigma 3$, general, and coherent $\Sigma 3$ grain boundaries in $SrTiO_3$, as determined by AFM measurements of thermal groove geometries. Generally speaking, incoherent $\Sigma 3$ boundaries have lower relative energies than general boundaries, or coherent $\Sigma 3$, which have the highest relative grain boundary energies.

The mean γ_{gb}/γ_s ratios show that, on average, the energies of coherent $\Sigma 3$ boundary energies are greater than the energies of general boundaries, while incoherent $\Sigma 3$ boundaries have are the lowest recorded energies.
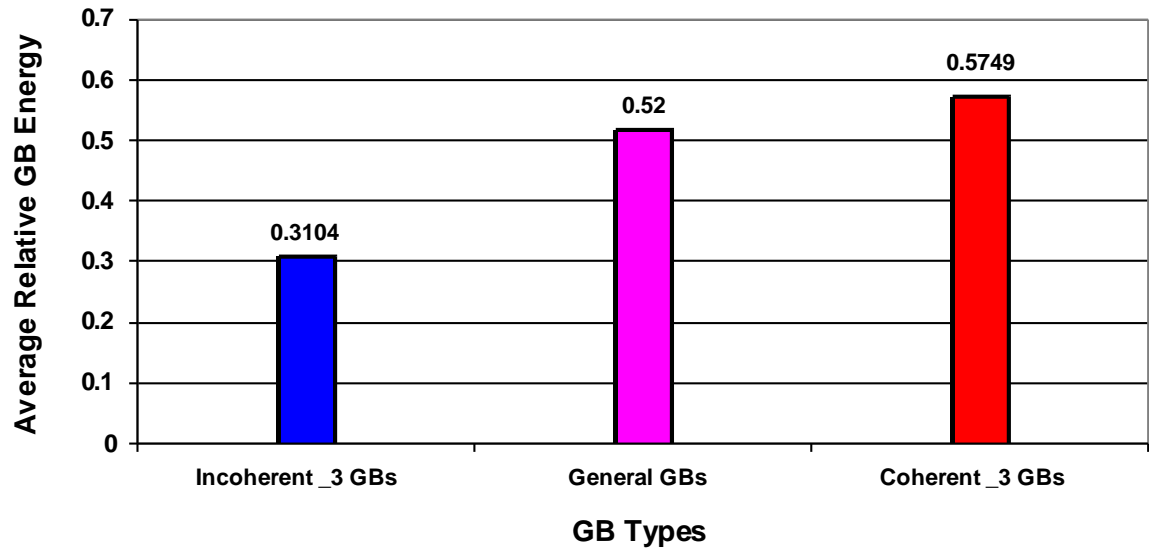
Figure 4.17 Mean values of the relative grain boundary energy (γ_{GB}/γ_s) for incoherent $\Sigma 3$, general, and coherent $\Sigma 3$ grain boundaries in $SrTiO_3$. Incoherent $\Sigma 3$ boundaries were found to have the lowest mean relative grain boundary energy. The average relative grain boundary energy of general boundaries was higher, and the average energy of coherent $\Sigma 3$ was found to be the highest of the three categories.

Relative grain boundary energies can also be determined with a serial-sectioning based technique. For this work, a dual-beam focused ion beam (FIB) (instrument details) was used for sectioning and orientation imaging to reconstruct the 3-D microstructure, including orientation information, of a $SrTiO_3$ sample. The sample for this experiment was created from the same powder and using similar techniques as described in Chapter 3, Section 3.4. Relative grain boundary energies were determined using similar techniques as those presented by Dillon and Rohrer [78].

For reasons similar to those presented in Chapter 4, Section 2.3, it is challenging to quantitatively compare five parameter grain boundary energy and character distributions. It is most straightforward to visually compare populations for specific locations within the five parameter space. For this analysis, calculated grain boundary

energy distributions can be compared to the grain boundary populations calculated at previously identified locations of interest in the five parameter space. In Fig. 4.18, the calculated relative grain boundary energies are compared to grain boundary populations for boundaries misoriented 20 ° and 60 ° about the [111] axis – boundaries that were highlighted in Chapter 4, Section 2.3 as boundaries that showed likely appreciable change with grain growth. In the case of boundaries with a 20 °/[111] misorientation axis, a local minima is observed in the energy distribution for boundaries terminated with near-{100} planes. The perceived increase in the population of this type of boundary is very near the experimental limit, but the trend of an inverse correlation between boundary population and energy is observed, even at the limit of detection. This correlation is even more obvious when considering the energy and population of coherent twins in $SrTiO_3$. In Fig. 4.18 (c) and (d), the relative grain boundary energy and grain boundary population is plotted for boundaries with a 60 ° / [111] misorientation. As previously mentioned, the population decrease of boundaries of this misorientation that are terminated by (111) planes – the coherent twin – is well above the detectable limit for this boundary type. It is observed that this boundary type has one of the highest relative grain boundary energies in the system.
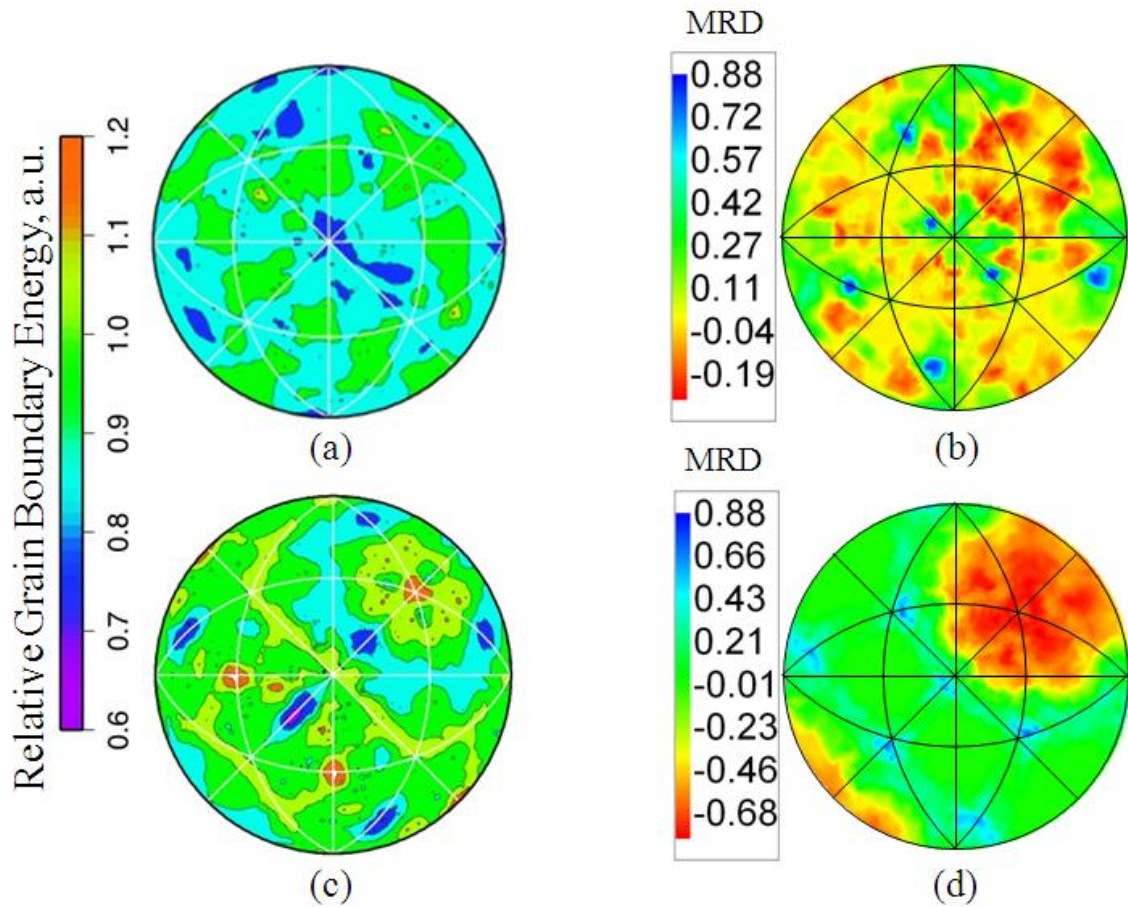
Fig. 4.18 Relative grain boundary energy and population distributions for boundaries with 20 ° / [111] (a,b) and 60 ° / [111] (c,d) misorientations. In general, boundary types that are of low relative grain boundary energy correspond to boundary types that are increasing in population with grain growth, and vice-versa. This is especially obvious for the coherent twin, which experiences the largest decrease with grain growth, and is the highest relative energy boundary. An inverse correlation between boundary energy and population is observed in the full five parameter space.

4.3 Discussion

The initial hypothesis of the five parameter grain boundary energy anisotropy determining the evolution of the five parameter grain boundary character distribution was tested. The assumptions of a scale invariant grain size distribution with grain growth and an initially random GBCD were not observed experimentally. Abnormal grain growth may complicate some of the observations, but it is assumed that the high fraction of "small" grains that are included in the zero hour dataset dominate the observed properties of the GBCD. Also, it is difficult to know if the GBCD is ever truly random for a ceramic sample formed by conventional powder processing, or if this state can be captured experimentally. There is no one instant in which the sample ceases to be a powder compact and becomes a 100 % dense body. Nevertheless, the analysis of the evolution of the GBCD with grain growth in $SrTiO_3$ has led to important observations.

The grain boundary plane distribution, $\lambda(\mathbf{n})$, was observed to evolve to an anisotropic steady state which favors low energy {100} boundary planes. {100} boundary planes occur with a frequency approximately two times random (2 MRD) even at the earliest recorded time step. It is assumed that this state is achieved very early in the sintering/grain growth process. A statistically indistinguishable steady state $\lambda(\mathbf{n})$ is maintained throughout observed grain growth in which the gain size increases by nearly a factor of ten.

There are very few grains in the "zero hour" sample that survive in the "three hour" sample. This is the result of a complicated combination of many critical events that occur during the continuous elimination of interfacial area during grain growth to reduce total energy of the system. While the population of boundary planes remains

statistically indistinguishable during grain growth, there are obviously many changes to the microstructure. It is also known that it is a combination of misorientation and boundary plane orientation that determines the properties of a grain boundary. In the initial observed microstructure, coherent twins (grains separated by a 60 °/ [111] misorientation and bounded by (111) planes) occur with a frequency of more than 12 times random in the anisotropic distribution. These boundaries may be present initially in polycrystalline powder agglomerates or may be caused by the compaction process. Attempts were made to analyze the raw powder with TEM, but the results were inconclusive. It was found that coherent twin boundaries in $SrTiO_3$ on average have higher grain boundary energies than general boundaries. This result was determined from both grain boundary groove measurements and FIB serial sectioning. This is fully consistent with the hypothesis that grain boundary energy anisotropy is driving the evolution of the GBCD during grain growth and higher energy boundaries are being eliminated in preference for lower energy boundaries. The grouping of "incoherent" $\Sigma 3$ boundaries was found to have the lowest average relative grain boundary energy. While this may have some yet unknown significance, it should be pointed out that the grouping of "general" boundaries contains every boundary that is not a coherent or incoherent $\Sigma 3$ boundary; there is every reason to assume that this grouping contains some boundaries that are very high in energy and some that are very low, as well as those that span the range. There is no current understanding of what the lowest or highest energy boundary configuration in $SrTiO_3$ might be. This particular classification of boundaries was selected because they were readily identifiable using the TSL OIM 4.6 software.

That the coherent twin in $SrTiO_3$ is a relatively high energy boundary is very different than the case of low-stacking fault energy cubic metals. While this is inconsistent with other materials, it is consistent with the results if a "sum of surface energies" approach is adopted to infer relative grain boundary energies, as {111} are the high energy planes in $SrTiO_3$ [13]. It has also been verified with two independent methods. Presumably, this is the result of surface termination/charge compensation issues. A coherent twin in $SrTiO_3$ would require SrO_3 or Ti termination. Charge may be balanced in the interface plane, but the second-nearest neighbors are likely in non-equlibrium positions. This may lead to an unbalanced charge and seemingly results in a high energy configuration. The role of coherent (and incoherent) $\Sigma 3$ boundaries in the context of grain boundary engineering of nickel is expected to be different and will be specifically addressed in the Chapter 6.

Chapter 5

5. Influencing the GBCD with Doping in MgO

5.1 Introduction

Experimental and simulation results suggest that anisotropy develops in the area and number weighted MDF with curvature driven grain growth [80]. In general, low angle, low energy boundaries occur more frequently than in a random distribution. This is a result of both the preferential elimination of higher energy grain boundaries and the increase in area of lower energy boundaries. A steady state distribution develops during simulations. The number and area weighted MDF is calculated for a 3000 ppm Ca-doped MgO sample at a representative point in time during grain growth to experimentally test these results.

Changing the chemistry of a ceramic system has been shown to change the anisotropy of the GBCD [50]. In this work, a 3000 ppm Ca-doped MgO sample was prepared for experimental study of the change in the GBCD with doping. Results will be compared to those for a nominally pure MgO sample. Representative [001] inverse pole figure orientation maps for both the doped and undoped MgO samples are shown in Fig. 5.1. It is expected that grain boundary energy anisotropy will drive the formation of the anisotropic GBCD and that doping will change the grain boundary energy anisotropy, and thus the GBCD, in MgO. An anisotropic distribution should form in a similar manner to that of $SrTiO_3$ (Chapter 4) from an initially isotropic condition and should show eventual statistically self-similar behavior. AFM measurements of thermal grooves

in both nominally pure and 3000 ppm Ca-doped MgO are used to determine and compare

relative grain boundary energies in the two samples to support the claim that variations in

energy anisotropy at least partially explain observed variations in anisotropy of the five

parameter GBCD.
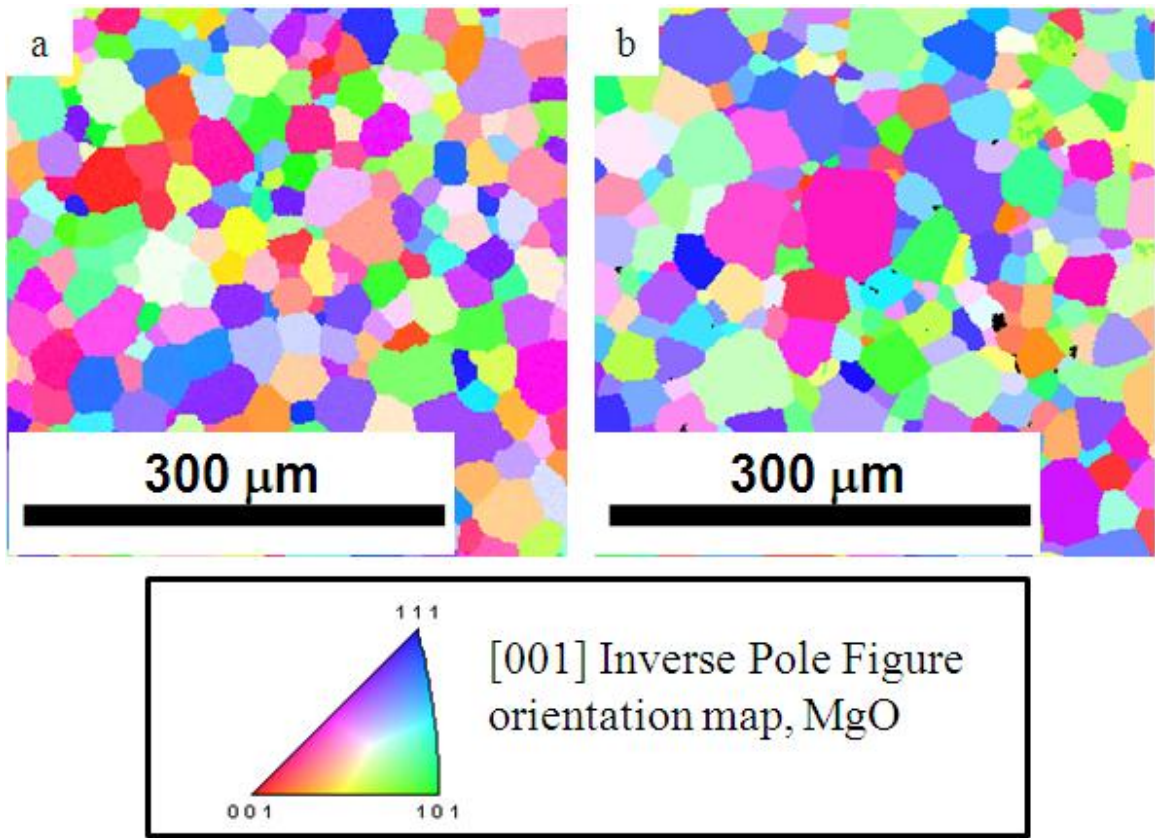
Figure 5.1 Representative [001] inverse pole figure orientation maps for the undoped (a) and 3000 ppm Ca-doped MgO samples studied in this work. Average grain size is approximately the same for each material.

5.2 Results

5.2.1 MDF Formation

The area and number weighted MDF as a function of disorientation was calculated for more than 40,000 grains for a 3000 ppm Ca-doped sample. An enhancement at low angle boundaries was observed for both. The area-weighted MDF, $\lambda_A(\theta)$, and the number-weighted MDF, $\lambda_N(\theta)$, are plotted in units of MRD with respect to disorientation angle in Fig. 5.2. The two points at lowest disorientation angles are likely artificially low because of undersampling in the measurement. These results are comparable to simulation results [80].
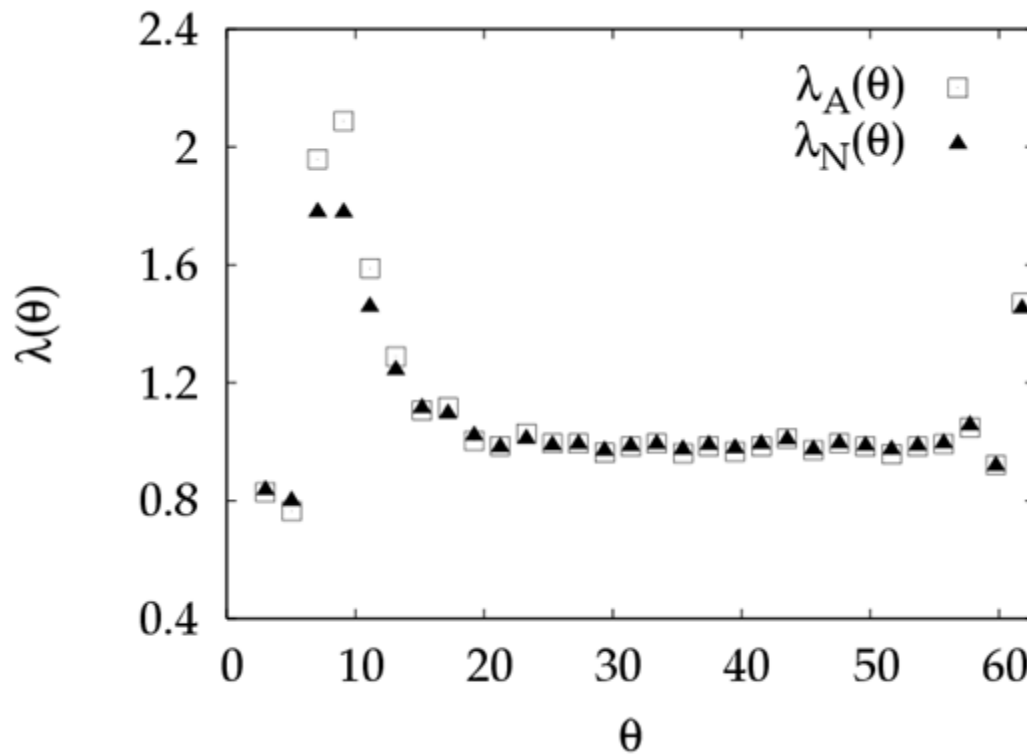
Figure 5.2 Area- and number-weighted MDF calculated from greater than 40,000 grains for a 3000 ppm Ca doped MgO sample. An enhancement is observed in both for low angle boundaries.

5.2.2 GBPD Variation with Doping

The GBPD was determined for the 3000 ppm Ca-doped MgO sample. An

anisotropic misorientation-independent grain boundary plane distribution is observed. A

maximum is observed for {100} boundary planes, which occur with a frequency more

than two times a random distribution. When compared to the GBPD of a nominally pure

MgO sample with a similar grain size prepared in the same manner (from Papillion), it is

obvious that the GBPD is more anisotropic in the doped sample (Fig. 5.3). The

population of grain boundaries terminated by {100} type planes nearly doubles. The

population increases from 1.16 MRD, which is only slightly more anisotropic than a

random distribution, to 2.34 MRD.
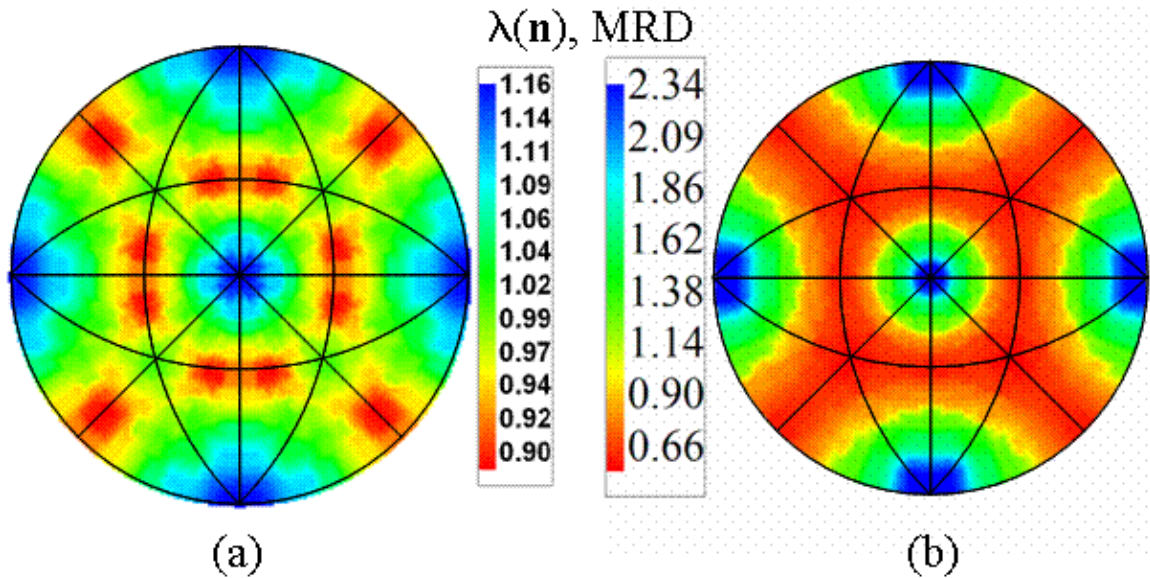
Figure 5.3 $\lambda(n)$ for a nominally pure MgO sample with $<d> = 24$ μm (a) (Papillion) and for a 3000 ppm Ca-doped MgO sample with $<d> = 22$ μm (b). The doped sample shows significantly more anisotropy in the GBPD.

5.2.3 GBCD Variation with Doping

Just as a change in the grain boundary energy distribution as a result of doping may lead to a change in the GBPD, it should also lead to changes in the five parameter GBCD. Plotting of specific slices of the five parameter space is required to test this hypothesis. Representative examples of grain boundary populations at fixed misorientations about [100], [110], and [111] misorientation axes are shown in Figs. 5.4 and 5.5. It is observed that while the GBPD for the undoped MgO sample is nearly isotropic, there is appreciable anisotropy in the five parameter GBPD (Figs. 5.4 and 5.5 a and b). When considering grain boundary misorientations that favor {100}-type termination planes (Fig. 5.4), an increase in population with doping is observed, as expected from the GBPD analysis. For grain boundaries with a 50° misorientation about [100], boundaries terminated by {100} planes increase by nearly a factor of 1.7, for

example. It is also observed that for fixed misorientations that favor boundary terminations other than {100} type planes, populations either decrease or change termination preference entirely with Ca doping in MgO. Fig. 5.5 shows $\lambda(n|30\,°/[111])$ (a,b) and $\lambda(n|60\,°/[111])$ (c,d) for the undoped and doped MgO. A {111} termination plane is favored for these misorientations in the undoped material. A decrease in the population of {111} terminating planes is observed for the 60 ° misorientation, and a change in boundary plane termination preference from {111} type to {100} type is observed for 30 ° misorientation. The trends at these specific fixed misorientations are characteristic of other points in misorientation space.
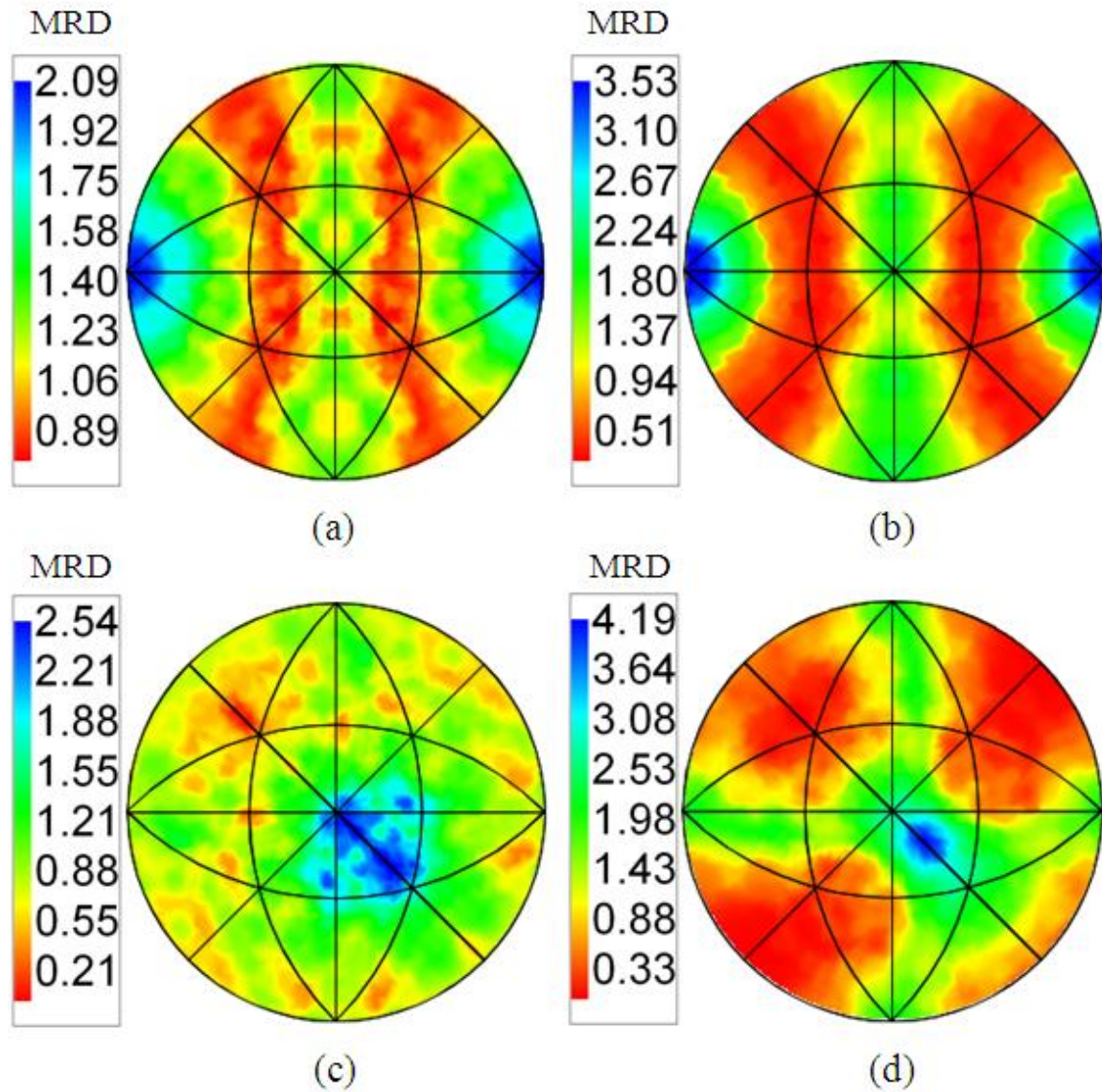
 Figure 5.4 Distribution of grain boundary planes for undoped MgO for fixed misorientations of 50 °/[100] (a) and 50 °/[110] (c), and for 3000 ppm Ca-doped MgO for fixed misorientations of 50 °/[100] (b) and 50 °/[110] (d). An increase in population of boundaries terminated by {100} planes is observed with doping.
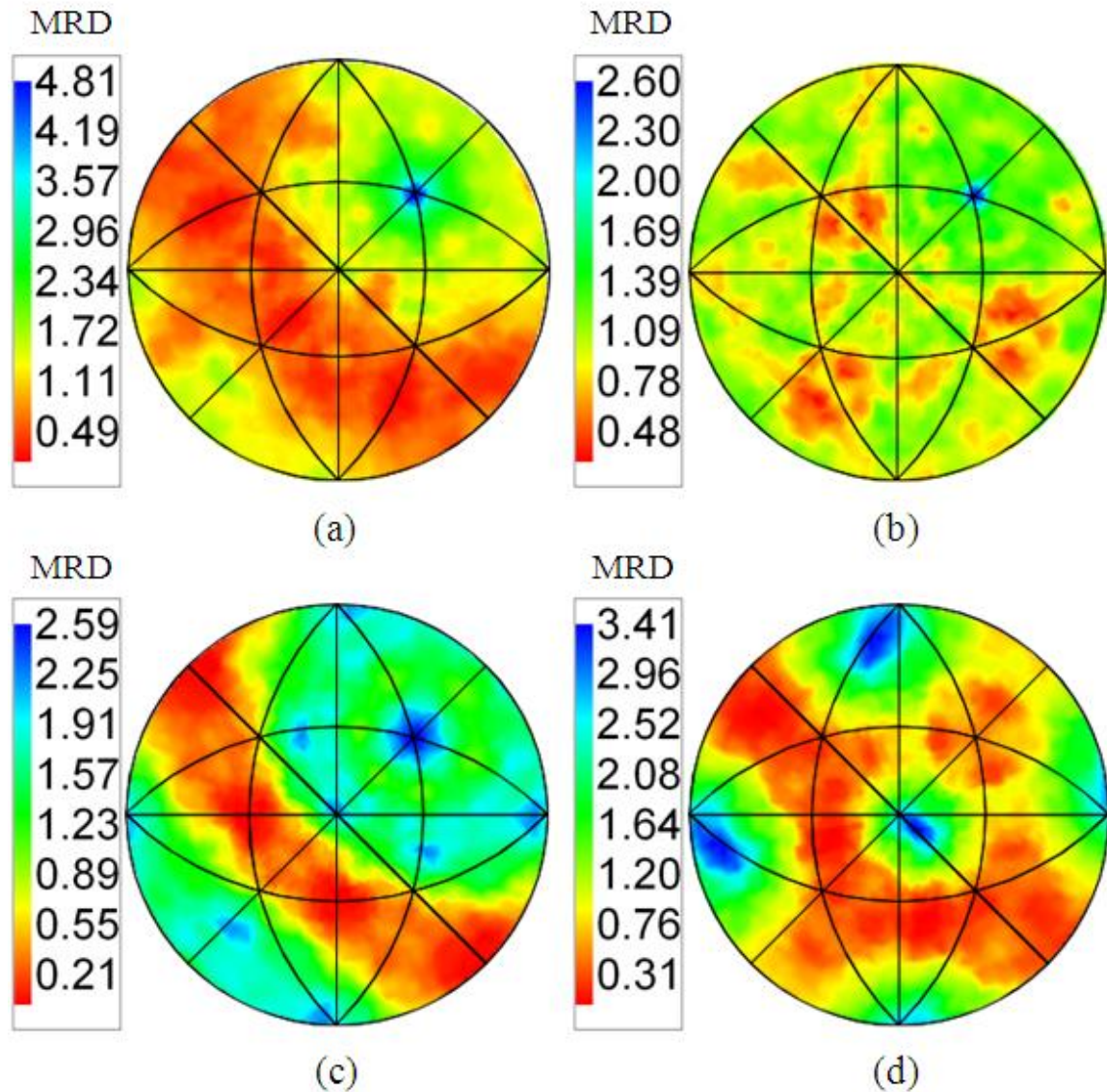
Figure 5.5 Distribution of grain boundary planes for undoped MgO for fixed misorientations of 30 °/[111] (a) and 60 °/[111] (b), and for 3000 ppm Ca-doped MgO for fixed misorientations of 30 °/[111] (c) and 60 °/[111] (d). A decrease in boundaries terminated with {111} is observed for these fixed misorientations with doping. For a fixed misorientation of 30 °/[111], the preference for boundary termination clearly changes from {111} type planes to {100} type planes.

5.2.4 Relative Grain Boundary Energies and the Correlation with Grain Boundary Character

To determine if a change in the grain boundary energy anisotropy can be used to explain differences in the GBCD with doping, relative grain boundary energies must be measured. If grain boundary population and energy are correlated as expected, the grain boundary energy distribution for the doped MgO should be more anisotropic than for the undoped MgO. Using the method described in Chapter 3, Section 7, the geometries of thermal grooves were measured to calculate relative grain boundary energies. Cumulative probability plots (Fig. 5.6) show that the grain boundary energy distribution is indeed more anisotropic in the doped sample as evidenced by the width of the distributions. A wider distribution corresponds to a more anisotropic distribution. Although the statistics are limited, these results are consistent with the correlation between relative grain boundary energy and population observed for $SrTiO_3$ as presented in Chapter 4, Section 2.4.
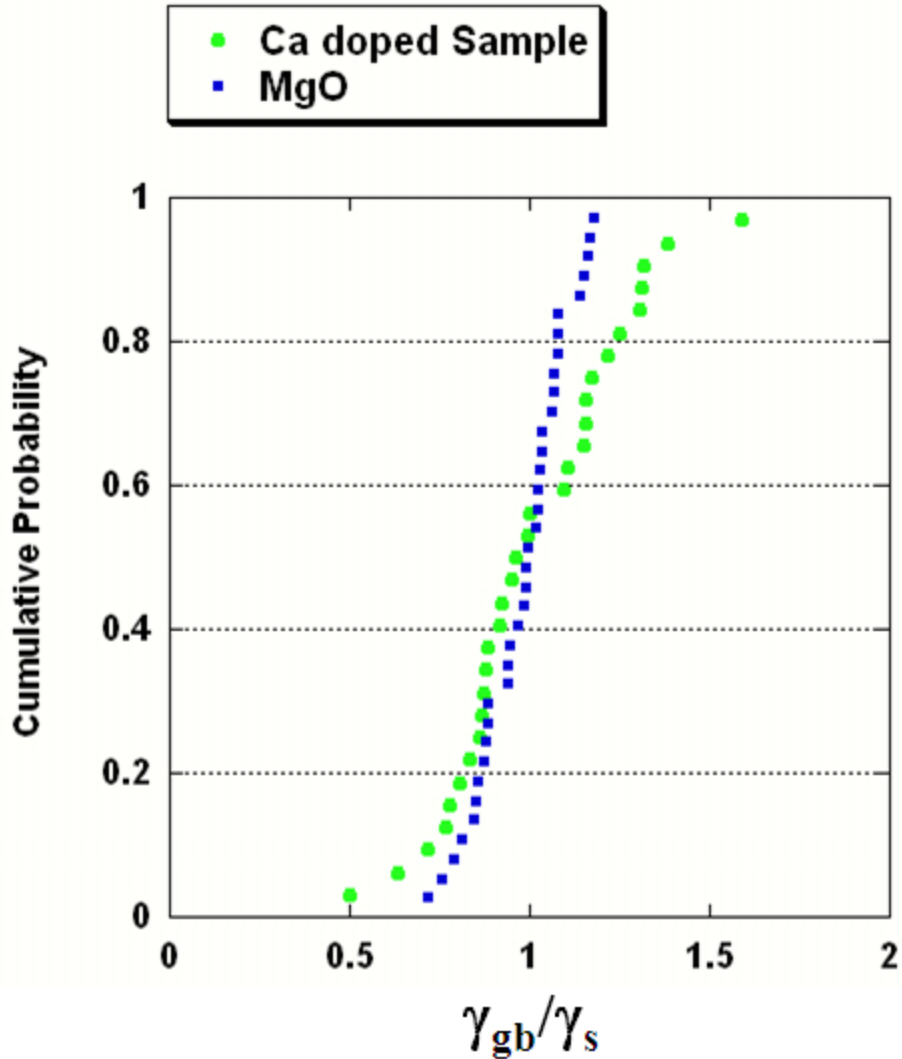
Figure 5.6 Cumulative probability plot of the relative grain boundary energies for a 3000 ppm Ca doped MgO and an undoped MgO sample. A wider distribution of relative grain boundary energies is found for the Ca doped sample, indicating and increase in grain boundary energy anisotropy with doping.

5.3 Discussion

As expected, anisotropic number- and area-weighted MDF forms with grain growth in 3000 ppm Ca-doped MgO. Both MDFs show a preference for low angle, presumably low energy boundaries. To better understand the role that grain boundary energy has in determining the GBCD of a sample, GBCDs and relative grain boundary

energy distributions were determined for undoped and 3000 ppm Ca-doped MgO. An increase in anisotropy was observed in the GBPD with doping. While it has not been determined how the grain boundary energy distribution has changed with doping, it is clear that it has changed and that this change has influenced the GBPD. Specifically, {100} grain boundary termination planes appear to be stabilized with Ca doping in MgO. This observation is further supported by analysis of five parameter GBCD changes with doping. For specific misorientations such as 50 °/[100] and 50 °/[110] at which undoped MgO favors {100} boundary plane termination, an increase in population is observed for {100} boundary planes with doping. It is expected that the energy of these boundaries are relatively lowered with doping. For misorientations such as 30 °/[111] and 60 °/[111], at which pure MgO favors {111} boundary plane termination, a relative decrease in population is observed for {111} boundary planes with doping. In fact, for a fixed misorientation of 30 °/[111], the location of the maxima changes from {111} type planes to {100} type planes. While it is not possible to directly correlate grain boundary population and grain boundary energy with the results presented for doped and undoped MgO, it is expected that the inverse correlation between energy and population as observed in many other ceramic systems should hold true. Thus, it is concluded that doping in MgO changes the relative grain boundary energy distribution such that boundaries with {100} termination planes are of relatively lower energy and are thus favored with grain growth during processing. It is uncertain whether or not {111} planes have lower relative energy in the pure material and exactly why they initially have a higher relative population. For MgO, calcium doping increases the width of the relative grain boundary energy distribution as well. This corresponds to an increase in observed

anisotropy in the grain boundary plane distribution. It should be noted that the case of calcium doping in MgO appears to be slightly different than for niobium doping in TiO_2 [50]. While in each case the GBCD anisotropy increases with doping, the relative grain boundary energy anisotropy was seen to decrease with Nb doping in TiO_2. Relative grain boundary energies were not directly measured in the TiO_2 study. Rather, surface energies were measured and grain boundary energies were inferred by assuming that the sum of the energies of the two surfaces that comprise a grain boundary adequately approximates the grain boundary energy. Keeping in mind the fact that two different techniques were used to determine relative grain boundary energies in the TiO_2 work and that a full five parameter description of the relative grain boundary energy was not determined for MgO in this work, it is unclear whether these results contradict each other or not. It is clear that doping can affect relative grain boundary energy and GBCD formation. If it is known how doping affects the grain boundary energy in a system, doping can be used as an effective means to control the GBCD.

Chapter 6

6. Grain Boundary Engineering of Nickel

6.1 Introduction

Iterative thermo-mechanical processing has been shown to influence the five

parameter GBCD for fcc metals [20, 21]. This has been shown to improve or affect some

materials properties [53-57]. It is proposed that such processing is altering the

connectivity of the random grain boundary network, replacing boundaries with relatively

poor properties with boundaries that have better properties [53-61]. According to the

central hypothesis of this dissertation, the grain boundary energy will play a role in

determining the GBCD with processing. Globally, a lower energy state should be

reached with iterative thermomechanical processing. "Configurational constraints," or

geometric/crystallographic limitations placed on the grain boundary network because of

the extensively twin- related microstructures typically found in these materials, will have

an effect on the evolution of the GBCD with GBE processing as well. However, how the

competing factors of maximizing the number of low energy boundaries while satisfying

crystallographic and energetic constraints at the junctions influence the GBCD is not

understood and will be explored in this work. Iterative thermo-mechanical processing

has been employed to study the evolution of the GBCD with GBE processing. The

GBCD was compared for reference and GBE states for both commercially available

(Integran) and high purity nickel. While it was instructive to complete the GBCD

evolution and grain boundary network connectivity experiments on the commercially

available Integran samples, these experiments were not ideal because the details of the

thermo-mechanical processing history of the samples were unknown. For more controlled experiments, it was decided to attempt to "grain boundary engineer" high purity nickel in house and complete a similar analysis.

Previous research ascribes property enhancements with GBE in fcc metals to increases in $\Sigma 3^n$ boundaries (where n = 1, 2, or 3) during processing [53-61]. As a result, the length and number fractions of $\Sigma 3^n$ boundaries and general boundaries in reference and grain boundary engineered states are studied in depth in this work. Of particular interest are the fractions normalized per area. Normalizing by area will show whether these "special boundaries" are replacing general boundary area with processing. For example, while it is well known that coherent $\Sigma 3$ twins in fcc metals are low energy boundaries, merely increasing grain boundary density by adding coherent twins to a microstructure is expected to have little effect on materials properties, as these boundaries do not necessarily modify the network of boundaries or replace boundaries which may have "worse" properties. It has also been reported that increases in the $\Sigma 3^n/\Sigma 3$ ratio are more important than increases in the fraction of $\Sigma 3$ boundaries alone to determining materials properties [61]. This ratio will be calculated before and after thermomechanical processing for both the commercially available and high purity nickel samples.

As mentioned multiple times in this work, the description of grain boundaries based solely on misorientation is insufficient. The full five parameter GBCD will be calculated and compared for the reference and thermomechanically processed nickel samples. Of particular interest will be the orientation of the grain boundary planes of the $\Sigma 3$ boundaries that are introduced with processing.

Previous research has shown that $\Sigma 3^n$ grain boundaries (other than coherent $\Sigma 3$ boundaries) result geometrically from interactions at triple junctions [81]. Thus, it is expected that grain boundary network connectivity is also an important factor in determining the GBCD and properties. To assess changes in the connectivity, triple junctions will be classified into groups based on the types of grain boundaries that meet to form the junction.

The hypothesis of this work is that both grain boundary energy effects and configurational constraints will influence the evolution of the GBCD from reference state to the GBE state. Higher energy boundaries will be replaced by lower energy grain boundaries on average, but energetic and crystallographic constraints will likely not permit all new $\Sigma 3$ grain boundaries to be coherent twins. Measurement of relative grain boundary energies, GBCDs, and triple junction composition will determine how the balance between grain boundary energy and configurational constraints influences the GBCD with iterative thermomechanical processing.

6.2 Results

6.2.1 Coincident Site Lattice-Based Analysis of Iterative Thermomechanical Processing

Commercial grain boundary engineering of nickel created obvious differences in the microstructure, as seen in Fig. 6.1. Instead of equiaxed grains with parallel interior twin boundaries as seen in the reference sample (a), the grain boundary engineered microstructure consists of a much more disjointed network of boundaries (b). Boundaries that are not Σ3 misorientation are marked in black.
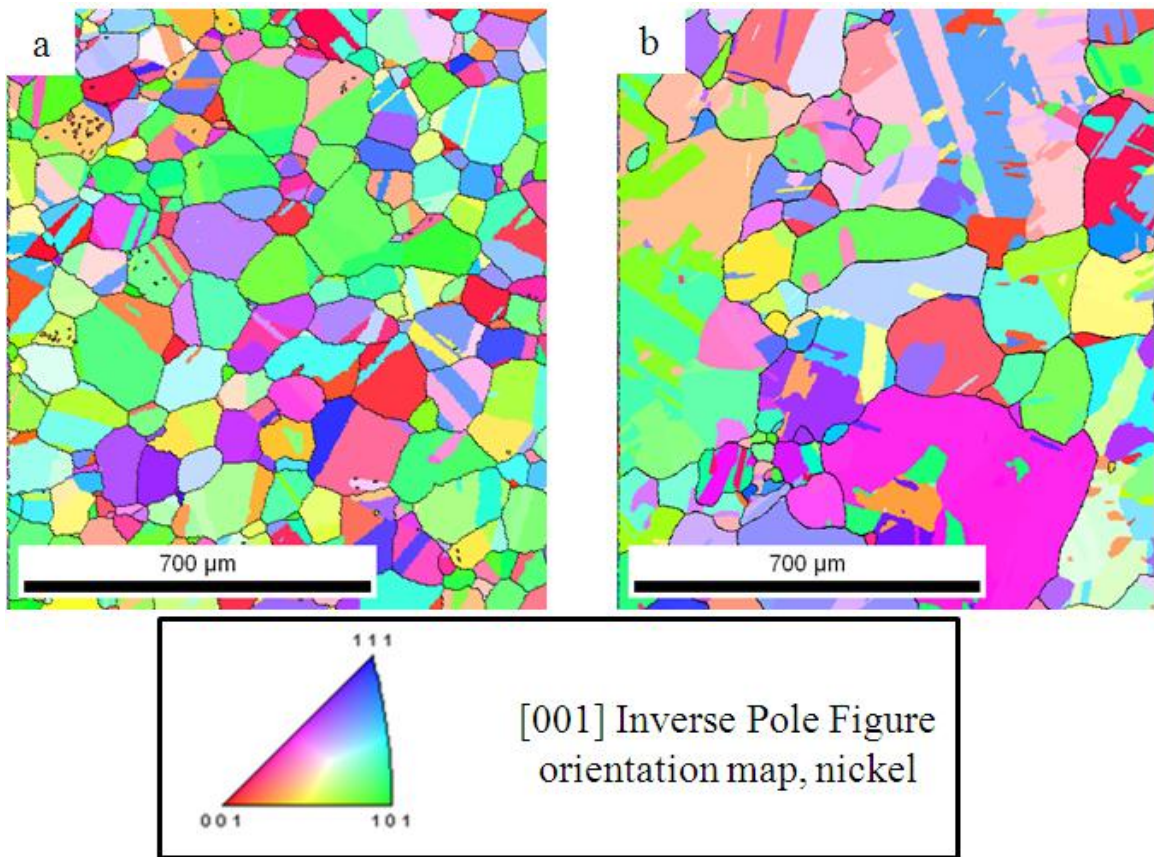
Figure 6.1 Representative [001] inverse pole figure orientation maps for Integran reference (a) and Integran GBE (b) nickel. Grain orientations with respect to sample coordinates are plotted according to the standard stereographic triangle color scale. Grain boundaries that do not have a Σ3 misorientation are colored black.

In commercial grain boundary engineering, control of the final grain size is important. In fact, grain growth is typically avoided so that grain boundary engineered microstructures have a similar average grain diameter as the initial microstructure. Minimal deformation and annealing is employed to allow for boundary reconfiguration instead of grain growth. For the high purity nickel analysis, the iterative thermomechanical processing was not optimized. As a result, grain growth did occur during the five strain-recrystallization cycles employed. Fig. 6.2 shows inverse pole figure maps that are representative of the microstructures analyzed in this study. Recent work has been completed to quantify the microstructural differences for the commercially available material [82]. Conventional analysis of GBE materials requires the comparison of fraction of "special" boundaries (FSB) based on the CSL framework – or, the misorientation dependent distribution $\lambda(\Delta g)$. In previous research, boundaries with $\Sigma <= 29$ are considered special. However, in this work, noticeable changes in the distributions were only observed for $\Sigma 3^n$ boundaries, where n is 1, 2, or 3.
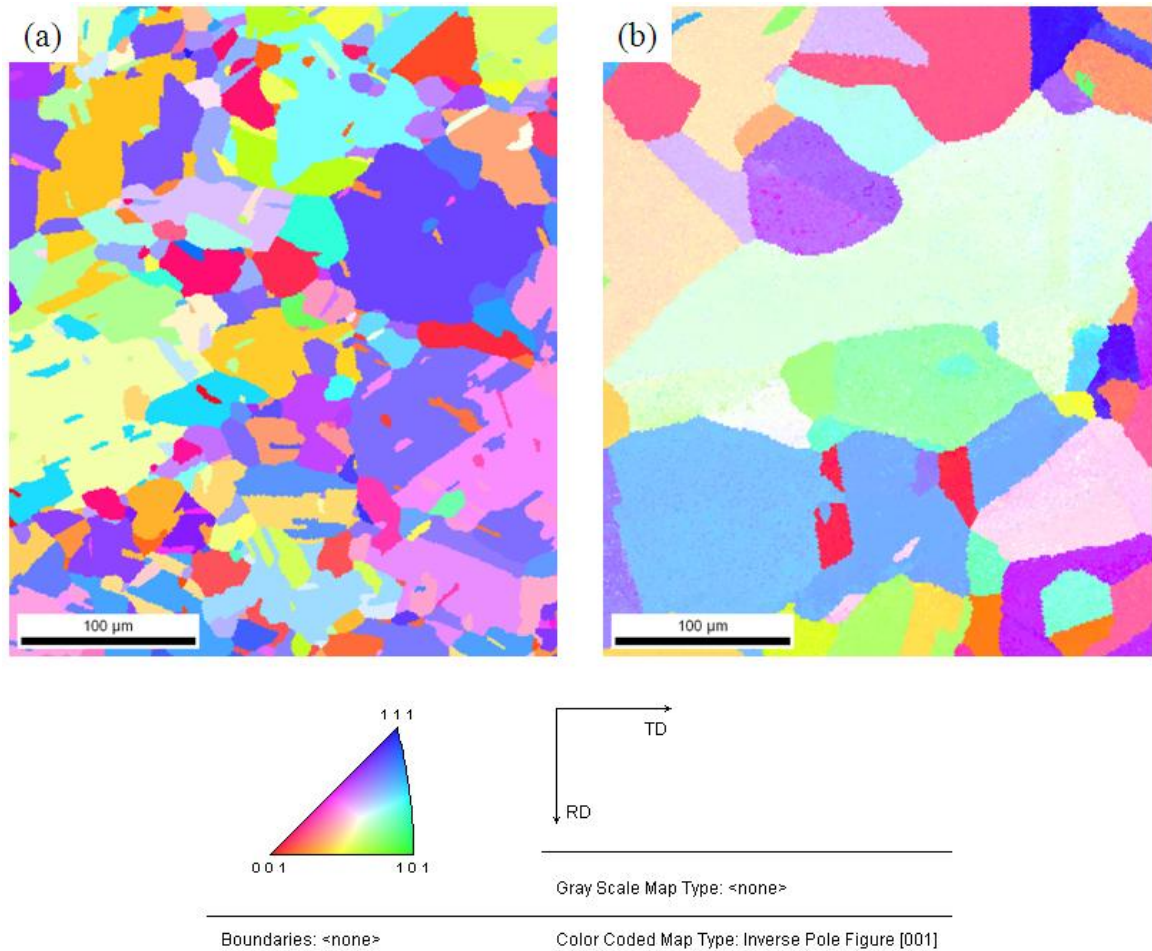
Figure 6.2 Representative inverse pole figure orientation maps for the high purity nickel reference (a) and the iterative thermomechanically processed (b) samples. Grain orientations with respect to the sample normal are colored according to the scale. The average grain size increased from 12.7 μm to 40.57 μm.

As described in Chapter 3, it is the $\Sigma 3^n$ that are expected to have a greatest influence on properties. As a result, the reference and GBE samples will first be quantified based on populations of these $\Sigma 3^n$ boundaries. Plots in Fig. 6.3 compare both the length and number fractions of $\Sigma 3$, $\Sigma 9$, and $\Sigma 27$, (within Brandon tolerance [83]) boundaries before and after GBE processing. Results show an increase in both the length and number fraction for $\Sigma 3^n$ boundaries. It appears that for grain boundary engineering for Ni, an increase in population of $\Sigma 3^n$ boundaries is due to "generation" more than

lengthening of boundaries. That is to say, new grain boundaries are being created and it is not just the relative lengthening of existing boundaries that is causing the increase in population. This idea will be explored in Chapter 6, Section 2.3. If the relative increase is calculated for each type of $\Sigma 3^n$ boundary (Fig. 6.3c), where relative increase is defined as $(\text{fraction}_{GBE} - \text{fraction}_{reference})/\text{fraction}_{reference}$, it is seen that $\Sigma 9$ boundaries are increasing in length more than number while $\Sigma 3$ and $\Sigma 27$ boundaries are increasing more in number. Although initial $\Sigma 3^n$ populations are higher for the initial high purity nickel than for the commercially available reference nickel (see Fig. 6.4), fractional length and number $\Sigma 3^n$ populations after five strain-recrystallization cycles are very similar to the $\Sigma 3^n$ populations found in the Integran ^{TM} GBE nickel.
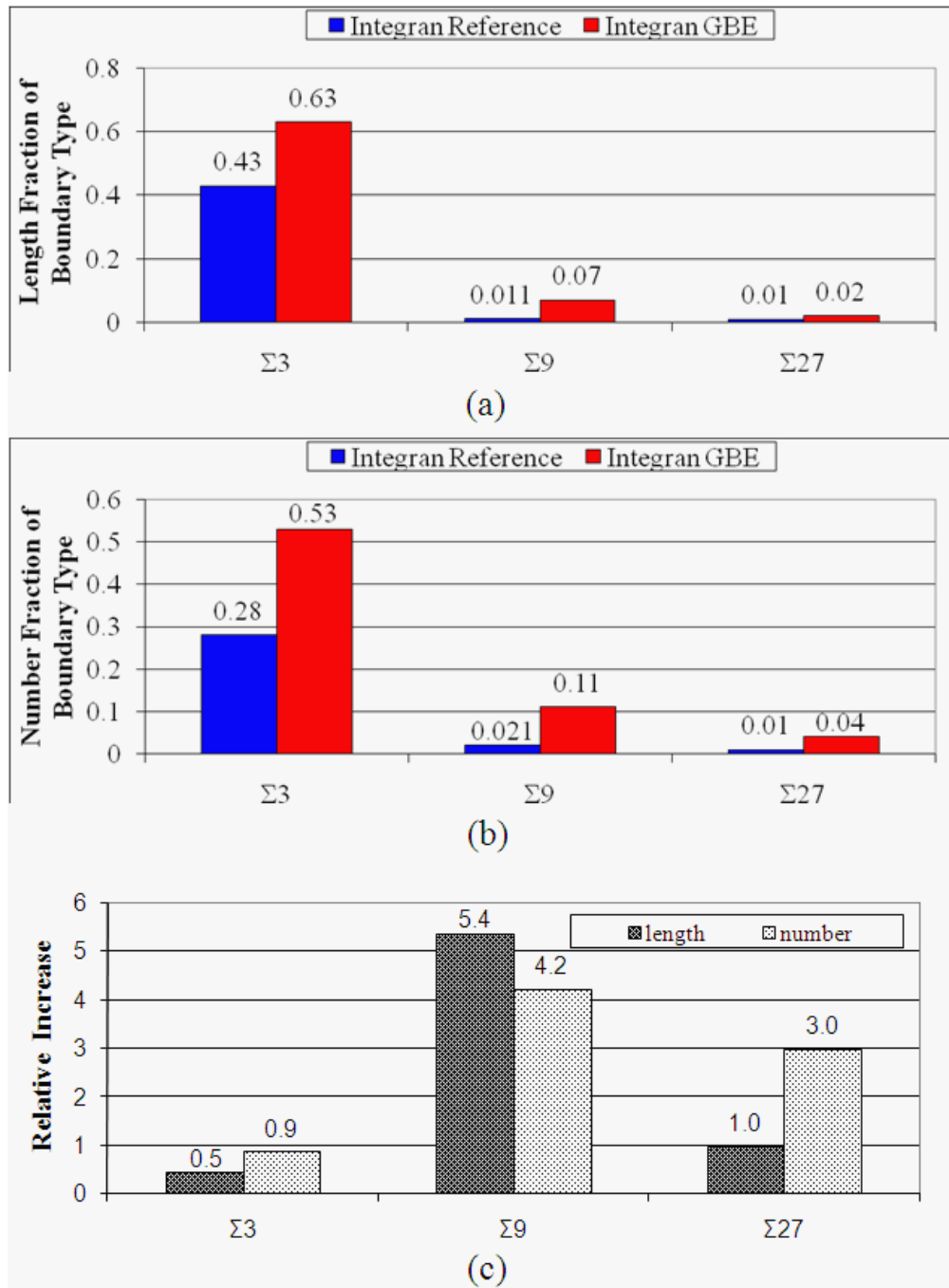
Figure 6.3 Plots of the length fractions (a) and number fractions (b) of Σ3, Σ9, and Σ27 boundaries for Integran reference and GBE nickel. An increase in both the length fraction and number fraction of Σ3, Σ9, and Σ27 boundaries is observed with grain boundary engineering. (c) Plots showing the relative increase, defined as (fraction$_{GBE}$ − fraction$_{reference}$)/fraction$_{reference}$, of the length and number fraction of Σ3, Σ9, and Σ27 boundaries with GBE processing. Σ3 and Σ27 boundaries increase more in number, while Σ9 boundaries increase more in length.
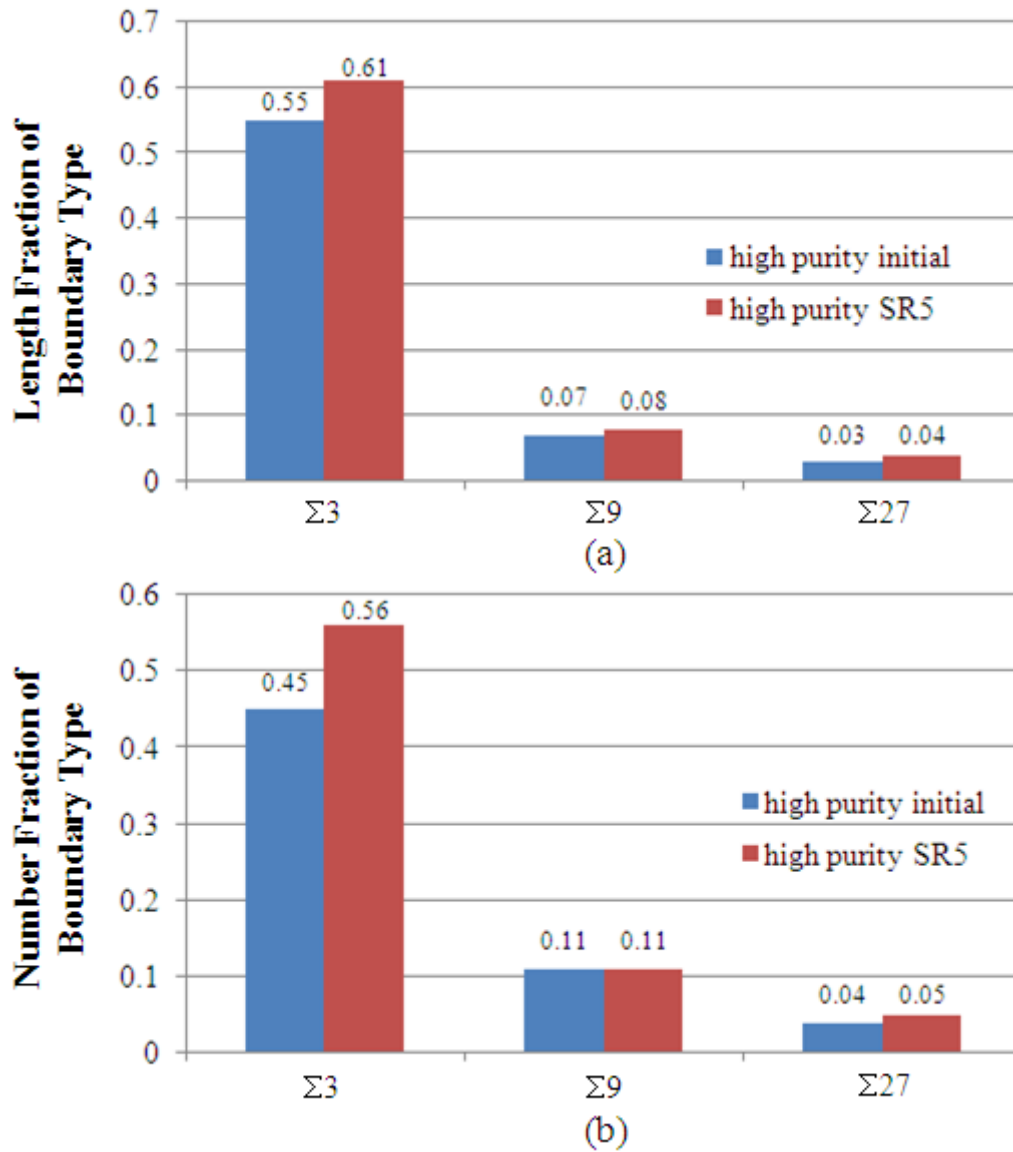
Figure 6.4 Plots of the length fractions (a) and number fractions (b) of $\Sigma3$, $\Sigma9$, and $\Sigma27$ boundaries for high purity initial and SR5 nickel. A slight increase is observed for $\Sigma3^n$ boundaries. $\Sigma3^n$ in the SR5 sample are very similar to $\Sigma3^n$ populations found in commercial GBE nickel.

To fully understand the evolution of the GBCD with GBE, it is necessary to consider the orientation of grain boundary planes in the samples as well. For instance, coherent $\Sigma3$ boundaries are expected to have different properties and effects on the microstructure than incoherent $\Sigma3$ boundaries. For this analysis, the grain boundary

segments in each sample are classified in the following way. If the misorientation is within Brandon's criterion (8.7 °) of the ideal $\Sigma 3$ misorientation, and the surface trace of the boundary is within 10° of orientation of the coherent twin, it is classified as a coherent twin. The tolerance of 10° was selected because this is commensurate with the resolution with which the five parameter grain boundary distribution data is discretized. If the misorientation is within Brandon's criterion of the ideal $\Sigma 3$ misorientation, but the surface trace of the boundary is more than 10° from the orientation of the coherent twin, then a boundary is classified as an incoherent $\Sigma 3$. It should be noted that some of the incoherent $\Sigma 3$s have traces that are coincidentally within the 10° tolerance and will be incorrectly classified as coherent. This leads to a small overestimation of the coherent twin population and an underestimation of the incoherent $\Sigma 3$ population. Recognizing the small error, we will henceforth consider all those boundaries with traces less than 10° from the ideal trace to be coherent twins. If the boundary does not meet the Brandon criterion, it is considered a random boundary. We recognize that some of the boundaries that are placed in the random category could also be classified according to their special characteristics (for example, the $\Sigma 9$ and $\Sigma 27$ grain boundaries), but for the purposes of this analysis we differentiate only the $\Sigma 3$ boundaries. The grain boundary populations based on this classification scheme are shown in the Table 6.1. It is important to note that the total grain boundary L/A is very similar for both the reference and GBE Ni. Considering the L/A fraction, it is obvious that the increase in the overall population of $\Sigma 3$ boundaries resulting from GBE is due in large part to the increase of incoherent $\Sigma 3$ boundaries. Length/area of random boundaries is observed to decrease with GBE. Similar results were not calculated for the high purity nickel samples because the total

length/area of grain boundaries obviously does not stay the same with processing, making

interpretation difficult.

Table 6.1 Summary of Σ3 Boundary Statistics for Integran Reference and GBE Nickel

		N%	L, μm	L,%	$<L>$, μm	L/A, μm^{-1}
reference	total	100	21.7×10^5	100	25.2	3.40×10^{-2}
	random	73	12.5×10^5	58	20.0	1.95×10^{-2}
	Σ3	27	9.23×10^5	42	38.9	1.44×10^{-2}
	coherent Σ3	15	6.18×10^5	28	48.3	0.97×10^{-2}
	incoherent Σ3	12	3.04×10^5	14	27.8	0.47×10^{-2}
GBE	total	100	23.8×10^5	100	20.6	3.53×10^{-2}
	random	47	8.79×10^5	37	16.3	1.31×10^{-2}
	Σ3	53	15.0×10^5	63	24.5	2.22×10^{-2}
	coherent Σ3	20	8.2×10^5	34	35.0	1.21×10^{-2}
	incoherent Σ3	33	6.77×10^5	28	18.0	1.01×10^{-2}

The data in Fig. 6.5 illustrate how the orientations of the Σ3 grain boundaries are

distributed for the commercially available and high purity nickel. In each case, the

orientation of the observed grain boundary trace was compared to the orientation of a

trace that would be expected if the boundary were an ideal coherent twin. Those

boundaries with small deviation angles (less than 10°) are likely to be coherent and those

with large angles are definitely incoherent. The data show that the fractional population

of Σ3 grain boundaries increases by roughly the same amount at all deviation angles. As a

result, the number and length fractions of incoherent Σ3s increase more than for coherent

twins. Note that for the commercially available nickel, the number fraction increase of Σ3

grain boundaries is larger than the length fraction increase because, as shown in Table

6.1, the Σ3 grain boundaries resulting from the GBE process have, on average, less area

than the pre-existing Σ3 grain boundaries. Similar to the commercially available nickel, there is an appreciable increase for the number fraction of Σ3 that are incoherent, peaking approximately 15 °- 30 ° from coherency. It should be pointed out that number fraction statistics may be skewed by grain boundary reconstruction processing. Long, straight coherent twins should always be represented by one boundary segment. If other boundaries exhibit enough curvature, though, they may be represented by more than one boundary segment. While this is likely to lead to a small overestimation of the number fractions, it will not pose a problem when calculating the length fractions. Based on the length fraction analysis, it is apparent that while there is an increase in coherent twins with processing, the majority of the increase in Σ3 population is due to an increase in incoherent Σ3 boundaries.
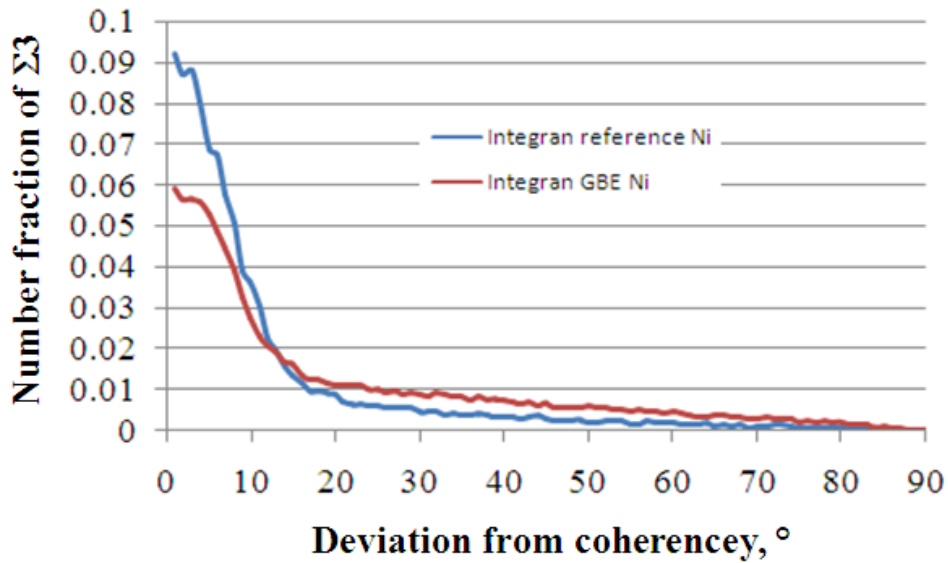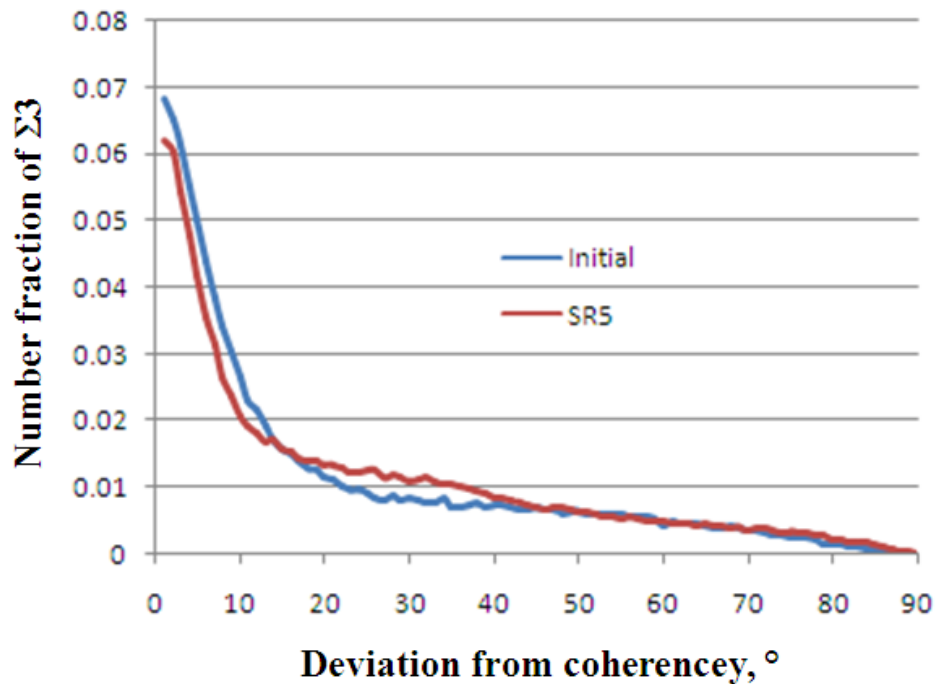
Figure 6.5 The fraction of Σ3 grain boundaries as a function of the angle (°) between the measured grain boundary trace and the trace expected for an ideal coherent twin for the commercially available (a) and for the high purity (b) nickel samples. An increase in coherent Σ3 grain boundaries is observed, but they make up a smaller faction of the total Σ3 grain boundary population. Incoherent Σ3 grain boundaries make up a greater fraction of the population with grain boundary engineering. The results are qualitatively similar.

6.2.2 GBPD Changes with Iterative Thermomechanical Processing

No net increase of {111} boundary planes is observed in the misorientation-independent population of grain boundary planes ($\lambda(\mathbf{n})$) with iterative thermomechanical processing for the commercially available nickel (Fig. 6.6). This is consistent with the results from Chapter 6, Section 2.1 considering misorientation only. Some coherent $\Sigma 3$ grain boundaries are being created, but they make up a smaller fraction of the total population after GBE processing. Thus, there is no net increase in {111} type grain boundary planes.

(a)   (b)
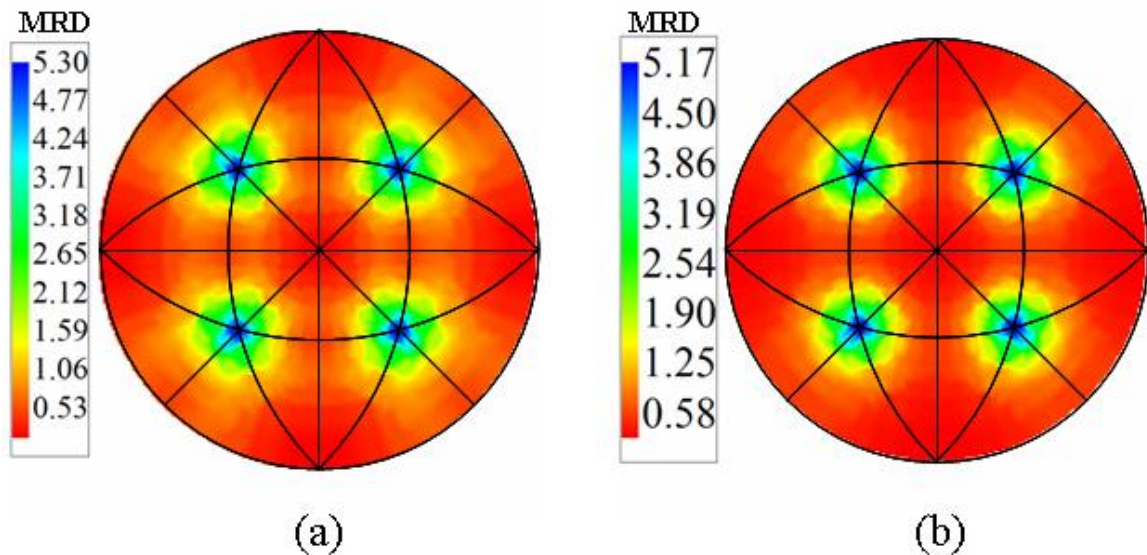
Figure 6.6 GBPD for Integran reference (a) and GBE (b) nickel, plotted on stereographic projections in units of MRD. No net increase of boundaries terminated by {111} planes is observed.

As with the commercial nickel, we will begin by analyzing the GBCD of the high purity nickel samples by considering the grain boundary plane distribution at a 10 ° binning resolution. As expected, both distributions peak for {111} type boundary planes. This is primarily due to twins in the samples, and is typical of fcc metals with low to moderate stacking fault energies. In this case, while the distributions are similar, there is

a slight increase in boundaries terminated by {111} planes with processing (Fig. 6.7).
The increase is 11 % and is presumably a measureable difference based on the 10 %
tolerance established earlier in this work.
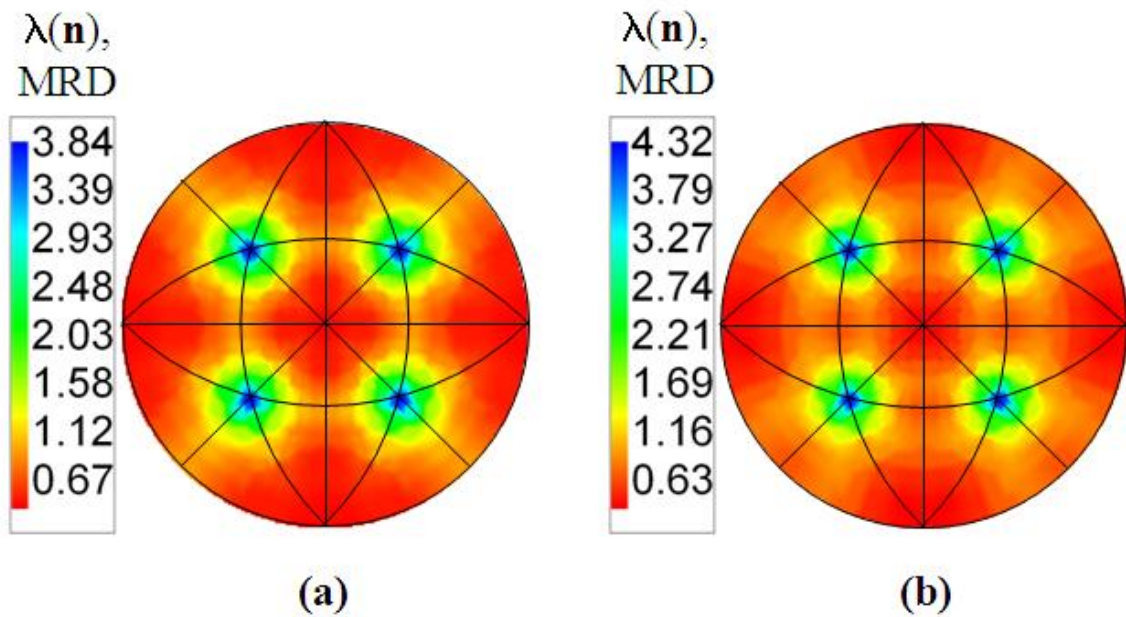
Figure 6.7 GBPD for the high purity reference (a) and iterative thermomechanically processed (b) nickel, plotted on stereographic projections in units of MRD. An 11 % increase of boundaries terminated by {111} planes is observed.

6.2.3 Binning Resolution Effects on the Determination of the GBPD

It is known that the binning resolution of the five parameter grain boundary
character space will determine the number of distinguishable grain boundaries. Binning
resolution is also expected to have an effect on the observed or reconstructed GBCD. At
any resolution, a given bin will include a range of independent grain boundary-type
observations that are all assigned to a single boundary type. This could lead to a
population value for a given boundary type which is either artificially high or low,

depending on width of a feature in the distribution (for example, a maximum), the size of the bins, and the exact placement of the bins with respect to the feature. If the width of the distribution is narrower than the binning resolution, the observed peak intensity will increase in proportion to the number of bins used. For increasing resolution, as the bins become similar in size or smaller than the width of the peak in question, the observed intensity will remain constant with bin size. A schematic diagram illustrating idealized limiting cases of this effect is shown in Fig. 6.8. In Fig 6.8a, a fixed number of observations (100) are placed in one bin at a fixed resolution. The corresponding populations of each bin in MRD are plotted above the bins. In Fig. 6.8, the resolution is doubled and the fixed number of observations still falls within one bin. This is analogous to the peak width being narrower than the binning resolution. As expected, the observed population for this bin in MRD increases. For this example, the observed population doubles. Fig. 6.8c shows an example of the peak width being larger than the binning resolution. In this case, as the resolution is doubled, the observations are now divided into two neighboring bins. The result is an observed population that does not differ from that found with the original binning.
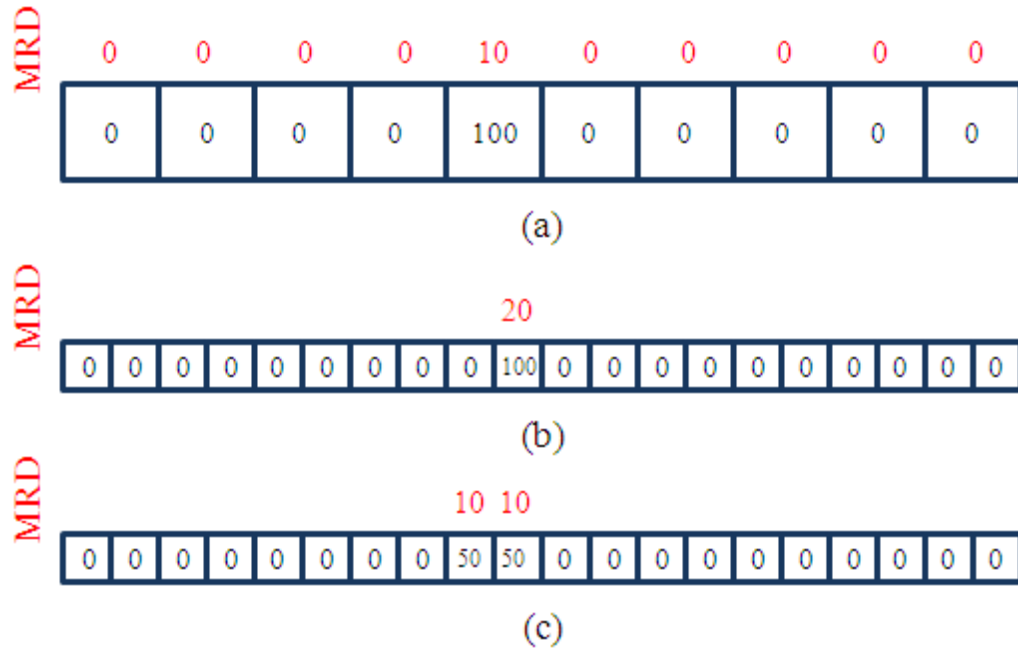
Figure 6.8 Diagram showing effects of binning resolution on observed populations. 100 observations are placed in one bin in (a), leading to an observed population of 10 MRD for that "boundary type." Upon doubling the resolution, if the width of the observations peak is less than the bin size, the observations will still fall within one bin and observed population will double (b). If, however, the width of the observations is such that the observations are divided between two bins, the observed population will be the same as that as found for the initial binning. Further increasing the binning resolution will lead to a decrease in the observed populations.

It is important to quantify the impact of this effect on the reconstructed GBCD. The misorientation-independent GBPD is again a convenient measure to study first. The GBPD was calculated for an increasing number of grain boundary segments for the high purity initial nickel sample at 10 °, 8.18 °, and 5 ° resolution. These resolutions represent the result of dividing $\pi/2$ (90 °) into 9, 11, and 18 bins, respectively. The maxima and minima are plotted in Fig. 6.8 for each resolution with respect to the number of segments used to calculate the GBPD. It is observed that the calculated GBPDs remain consistent at both 10 ° and 8.18 ° when more than approximately 20,000 reconstructed grain boundary segments are used. This is consistent with the experimental results for $SrTiO_3$

presented in Chapter 4, Section 3.1. While it was expected that this guideline would hold true for 10 ° binning of the GBPD for nickel, it is interesting to note that it also appears to hold true when 8.18 ° resolution is chosen as well. Even though both of these types of GBPD distributions remain consistent after approximately the same number of segments used in the calculation, the maxima of the GBPDs calculated at 10 ° are consistently lower than the maxima of the GBPDs calculated at 8.18 °.

The results also show that when the GBPD is measured with 5 ° bins, more observations are needed. The maximum of the GBPD does not level off after 20,000 segments are used. It is not until at least 50,000 segments are used that the maximum ceases to vary by less than 10 %. The fact that the maxima are relatively constant for 5 ° and 8.18 ° indicates that resolution of the bins has exceeded the resolution of the observations.
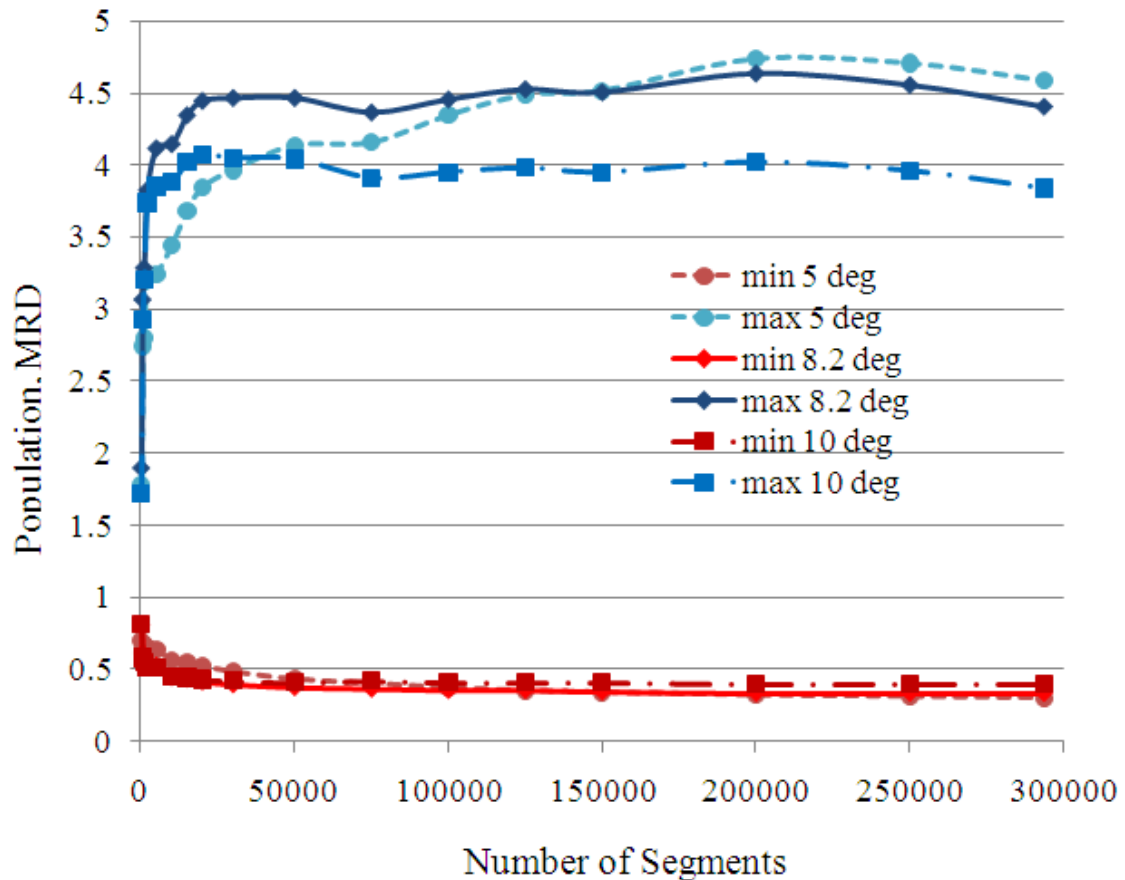
Figure 6.9 Maxima and minima of the GBPD with respect to the number of segments used in the stereological calculation for the high purity initial nickel sample at 10 °, 8.18 °, and 5 °. The maxima calculated at 10 ° and 8.18 ° resolution remain relatively constant when greater than approximately 20,000 reconstructed grain boundary segments are used in the stereological reconstruction of the GBPD. More than 50,000 reconstructed boundary segments are required for the consistent stereological reconstruction of the GBPD at 5 ° resolution.

In Fig. 6.10, the GBPD is plotted for the high purity nickel "initial" sample at 10 °, 8.18 °, and 5 ° resolution. Analysis similar to that reported in Chapter 4, Section 2.1 was performed on three 100,000 segment subsets of the full initial high purity nickel dataset. The GBPD was calculated for each subset to estimate the amount of variation within the dataset to quantify measureable differences. For both 10 ° and 8.18 ° resolution, the maxima of subset GBPDs varied by less than 8 %. From this, we will

assume that the 10 % threshold for interpretable differences as established in Chapter 3 still holds at these resolutions, the effect of averaging with coarse binning is observable when comparing the 10 ° case to the 8.18 ° case. The population of boundaries terminated by {111} planes is underestimated with 10 ° binning and differs from the 8.18 ° case by approximately 13 %. It appears there is a slight increase in the anisotropy of the distribution when increasing the resolution to 5 °; however, this increase is only 4%. This is not to be a measureable difference. It is also unlikely that the in plane grain boundary geometry was measured with greater than 5 ° accuracy for this dataset.
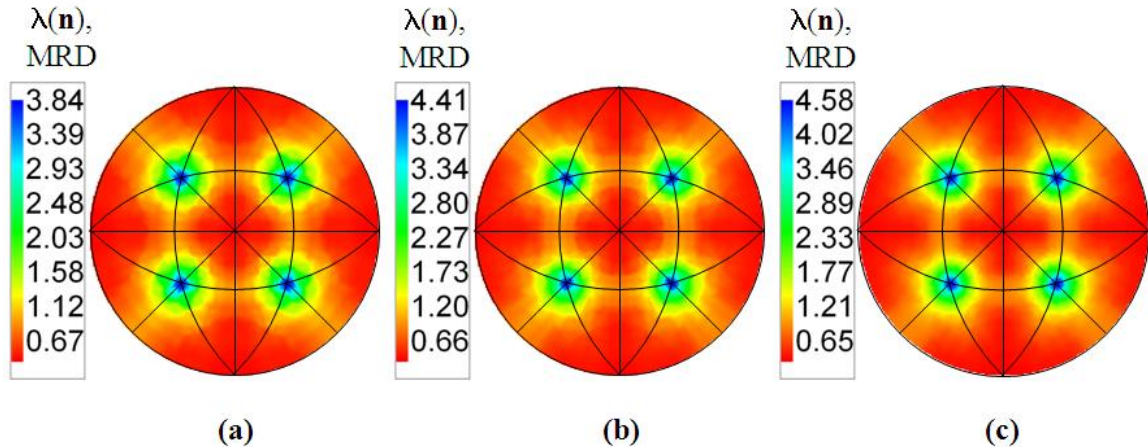
Figure 6.10 The GBPD for the reference high purity nickel sample reconstructed with 10 ° (a), 8.18 ° (b), and 5 ° (c) resolution. Sufficient observations have been made for reliable GBPD reconstruction at 10 °, 8.18 °, and 5° resolution. All distributions are qualitatively similar with peaks in the distributions for {111} boundary termination planes. A 15 % difference between the distribution calculated with 10 ° resolution and the distribution calculated with 8.18 ° resolution is observed. The 4 % difference between the 8.18 ° and the 5 ° resolution is insignificant.

With an increase in resolution from 10 ° to 8.18 °, there is an increase of a factor of 2.73 in the number of distinguishable boundaries. A simple approximation can be made that assumes that the number of observations required for reliable determination of the GBPD should also increase by this same factor. Following this assumption, sufficient

observations have been made for 8.18 ° resolution, but not for 5 ° resolution. This again

may lead to an underestimation of the anisotropy of the distribution at this resolution.

The grain boundary geometry was presumably measured with a much greater

accuracy for the SR5 sample. As a reminder, a step size/average grain size diameter ratio

of 1:27 was used for this dataset. Calculated results for the GBPD are plotted for 10 °,

8.18 °, and 5 ° resolution in Fig. 6.11. As for the "initial" sample, intensities of peaks are

observed to increase upon increasing the resolution to 8.18 °. Population peaks are being

underestimated at 10 ° resolution. In this case, the difference is approximately 16 % and

is experimentally distinguishable. Based on the subset analysis results, the difference

between 8.18 ° and 5 ° is not to be experimentally distinguishable.

(a)   (b)   (c)
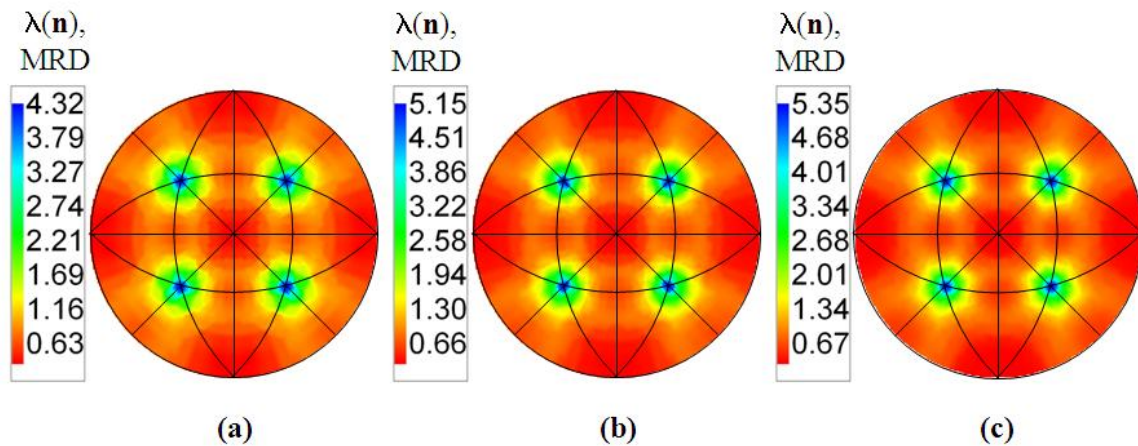
Figure 6.11 The GBPD for the SR5 high purity nickel sample reconstructed with 10 ° (a), 8.18 ° (b), and 5 ° (c) resolution. All distributions are qualitatively similar with peaks in the distributions for {111} boundary termination planes. A 19 % difference between the distribution calculated with 10 ° resolution and the distribution calculated with 8.18 ° resolution is observed. The 4 % difference between the 8.18 ° and the 5 ° resolution is insignificant.

6.2.4 Five Parameter GBCD Analysis

It has already been shown that materials can have similar misorientation-independent grain boundary plane distributions but have different grain boundary character distributions. To fully characterize the microstructural differences between the two sample states, we must consider all five grain boundary parameters.

We begin by considering the coherent twin population in the two samples. For the commercially available material, these distributions are plotted in Fig. 6.12. A marginal increase in coherent Σ3 boundaries (those terminated by (111) planes) is evident. The peak in the distribution for this boundary type increases from approximately 1200 MRD to approximately 1430 MRD.
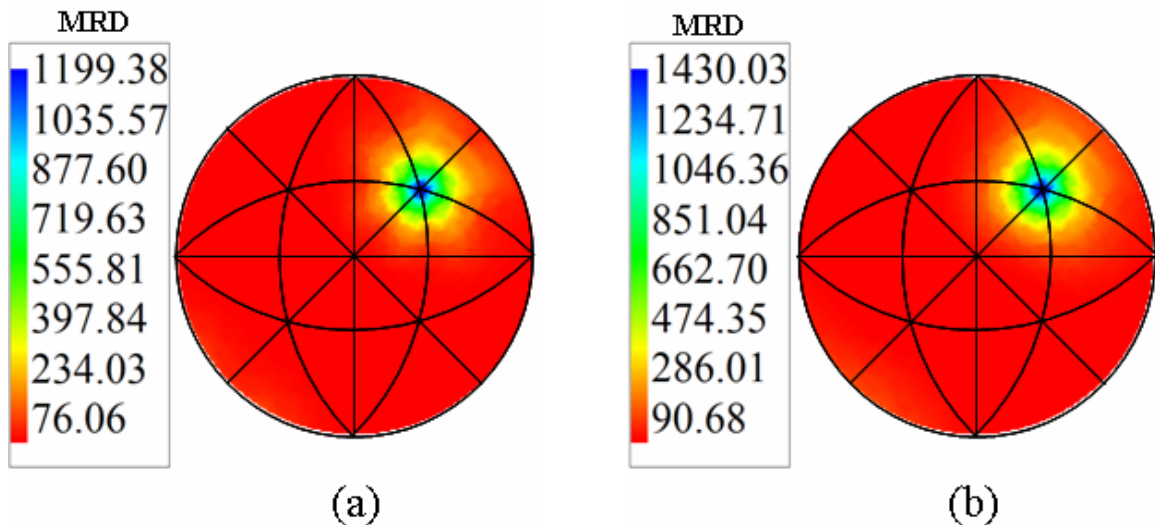
Figure 6.12 The distribution of grain boundary planes with the Σ3 (60 ° rotation around [111] misorientation axis) misorientation for Integran reference (a) and GBE (b) nickel plotted on stereographic projections in units of MRD. A high population of boundaries terminated by (111) planes is observed in each case. This is the coherent twin. The increase after GBE processing is minimal.

Because of the strong peak at the coherent twin position, it is difficult to visualize

any of the features of the distribution of incoherent boundaries. For this reason, the

distribution of grain boundary planes with the $\Sigma 3$ (60 ° rotation around [111]

misorientation axis) misorientation is plotted in along the [$\bar{1}$10] zone in Fig. 6.13 with the

coherent twins excluded.
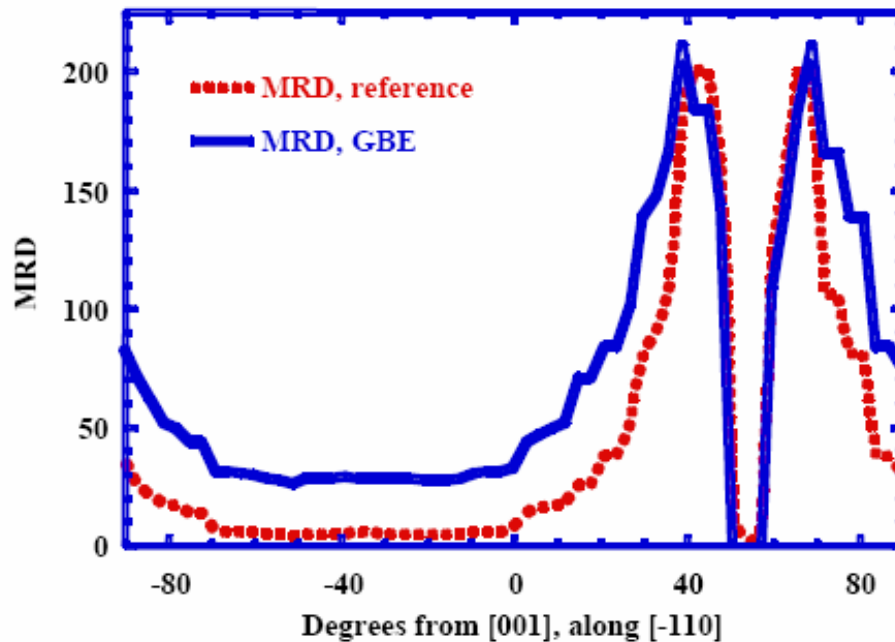
Figure 6.13 Population of grain boundary planes along the [–110] for both the reference
and GBE nickel samples, plotted in units of MRD with respect to the angular distance
from [001]. For this plot, coherent twins were removed, creating a "crater" in the
distribution near the orientation of {111} planes. There is an increase in population of
grain boundary planes along the entire [–111] zone with GBE. The width of the ring
around the "crater" also increases with GBE.

Because of the exclusion of the coherent twins, the distribution appears crater-like, with a

minimum at the (111) position and a maximum "ring" 10° away that reaches more than

200 times random. The shape of the distributions for the reference and GBE materials

are similar, except for the fact that in the GBE sample, the distribution extends further

away from the ideal (111) position. Along the [-1 10] zone, the grain boundary plane

population is greater than or equal to 30 MRD at all orientations. In contrast to the reference sample population, a relatively high population is maintained for all orientations in the [-1 10] zone of the GBE sample.

The increase in boundaries terminated by {111} planes with iterative thermomechanical processing in the high purity nickel is a direct result of an increase in the coherent twin population. The distribution of boundary planes with a 60 ° misorientation about [111] (λ(n|60 °/[111])) is plotted on stereographic projections for the initial and SR5 samples in Fig. 6.14. As expected, there is an observable increase in coherent twin boundaries with processing. The population of boundaries with the $\Sigma 3$ misorientation that are bounded by (111) planes increases from approximately 1641 MRD for the initial state to 1908 MRD for the engineered state, a 14 % increase. This increase is very similar to the increase in population observed at the same fixed misorientation for the commercial nickel. It is important to note that a portion of the observed increase in coherent twins might be caused by the incorrect inclusion of incoherent twins because of the 10 ° bin-resolution. This effect will be explored in the next section.

160

MRD

1640.88
1424.76
1208.65
992.53
776.41
560.30
344.18
128.07

MRD

1907.91
1656.62
1405.34
1154.05
902.77
651.48
400.20
148.91

(a) (b)
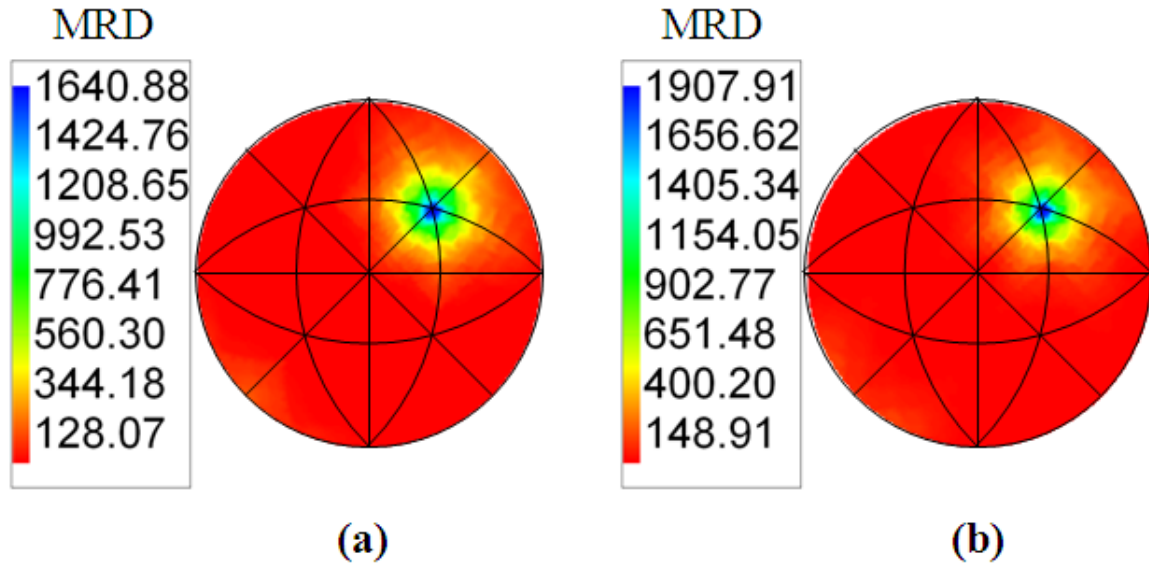
Figure 6.14 The distribution of grain boundary planes with the Σ3 (60 ° rotation around [111] misorientation axis) misorientation for the high purity reference (a) and GBE (b) nickel plotted on stereographic projections in units of MRD. A high population of boundaries terminated by {111} planes is observed in each case. This is the coherent twin. The increase in boundaries of this type after iterative thermomechanical processing is approximately 16 %.

6.2.5 Binning Resolution Effects on the Determination of the Five Parameter GBCD

The observed grain boundary character distribution depends strongly upon the

binning of the five independent macroscopic parameters used to define a grain boundary.

If there are two peaks in the distribution with an angular spacing that is smaller than the

bin size, it will obviously not be possible to differentiate them. As an example, it is not

possible to differentiate between Σ9 and Σ27a boundaries at the previously used 10 °

resolution, as the disorientation between these two misorientations is 7.3 ° and they fall in

the same bin. Another result of binning is a likely "smoothing" of the observed GBCD,

as coarser bins necessarily include average grain boundary types that are different but

indistinguishable because of the resolution of the binning. The locations of the edges of

the bins in five parameter space are also affected by the resolution. Depending on the resolution chosen, some specific boundary types of interest may fall on the boundary between two bins. For these reasons, it is desirable to quantify differences in calculated GBCDs for increasing binning resolution.

One cannot necessarily increase this resolution with disregard to all other factors. First, increasing the resolution of the binning of the five parameters that define the GBCD greatly increases the number of distinguishable boundaries. In fact, the number of distinguishable boundaries is inversely correlated to the resolution to the fifth power. If the binning resolution is doubled, there are 32 times more distinguishable boundaries. As a consequence, significantly more observations are required for the stereological procedure to maintain statistical significance. As important, if not more so, is the requirement that the five parameters are being measured with accuracy comparable to the binning. Here, the major limitation is the accuracy of the determination of the in-plane grain boundary trace geometry.

Significantly larger datasets were recorded for high purity initial and SR5 nickel samples than for the commercially available nickel to aid in distinguishing $\Sigma 9$ and $\Sigma 27a$ grain boundaries when considering the five parameter GBCD. When using 10 ° binning of the five parameter space, these boundary types overlap. The grain boundary plane distributions calculated with binning resolutions of 10 ° and 8.18 ° for fixed misorientations of 38.9 ° / [110] ($\Sigma 9$) and 31.6 ° / [110] ($\Sigma 27a$) are plotted for the high purity initial nickel sample in Fig. 6.15. As expected, the plots calculated with 10 ° resolution (a, b) are identical. This is because at 10 ° resolution, both boundary types are grouped into the same bin because their disorientation is less than 10 °. When the $\Sigma 9$

populations calculated at 10 ° and 8.18 ° resolution are compared (a,c), it is observed that the population of Σ 9 boundaries is being underestimated in the 10 ° plot. This is because the less populous $\Sigma27a$ boundaries are being averaged along with the $\Sigma9$ boundaries at 10 ° resolution. Conversely, it is observed that the $\Sigma27a$ population is overestimated in the 10 ° resolution plot as Σ 9 boundaries are being included as well. Similar results are observable for the high purity SR5 nickel sample, as seen in Fig. 6.16. Population increases with iterative thermomechanical processing for $\Sigma9$ and $\Sigma27a$ boundaries are observed at both resolutions, as expected.
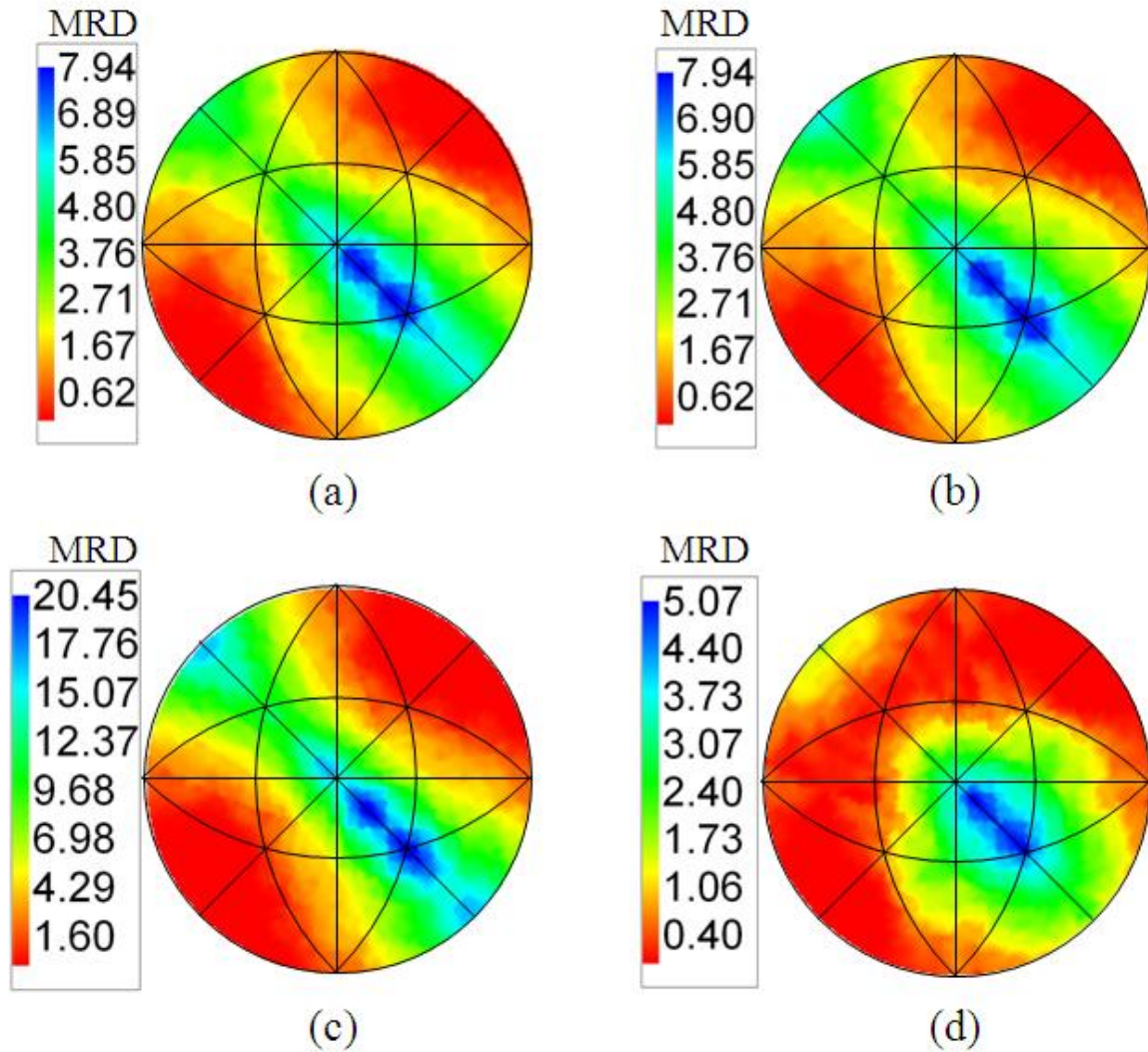
Figure 6.15 The grain boundary plane distributions calculated with binning resolutions of 10 ° (a,b) and 8.18 ° (c,d) for fixed misorientations of 38.9 ° / [110] (Σ9) (a,c) and 31.6 ° / [110] (Σ27a) (b,d) are plotted for the high purity initial nickel sample. Coarser binning leads to an underestimation of the Σ9 population and an overestimation of the Σ27a population at 10 ° resolution.
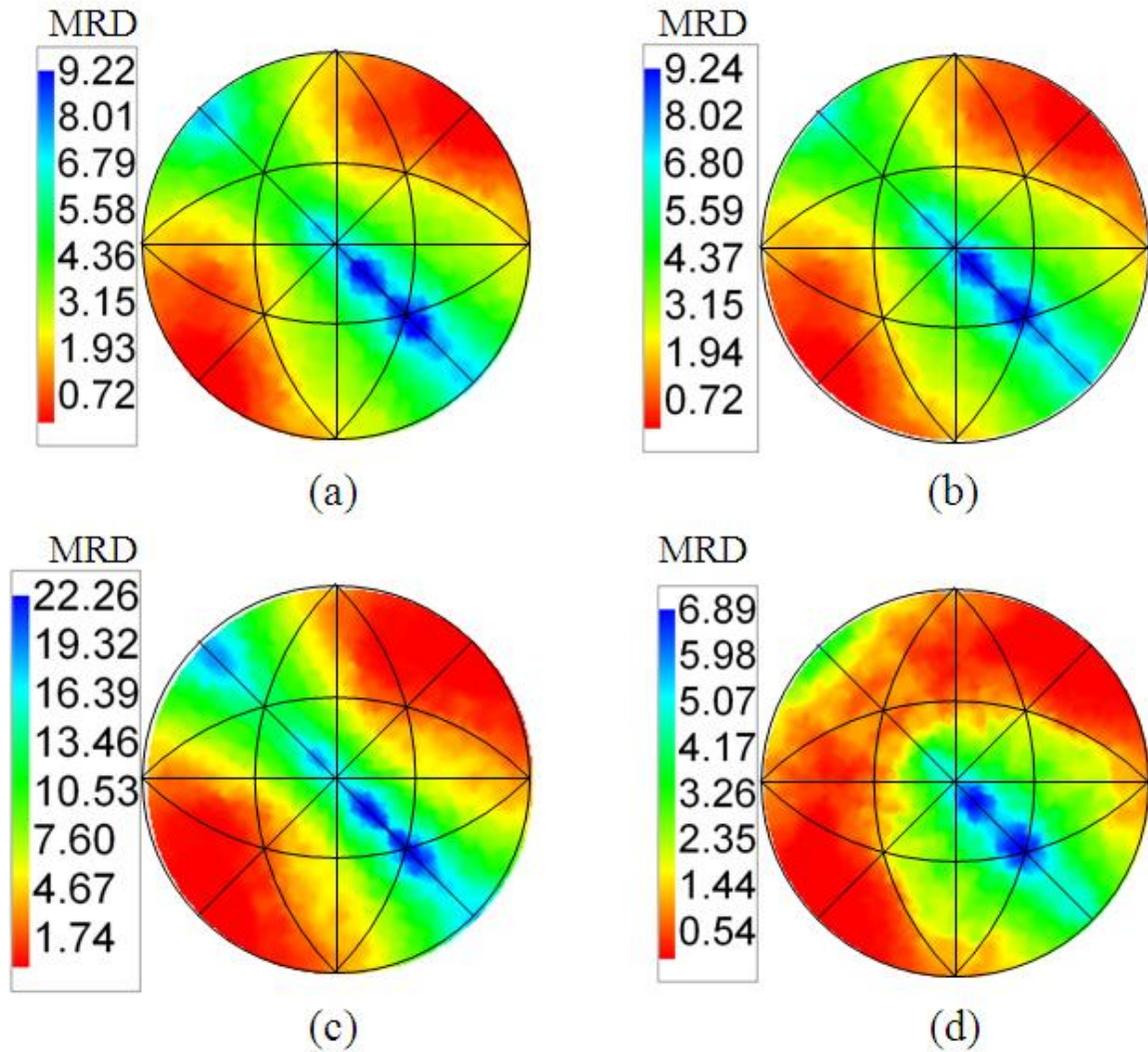
Figure 6.16 The grain boundary plane distributions calculated with binning resolutions of 10 ° (a,b) and 8.18 ° (c,d) for fixed misorientations of 38.9 ° / [110] (Σ9) (a,c) and 31.6 ° / [110] (Σ27a) (b,d) are plotted for the high purity SR5 nickel sample. Binning effect results are consistent with those observed for the high purity initial nickel sample.

Higher resolution binning of the space also allows for an understanding of the

effect of underestimation of peak maxima caused by bin averaging at lower resolutions.

This effect will be analyzed for coherent twin populations in both the high purity initial

and SR5 samples. Grain boundary plane distributions for a fixed misorientation of 60 ° /

[111] (Σ3 misorientation) calculated with 10 °, 8.18 °, and 5 ° resolution are plotted for

both high purity nickel samples in Fig. 6.17. It is not certain that in plane grain boundary

geometry has been captured at high enough resolution for reliable GBCD reconstruction

at 5 ° resolution, but it is hoped that because of the relative straightness and high

population of coherent twin boundaries that enough have been sampled with enough

accuracy for reliable population reconstruction at this resolution.
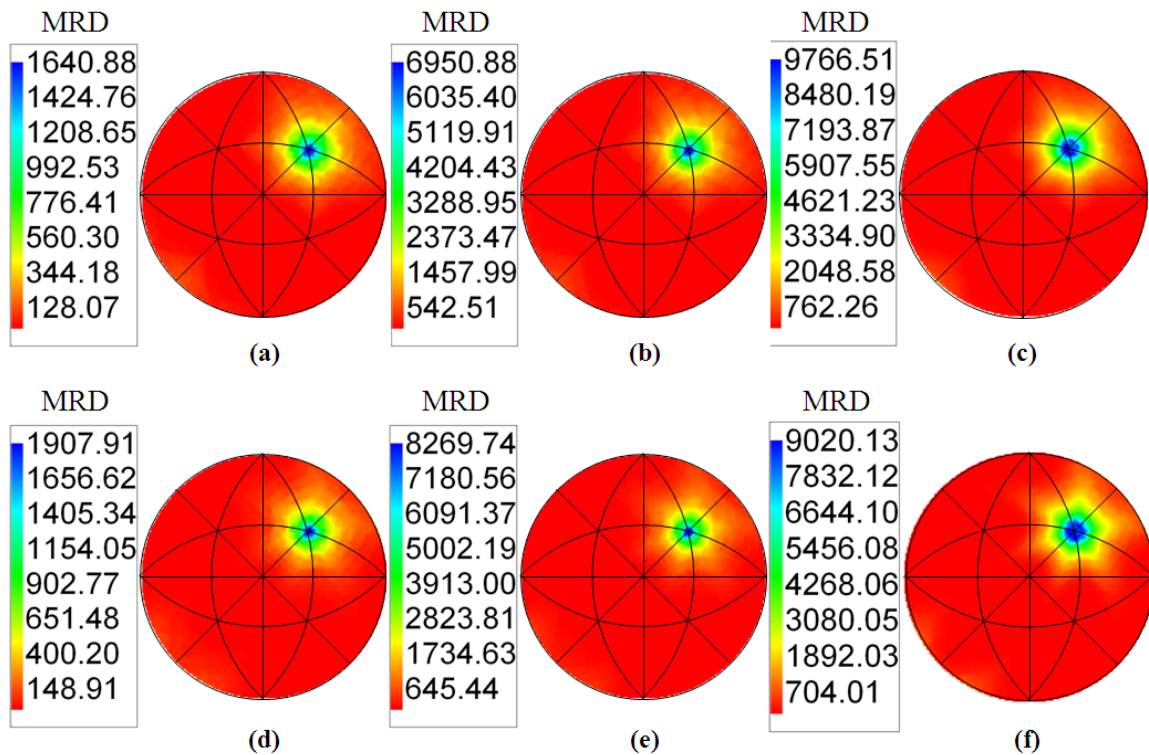
Figure 6.17 Grain boundary plane distributions for fixed misorientations of 60 ° / [111] for the high purity initial (a,b, and c) and SR5 (d,e, and f) nickel reconstructed at 10 ° (a,d), 8.18 ° (b,e), and 5 ° (c,f) resolution. As with $\Sigma9$ and $\Sigma27a$ boundaries, $\Sigma3$ populations are observed to increase with finer binning resolution. It is interesting to note that at 5 ° resolution, the SR5 sample appears to have a lower population of coherent twins than the initial sample.

As in the case of $\Sigma9$ and $\Sigma27a$ boundaries, $\Sigma3$ populations are observed to be

underestimated at coarser binning resolutions. For each sample, the observed coherent

twin population increases dramatically with a change in binning from 10 ° to 8.18 °

resolution. At 8.18 ° resolution, the SR5 sample still appears to have a higher coherent twin population. Upon tightening the binning resolution to 5 °, however, it appears that the initial sample has a higher population of coherent twins. This in an interesting observation that is consistent with the twin coherency analysis presented in Chapter 6, Section 2.1 and Section 2.4. The coherent twins in the initial sample, on average, are closer to the ideal twin configuration than the twins in the SR5 sample.

6.2.6 Grain Boundary Population and Relative Grain Boundary Energy Correlation

As with the $SrTiO_3$ and MgO work, it is necessary to determine relative grain boundary energies for nickel to observe the influence that grain boundary energy has on GBCD formation. For this work, relative grain boundary energies were determined for the high purity nickel using a previously established technique utilizing dual beam FIB serial sectioning coupled with orientation imaging [78]. For this experiment, a relatively fine grain size is required because the total possible volume of material for 3d analysis is limited by the FIB technique. A high purity nickel sample was created for this purpose by annealing a piece of the same high purity rod that the initial and SR5 samples came from at 325 °C for 15 minutes in flowing dry hydrogen.

As with the $SrTiO_3$ work, it is most straightforward to visually compare relative grain boundary energies with grain boundary populations for specific locations within the five parameter space. For this analysis, calculated grain boundary energy distributions can be compared to the grain boundary populations calculated at reference locations of interest in the five parameter space. Relative grain boundary energies are compared to

grain boundary populations measured for the high purity initial sample. In Fig. 6.18, the

calculated relative grain boundary energies are compared to grain boundary populations

for boundaries misoriented 20 ° and 40 ° about the [110] misorientation axis.
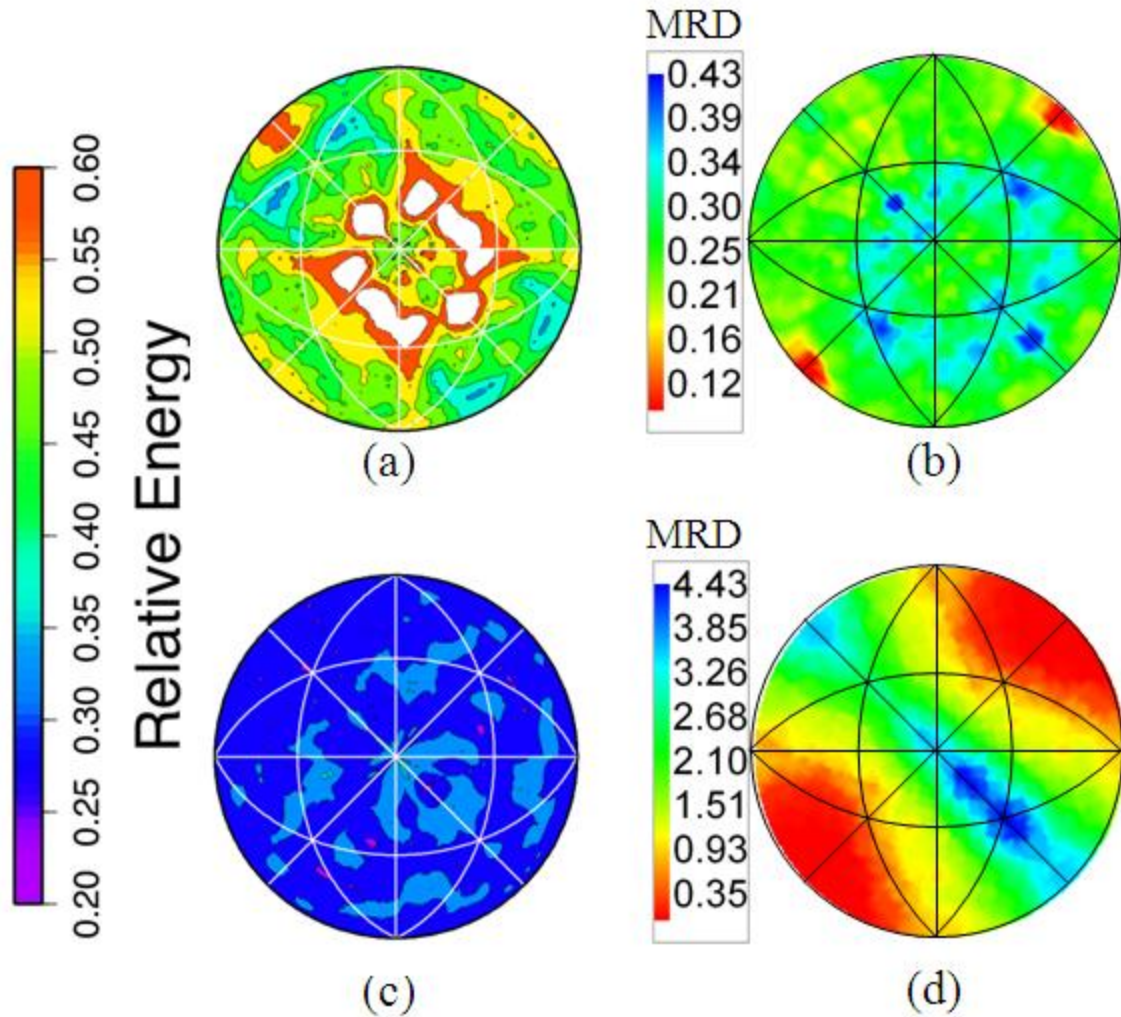
Figure 6.18 Relative grain boundary energy distributions and grain boundary plane
distributions for fixed misorientations of 20 °(a,b) and 40 ° (c,d) about the [110]
misorientation axis. An inverse correlation between grain boundary energy and
population is observed. Boundaries near the Σ9 misorientation have some of the lowest
observed grain boundary energies.

All grain boundaries with fixed misorientation of 20 ° /[110] have a relatively low

population. As with the examples of boundaries with a [100] misorientation axis, it is

observed that boundaries with this particular misorientation have high relative grain boundary energies. A fixed misorientation of 40 ° /[110] is very near the $\Sigma9$ misorientation. While the energy and population distributions are not inversely correlated in a point-by-point fashion for all plane orientations, it is observed that in general, all boundaries near the $\Sigma9$ misorientation have relatively low grain boundary energies and there is a relatively high population of these boundaries. They are, however, not the lowest energy boundaries in the material.

An inverse correlation between grain boundary population and energy is also observed when considering boundaries misoriented about the [111] axis. Fig. 6.19 shows grain boundary plane distributions and relative grain boundary energy distributions for fixed misorientations of 10 °/[111] (a,d), 40 °/[111] (b,e), and 60 °/[111] (c,f). For boundaries with 10 °/[111] and 40 °/[111], relatively low populations and relatively high grain boundary energies are observed. Coherent twins are the most populous boundary type for the high purity initial nickel sample (Fig. 6.19c). As expected, these boundaries are also the lowest energy boundaries found in the system (Fig. 6.19f). Incoherent $\Sigma3$ boundaries – boundaries with 60 °/[111] misorientation that are not terminated with {111} planes – have grain boundary energies that are at least slightly higher than that of the coherent twin.
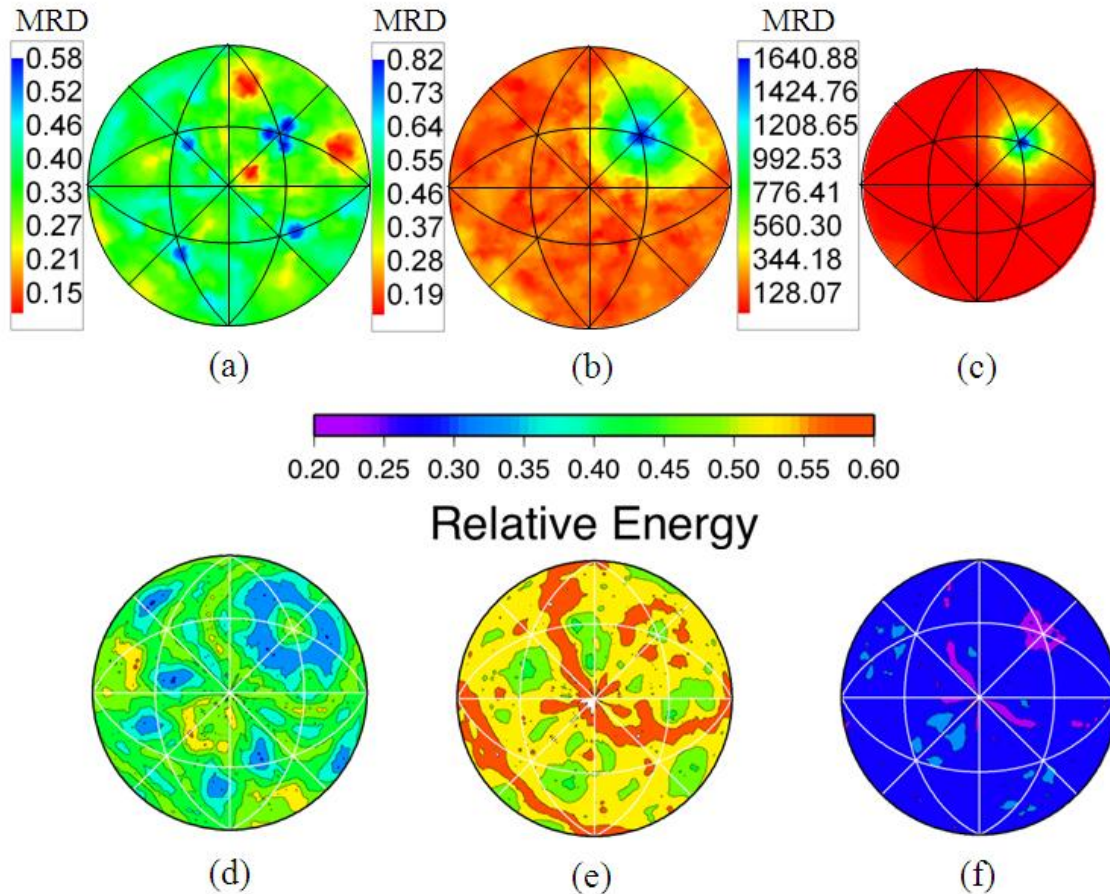
Figure 6.19 Relative grain boundary energy distributions and grain boundary plane distributions for fixed misorientations of 10 °(a,d), 40 ° (b,e) and 60 ° (c,f) about the [111] misorientation axis. An inverse correlation between grain boundary energy and population is observed. Coherent twin boundaries have the lowest recorded grain boundary energies. Incoherent Σ3 boundaries have slightly higher, but still relatively low, grain boundary energies.

6.2.7 Grain Boundary Connectivity Analysis

To explain the increase in incoherent twins in both the commercial and high purity nickel, it is hypothesized that Σ3 coherent twins are created during annealing, but that when two twins intersect, one is forced to adopt a new plane orientation. Boundaries are forced to adjust to maintain connectivity. It has been experimentally observed that Σ9

boundaries often meet with a coherent $\Sigma 3$ boundary and an incoherent $\Sigma 3$ boundary at triple junctions. Fig. 6.20 shows an example of such an interaction.
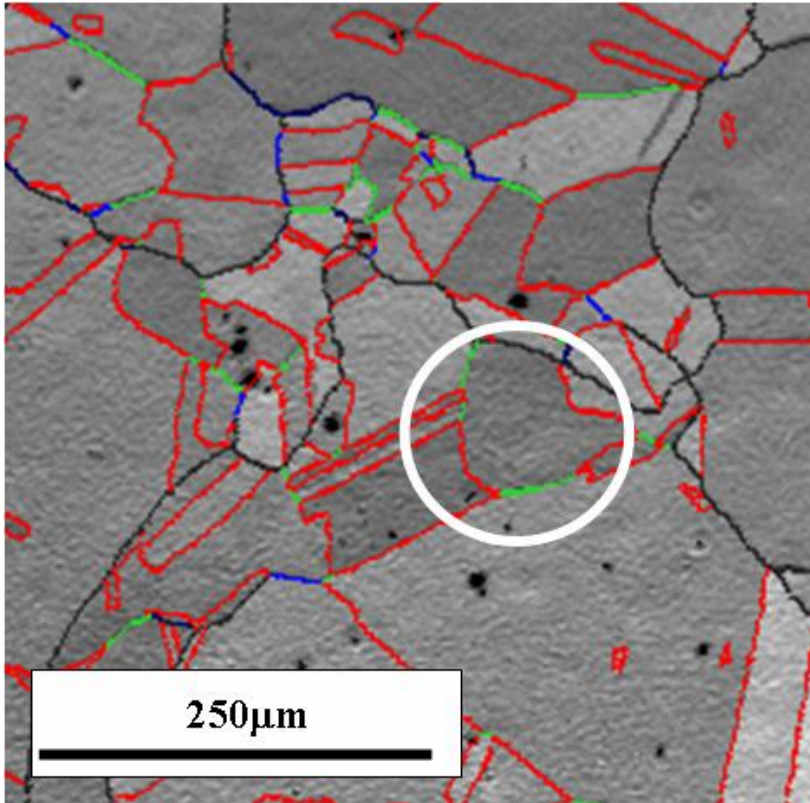
Figure 6.20 An example of $\Sigma 3^n$ boundary interaction at a triple junction is circled on an OIM image quality map. Grains are colored in gray scale according to the quality of the backscattered diffraction pattern at each point. Grain boundaries are colored according to $\Sigma 3^n$ type. $\Sigma 3$ boundaries are colored red, $\Sigma 9$ boundaries are colored green, and $\Sigma 27$ boundaries are colored blue. In this case, a $\Sigma 9$ boundary meets one coherent and one incoherent $\Sigma 3$ boundary in the circled region.

It should be noted that all of these events are occurring in a complicated, dependent manner, and we are only capable of observing which events presumably occur more frequently. Further analysis of these interactions, especially in real-time, would be vital to understanding the process.

An observable result of these interactions is the changing of the "composition" of triple junctions in the material, where composition refers to the type of boundaries that comprise the triple junction [19]. It is possible to group triple junction compositions into four groups: RRR, ΣRR, $\Sigma\Sigma$R, and $\Sigma\Sigma\Sigma$, where $\Sigma = \Sigma3^n$. A summary of this analysis for the present materials is shown in Fig. 6.22. More than 43,000 triple junctions were analyzed for the Integran reference nickel, and more than 30,000 triple junctions were analyzed for the Integran GBE nickel. 126,069 and 83,551 triple junctions were analyzed for the initial and SR5 samples, respectively. Coherency of the Σ3 boundaries was not considered in the analysis of the commercially available material, but was considered for the high purity nickel because the datasets are significantly larger and should yield more statistically robust results. In addition to the grouping of triple junction composition into four basic categories (RRR, ΣRR, $\Sigma\Sigma$R, and $\Sigma\Sigma\Sigma$, where $\Sigma = \Sigma3^n$ and n=1, 2, or 3), Σ3 coherency was also considered for this analysis. Fig. 6.21 shows the results of grouping triple junctions for the two high purity samples into four categories, and compares the results with those from the commercially available nickel.
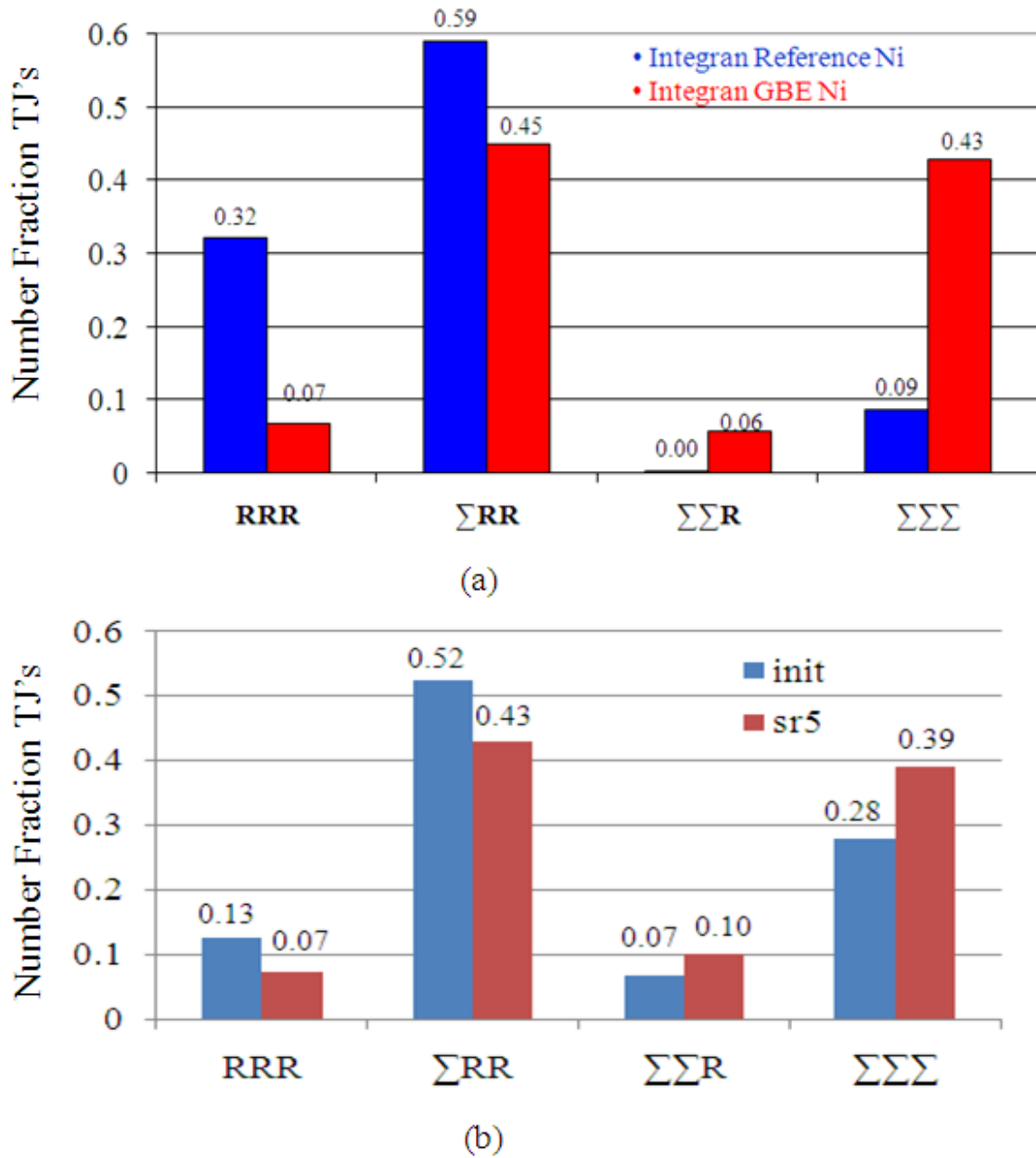
Figure 6.21 Number fraction of triple junctions composed of RRR, ΣRR, $\Sigma\Sigma$R, or $\Sigma\Sigma\Sigma$, where $\Sigma = \Sigma 3^n$ and R = random, non-$\Sigma 3^n$ boundaries for the commercial (a) and high purity (b) nickel. A significant decrease in boundaries composed entirely of random boundaries is observed with iterative thermomechanical processing. A dramatic increase in boundaries composed entirely of $\Sigma 3^n$ is observed as well. The populations of triple junction compositions are nearly the same for the high purity and commercially available nickel.

When analyzing the microstructure in this manner, it is seen that grain boundary

engineering leads to a dramatic reduction of triple junctions formed entirely of random

boundaries (RRR). There is an appreciable increase in those junctions comprised of two and three $\Sigma 3^n$ boundaries. This modification is expected to play a large role in the enhancement of properties as well. This is often explained in terms of percolation theory [84-86]. As an example, intergranular cracks may have a difficult time growing in the material as they are less likely that they can find an "easy" fracture path.

In general, it is observed that for the high purity nickel samples, the fraction of triple junctions composed of three non-$\Sigma 3^n$ boundaries ("random") or only one $\Sigma 3^n$ boundary decreases with iterative thermomechanical processing, while the fraction of triple junctions comprised of two or three $\Sigma 3^n$ boundaries increases. These trends are very similar to those observed for the commercially available nickel. It is interesting to note that while the triple junction compositions of the initial condition of the commercial and high purity nickel samples are rather different, the triple junction compositions of the "GBE" states are remarkably similar.

As noted, is has been observed that there is a greater relative increase of incoherent $\Sigma 3$ rather than coherent $\Sigma 3$ grain boundaries with thermomechanical processing in nickel. These incoherent $\Sigma 3$ boundaries might be formed through interactions at triple junctions. To test this hypothesis, the coherency of $\Sigma 3$ can also be taken into consideration when grouping triple junction types. Twenty two specific triple junction types are considered to be comprised of combinations of five boundary types: random, $\Sigma 9$, $\Sigma 27$, coherent $\Sigma 3$, and incoherent $\Sigma 3$ (all identified by the Brandon criterion). A full report of the triple junction analysis with this grouping high purity nickel initial and GBE samples can be found in the Appendix.

The populations of triple junctions with $\Sigma 3$ (coherent and incoherent), $\Sigma 9$, R

compositions are less than 1 % and remain relatively the same with thermomechanical processing. However, if triple junctions involving two $\Sigma 3$ boundaries are considered, some interesting trends emerge. Table 6.2 shows the populations of triple junction types with combinations of coherent $\Sigma 3$ (C $\Sigma 3$), incoherent $\Sigma 3$ (I $\Sigma 3$), $\Sigma 9$, and random boundaries for the junction class Σ Σ R. It is observed that there are relatively few triple junctions of type $\Sigma 3$, $\Sigma 3$ R. The populations of these triple junction types remain relatively constant with processing, as well. However, triple junctions of type $\Sigma 3$, $\Sigma 3$, $\Sigma 9$ are much more populous. The most common of these types the C $\Sigma 3$, I $\Sigma 3$, $\Sigma 9$ triple junction. While all $\Sigma 3$, $\Sigma 3$, $\Sigma 9$ triple junctions increase with processing, the C $\Sigma 3$, I $\Sigma 3$, $\Sigma 9$ type remains the most populous. This lends support to the hypothesis that at least some of the incoherent $\Sigma 3$ boundaries being formed through thermomechanical processing are the result of interactions of coherent $\Sigma 3$ being forced to adjust their orientation when connected to $\Sigma 9$ boundaries. As seen in Table 6.3, 36 % of all triple junctions in the initial sample and 47 % of all triple junctions in the SR5 sample contain at least one $\Sigma 9$ boundary. More than half of the Σ 9 boundaries connected to triple junctions belong to the type $\Sigma 3$, $\Sigma 3$, $\Sigma 9$ for each material. The fractions of triple junctions that contain at least one I $\Sigma 3$ boundary, at least one $\Sigma 9$ boundary, and at least one I $\Sigma 3$ and at least one $\Sigma 9$ boundary all increase with thermomechanical processing. For each case, approximately half of triple junctions that contain at least one I $\Sigma 3$ boundary contain at least one $\Sigma 9$ boundary (Table 6.3).

Table 6.2

Triple Junction Type	Initial, % of tjs	SR5, % of tjs
C Σ3, I Σ3, R	1.35	1.46
C Σ3, I Σ3, Σ9	10.2	13.16
C Σ3, C Σ3, R	0.36	0.37
C Σ3, C Σ3, Σ9	6.5	8.2
I Σ3, I Σ3, R	0.8	0.86
I Σ3, I Σ3, Σ9	4.13	6.23

Table 6.3

Triple Junction Type	Initial, % of tjs	SR5, % of tjs
Contains at least one I Σ3	38	48.2
Contains at least one Σ9	36.2	47.1
Contains at least one I Σ3 and at least one Σ9	17.6	24.7

Another way of thinking about network connectivity is that regions of grains related by Σ3 misorientations have grown. When the conventional grain sizes of the reference and GBE sample are determined, both are approximately 40 μm. The identical grain sizes are consistent with the measurements of the grain boundary length per area for the two samples (Table 6.1), which are also nearly the same. These observations are consistent with reports that the grain size is not altered by the grain boundary engineering process. If coherent twins are excluded from the analysis, the average grain sizes are 49 μm and 51 μm, which are again comparable. However, if all Σ3 grain boundaries are excluded, the grain sizes are 56μm and 104μm. This is a measure of the size of domains within which all of the material is related by the Σ3 misorientation. To show this graphically, we can compare the microstructures of the commercially available material with all grain boundaries marked (Fig. 6.22a and Fig. 6.22c) to the same areas when the $\Sigma3^n$ grain boundaries are eliminated. Σ9 or Σ27 boundaries are likely formed when two

$\Sigma3$s intersect, so these grain boundaries frequently connect the $\Sigma3$ boundaries within a twin related domain. It is clear that the regions of material containing only $\Sigma3^n$ grain boundaries are much larger in Fig. 6.22d. The boundary maps in Figs. 6.22b and 6.22d are consistent with the observation that the length of random boundaries per unit area decreases significantly as a result of grain boundary engineering (Table 6.1).
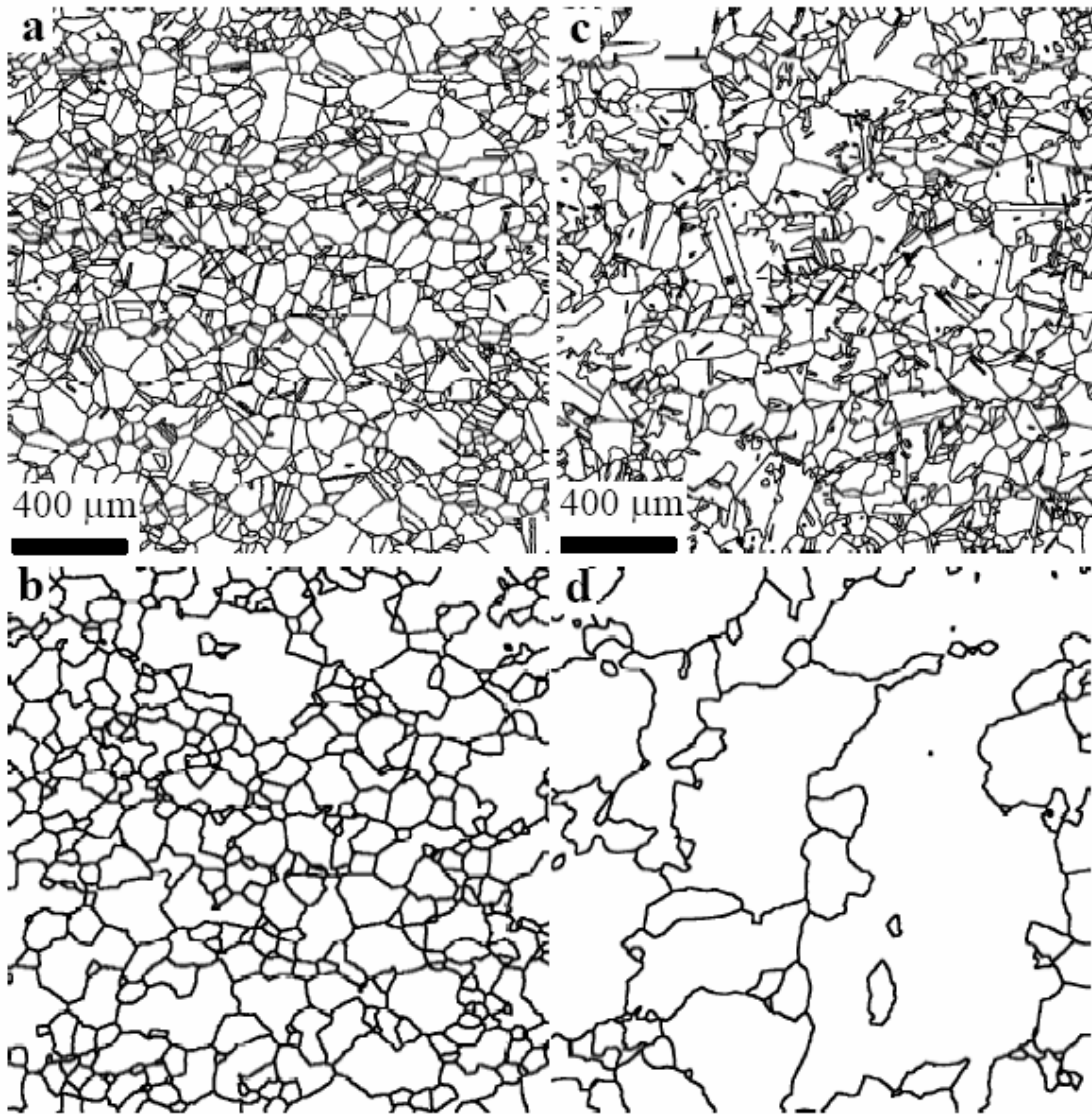
Figure 6.22 Representative skeleton grain boundary maps for Integran reference (a, b) and GBE (c, d) nickel. In maps (a) and (c), all grain boundaries are colored black. Maps (b) and (d) are plots of the same area respectively, with $\Sigma3^n$ removed. The area of material with a $\Sigma3^n$ has obviously increased with grain boundary engineering.

6.4 Discussion

Microstructural evolution during grain boundary engineering is different than during normal grain growth. Instead of the continuous elimination of boundary area to minimize the total energy as during grain growth in $SrTiO_3$, relatively low temperature-assisted boundary motion that is limited in range occurs mainly to relieve stored local strain energy imparted from light deformation. It is supposed that strongly oriented recrystallization where an undeformed crystal nucleates with an orientation closely related to the deformed grain occurs, and the nuclei grows to replace the preexisting deformed grain. However, because the orientations may be variants of the original deformed grain, new misorientations can emerge. In the ideal case, no further boundary motion occurs; thus, it is commonly reported that grain boundary engineering does not change the average grain size. If we consider length per area of grain boundaries for the commercially available material, we find that this ratio does indeed remain relatively constant. This is mainly the result of a compensation effect arising from the increase in length per area of $\Sigma 3$ boundaries and the decrease in length per area of random boundaries. As a result, twin related domains do increase in size. It is important to note that some motion of random boundaries must also occur, as the regions bounded by random boundaries coarsen, as seen in Fig. 6.22. Grain boundary network evolution during sequential thermomechanical processing was found to be similar to evolution during grain growth in the regard that relatively higher energy boundaries are being replaced by relatively lower energy boundaries. These lower energy boundaries that are increasing in population in nickel with grain boundary engineering are $\Sigma 3$ boundaries. Incoherent $\Sigma 3$ boundaries are increasing in relative population more than the lower

energy coherent $\Sigma 3$ boundaries, however, so energy effects alone cannot account for observed GBCD changes with iterative thermomechanical processing.

As in $SrTiO_3$, fractional changes in population in the GBCD of nickel can be the result of creation or elimination or boundaries, or a relative increase in boundary area. By considering the grain boundary length per area, as above, it appears that both of these mechanisms are important for the formation of the microstructure in GBE Ni. For example, the comparison of Figs 6.23c and 6.23d clearly shows that the elimination of non- $\Sigma 3^n$ grain boundaries is occurring. This is consistent with an observed decrease in the length of non- $\Sigma 3^n$ grain boundary trace per unit area. At the same time, additional incoherent $\Sigma 3$ boundaries are created, as illustrated in Fig 6.5. In other words, while the grain boundary engineering process does create additional $\Sigma 3$ boundaries, it is also effective in reducing the numbers of non- $\Sigma 3^n$ boundaries.

An increase in $\Sigma 3$ boundaries and a decrease in random boundaries lead to a higher probability of these boundaries intersecting. As $\Sigma 9$ and $\Sigma 27$ boundaries result from these interactions [81, 87], it is no surprise that the populations of these boundaries increase. A continuous network of boundaries must be formed, however, and crystallographic constraints must be obeyed. As a result, it is not always possible for a $\Sigma 3$ boundary to be bounded by the ideal low-energy $\{111\}$ type plane. Equilibrium at triple junctions forces some boundaries to adopt non-ideal boundary planes. Previous work suggests a proposed mechanism for incoherent $\Sigma 3$ boundary formation that relies on mobile $\Sigma 9$ boundaries interacting with coherent $\Sigma 3$ boundaries to create incoherent $\Sigma 3$ boundaries [88]. However, it is not clear why $\Sigma 9$ boundaries would be more mobile than random boundaries. Molecular dynamics simulations have shown coherent $\Sigma 3$

boundaries to be relatively immobile, as expected, but have also shown that incoherent

$\Sigma 3$ boundaries may actually be very mobile [89]. An alternative mechanism for

incoherent $\Sigma 3$ boundary formation is proposed here. The mechanism relies only on the

existence of at least two non-parallel coherent twins within a single grain and mobile

random boundaries. This mechanism is depicted schematically in Fig. 6.23.
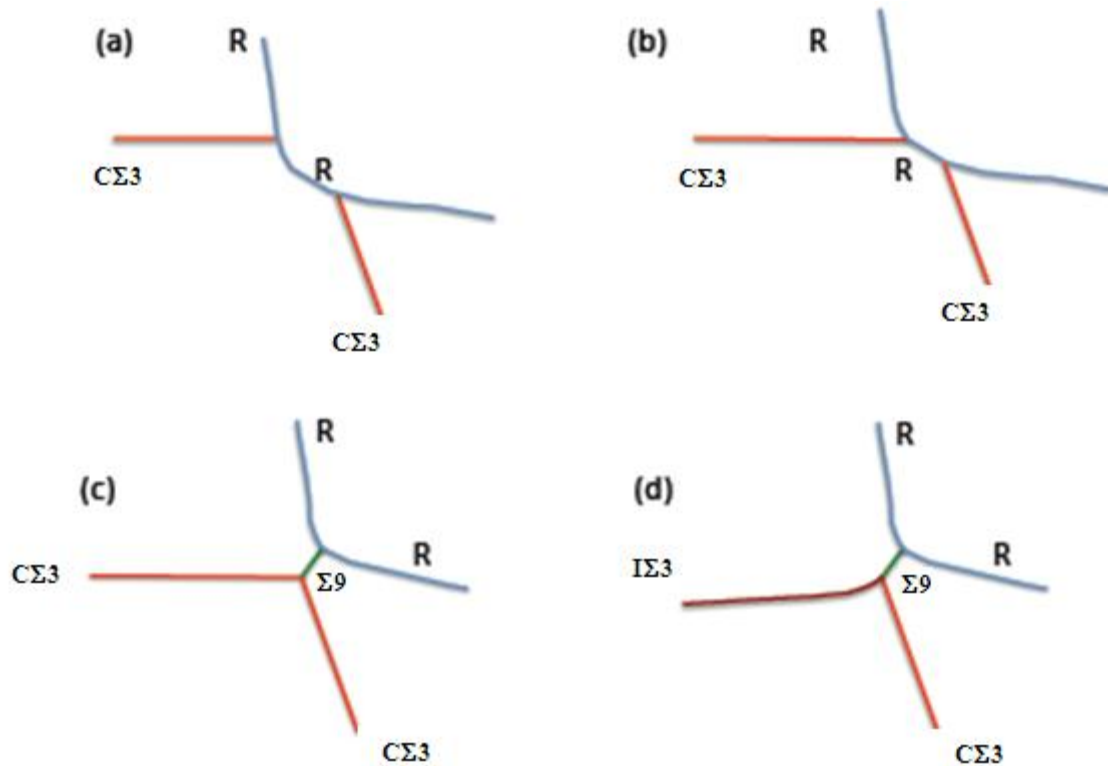
Figure 6.23 Diagram for proposed mechanism of incoherent $\Sigma 3$ formation. If two non-parallel twins exist within one grain (a), these may eventually intersect as a mobile random grain boundary recedes (b), forming a $\Sigma 9$ boundary. The geometry of the resulting boundary, dictated by crystallographic constraints is unlikely to sataisfy the criterion for the balance of interfacial energies. As a result, one or both of the coherent $\Sigma 3$ boundaries can rotate its boundary plane to balance the triple junction, forming an incoherent $\Sigma 3$ boundary.

If two non-parallel twin boundaries are allowed to intersect as a random boundary

recedes, their intersection will form a triple line. Because the intersection of two {111}

planes is always a <110>-type direction, the triple line is constrained to be along <110>.

The dihedral angle between two {111} planes must be 70.5 ° or 109.5 °. This is another constraint on the junction. Therefore, if the two twin boundaries remain fixed on {111} planes, the resulting triple junction will be of type Σ3 Σ3 Σ9 and must have dihedral angles of 70.5 °-144.75 °-144.75 ° or 109.5 °-125.25 °-125.25 °. However, it must also be true that Herring condition for interfacial equilibrium is satisfied at this junction (see Chapter 3, Section 7.1). If we ignore the torques and simplify to Young's Law, this implies that the energy ratio of C Σ3/Σ9 is 0.866 or 0.612, depending on which types of {111} planes intersect. While it is possible that one of the geometries balances the energy at junction, it is unlikely that both do. It is true that the torque terms in this case will be large and do not need to assume fixed values; however it seems unlikely that both geometries will be stable. The configuration that results in a 0.866 ratio seems particularly unlikely because the twin is expected to have a very low energy compared to other GBs. The fact that so many I Σ3C Σ3Σ9 TJs are observed supports the idea that the C Σ3C Σ3Σ9 configuration is undesirable. To correct this undesirable configuration, one of the Σ3 boundaries can rotate its boundary plane. This degree of freedom will allow the junction to balance and create a new incoherent Σ3and an I Σ3 CΣ3 Σ9 junction. Note that for this model, the populations of both types of Σ3boundaries are increased, more Σ9 boundaries are created, and the population of random boundaries is reduced, all as observed.

As seen in Table 6.2, there are appreciable fractions of C Σ3 C Σ3 Σ9 triple junctions as well and we must explain why they are not all converted to I Σ3 C Σ3 Σ9 junctions. There are several possibilities. First, only the very end of the GB needs to rotate to establish interfacial equilibrium and the triple junction geometry may not have

been determined with enough resolution in every case to capture such a detail. Second, it is possible that a boundary plane rotation within 10 ° (the threshold for separating coherent from incoherent in this work) is sufficient to balance the triple junction in some cases. Third, it is possible that one of the two C Σ3C Σ3Σ9 triple junction configurations is stable and that the rotation is sometimes not necessary.

It is known that the energies of Σ3 boundaries increase significantly for rotations away from the ideal configuration [90, 91]. When comparing the length per area of coherent and incoherent Σ3 boundaries in the GBE state, we see a greater fraction of coherent twins. This is consistent with the previous observation of an inverse correlation between grain boundary energy and grain boundary areas and populations. Again, topological and crystallographic constraints make it impossible for grains to be entirely bounded by low energy boundaries.

It should be noted that grain boundary engineering in α-brass produces rather different results than those presented here for nickel. A large increase in seen in the coherent twin population and little change is seen in the incoherent twin population. Annealing twins span the widths of grains and do little to modify the boundary network [88]. There are at least two possible reasons for the difference in results. α-brass is a relatively low stacking fault energy metal [20, 21, 91] compared to nickel, which may allow an easier formation of annealing twins than in nickel. Second, formation of annealing twins has been found to be temperature dependent [92]. Differences in the GBE conditions of α-brass and nickel may account for some observed differences in results.

Chapter 7

7. Conclusions and Future Work

7.1 Conclusions

Grain boundary energy anisotropy proved to be a major factor in dictating the evolution of the five parameter grain boundary character distribution. In general, higher energy boundaries are eliminated while lower energy boundaries increase in both number and area. In the case of grain growth in $SrTiO_3$, this is the result of the elimination and creation of grain boundaries during grain growth. A statistically indistinguishable steady state is observed for $\lambda(\mathbf{n})$, the population of grain boundary planes. This state is apparently achieved very early in the grain growth process and extends as far as has been experimentally measured. Steady state behavior was not observed for the full five parameter GBCD. Future measurements of the MDF in the current samples may show steady state behavior as seen in simulations [78], but experimental limitations may preclude any definitive claims. Surface energy anisotropy appears to be a reliable indicator of GBCD anisotropy, especially concerning boundary plane populations, which are likely to control properties.

Grain boundary energy anisotropy also proved to be a major factor in dictating the five parameter grain boundary character distribution for MgO. Doping was employed to vary the relative grain boundary energy distribution. 3000 ppm Ca-doping in MgO appears to stabilize {100} type boundary planes. As a result, an increase in anisotropy was observed in the grain boundary plane distribution with doping, favoring {100} type planes. The width of the grain boundary energy distribution, measured from thermal

grooves, also increased with doping. Changes in relative grain boundary energies brought upon by doping also had an impact the five parameter grain boundary character distribution. For fixed misorientations that favored {100} boundary plane termination, an increase in population was observed. For fixed misorientations that favored {111} boundary plane termination, a decrease in population was observed. In fact, in some cases the favored boundary plane termination switched from {111} to {100}. It appears that doping can be used as a means of predictably influencing the five parameter grain boundary character distribution if the effects of doping on the relative grain boundary energy distribution are known.

Higher energy boundaries also decrease in population while lower energy boundaries increase in population during grain boundary engineering of nickel. Because the evolution mechanism is different than in grain growth, and relies more on recrystallization and the local rearrangements of boundaries rather than large scale elimination of interfacial area, constraints placed on the resulting network of boundaries determine many of the properties. In nickel, a large increase of incoherent $\Sigma 3$ boundaries is observed. These are thought to be mainly the result of interacting $\Sigma 3$ boundaries and constraints imposed by equilibrium requirements at triple junctions. A mechanism was proposed that accounts for the observed increase of incoherent $\Sigma 3$ boundaries, $\Sigma 9$ boundaries, and triple junctions comprised of at least one of each. Lower energy coherent $\Sigma 3$ boundaries are still more frequent than incoherent $\Sigma 3$ boundaries after iterative thermomechanical processing. The areas of $\Sigma 3$-related domains tend to increase in area, even as the conventionally measured grain sizes remain the same. There is also an increase in triple junctions composed of two or more $\Sigma 3^n$ boundaries.

7.2 Future Work

Number and area weighted MDFs will be calculated for the $SrTiO_3$ zero, one, and three hour datasets. A higher than random population should be observed for 60º misorientation boundaries in the zero hour sample. Grain growth should lead to an increase in the number- and area-weighted MDF at low misorientation angles, as seen in simulation and experiment. This result would further support the observation that higher energy boundaries are being eliminated with grain growth and lower energy boundaries are both being created and increasing in area.

Previous results have shown dopant effects on the grain boundary energy anisotropy for polycrystalline ceramic systems [50]. It is hypothesized that controlling composition may provide a means for controlling the steady state GBCD. Doping was found to have no effect on the MDF for yttrium in aluminum oxide [47]. It remains unknown what effect doping will have on the MDF for MgO. The number and area-weighted MDF will be calculated for the undoped MgO sample and will be compared with the results for the Ca-doped MgO. It is expected that doping will have little effect on the MDF. Evolution of the GBCD with grain growth can also be determined for the doped MgO sample. It is expected that the GBCD will exhibit steady state behavior with grain growth, and that the achieved state will be different than that of the nominally pure sample.

8. Bibliography

[1] C. Goux, "Structure des Joints de Grains: Considerations Crystallographiques et Methods de Calcul des Structures," *Can. Metall. Q.* **13** [1], 9-31 (1974).

[2] K.T. Aust and J.W. Rutter, "Grain Boundary Migration in High-Purity Lead and Dilute Lead-Tin Alloys," *Trans. AIME*, 215, 119, (1959).

[3] G.S. Rohrer, D.M. Saylor, B.S. El-Dasher, B.L. Adams, A.D. Rollett, and P. Wynblatt, "The Distribution of Internal Interfaces in Polycrystals," *Zeit.fur Metall.*, **95,** 197-214, (2004).

[4] D.M. Saylor, B.S. El-Dasher, Y. Pang, H.M. Miller, P. Wynblatt, A.D. Rollett, and G.S. Rohrer, "Habits of Grains in Dense Polycrystalline Solids," *J. Amer.Ceram. Soc.*, **87**, 724-726, (2004).

[5] T. Sano, C.S. Kim, and G.S. Rohrer, "Shape Evolution of $SrTiO_3$ Crystals During Coarsening in a Titania-Rich Liquid," *J. Am. Ceram. Soc.,* **88**, 993-6 (2005).

[6] E.P. Gorzkowski, H.M.Chan, and M.P. Harmar, T. Sano, C.S. Kim, and G.S. Rohrer, "Changes in the Distribution of Interfaces in PMN-35 mol% PT as a Function of Time," *Zeit. furMetall.,* **96**, 207-210 (2005).

[7] E.A. Holm, G.N. Hassold, and M.A. Miodownik, "On Misorientation Distribution Evolution During Anisotropic Grain Growth," *Acta Mater.*, **49**(15), 2981–2991 (2001).

[8] J. Gruber, D.C. George, A.P. Kuprat, G.S. Rohrer, and A.D. Rollett, "Effect of Anisotropic Grain Boundary Energy on Grain Boundary Distributions During Grain Growth," *Mat. Sci. Forum*, **467-470**, 733–738, (2004).

[9] D.M. Saylor, B.S. El Dasher, B.L. Adams, and G.S. Rohrer, "Measuring the Five Parameter Grain Boundary Distribution From Observations of Planar Sections*," Met. and Mat. Trans.*, **35A**, 1981-1989, (2004).

[10]   D.M. Saylor, A. Morawiec, and G.S. Rohrer, "Distribution of Grain Boundaries in Magnesia as a Function of Five Macroscopic Parameters," *Acta Mater*, **51**, 3663-3674, (2003).

[11]   D.M. Saylor, B.S. El-Dasher, T. Sano, and G.S. Rohrer, "Distribution of Grain Boundaries in $SrTiO_3$ as a Function of Five Macroscopic Parameters," *J. Amer. Ceram. Soc*., **87**, 670-676, (2004).

[12]   D.M. Saylor, D.E. Mason, and G.S. Rohrer, "Experimental Method for Determining Surface Energy Anisotropy and its Application to Magnesia," *J. Amer. Ceram. Soc.*, **83** 1226-32 (2000).

[13]   T. Sano, D.M. Saylor, and G.S. Rohrer, "Surface Energy Anisotropy of $SrTiO_3$ at 1400° C in Air," *J. Amer. Ceram. Soc*., **86**, 1933-1939, (2003).

[14]   D.M. Saylor, A. Morawiec, and G.S. Rohrer, "The Relative Free Energies of Grain Boundaries in Magnesia as a Function of Five Macroscopic Parameters," *Acta Mater.*, **51**, 3675-3686, (2003).

[15]   M.L. Kronberg and F.H. Wilson, "Secondary Recrystallization in Copper," *Trans. AIME,* **185**, 501, (1949).

[16]   H.M. Miller, D.M. Saylor, B.S. El Dasher, A.D. Rollett, and G.S. Rohrer, "Crystallographic Distribution of Internal Interfaces in Spinel Polycrystals," Proc. 2nd Intl. Conf. on Recrystallization and Grain Growth, B. Bacroix, J.H. Driver, R. Le

Gall, Cl. Maurice, R. Penelle, H. Réglé, and L. Tabourot, eds., Annecy, France, August 2004, *Mat. Sci. Forum*, **467-470**, 783-788, (2004).

[17]   D.M. Saylor, B.S. El Dasher, A.D. Rollett, and G.S. Rohrer, "Distribution of Grain Boundaries in Aluminum as a Function of Five Macroscopic Parameters," *Acta Mater.*, **52**, 3649-3655 (2004).

[18]   T.A. Bennett, C.-S. Kim, G.S. Rohrer, and A.D. Rollett, "Five-Parameter Grain Boundary Character Distribution in Fe-1%Si," Proc. 2nd Intl. Conf. on Recrystallization and Grain Growth, B. Bacroix, J.H. Driver, R. Le Gall, Cl. Maurice, R. Penelle, H. Réglé, and L. Tabourot, eds., Annecy, France, August 2004, *Mat. Sci. For.*, **467-470,** 1057-1062, (2004).

[19]   V. Randle, G. Rohrer, and G. Owen, *Anisotropy, Texture, Dislocations, and Multiscale Modeling in Finite Plasticity and Viscoplasticity and Metal Forming*, ed. A.S. Khan and R. Kazmi (Publisher's Location: Neat Press, Inc., 2006), p. 307.

[20]   C.-S. Kim, Y. Hu, G.S. Rohrer, and V. Randle, "Five-Parameter Grain Boundary Distribution in Grain Boundary Engineered Brass," *Scripta Mater.*, **52**, 633-637, (2005).

[21]   G.S. Rohrer, V. Randle, C.-S. Kim, and Y. Hu, "Changes in the Five-Parameter Grain Boundary Character Distribution in alpha-brass Brought About by Grain Boundary Engineering," *Acta Mater.*, **54,** 4389-4502, (2006).

[22]   S.T. Downey, II, N. Bembridge, P.N. Kalu, H.M. Miller, G.S. Rohrer, and K. Han, "Grain Boundary Plane Distributions in Modified 316 LN Steel Exposed at Elevated and Cryogenic Temperatures," *J. Mater. Sci.*, **42,** 9543-47, (2007).

[23]   G.S. Rohrer, "Influence of Interface Anisotropy on Grain Growth and Coarsening," *Annual Review of Materials Research*, **35**, 99-126, (2005).

[24]   D. Wolf, "Structure-Energy Correlation for Grain Boundaries in F.C.C. Metals; I. Boundaries on the (111) and (100) Planes," *Acta Metall.*, **37**, 1983-1994, (1989).

[25]   D. Wolf, "Correlation Between Structure, Energy, and Ideal Cleavage Fracture for Symmetrical Grain Boundaries in fcc Metals," *J. Mater. Res.*, **5** [8], 1708–1730, (1990).

[26]   D. M. Saylor, E. R. Fuller, Jr., T. Weiss, "Thermal-elastic Response of Marble Polycrystals: Influence of Grain Orientation Configuration," *Int. J. Mater. Res.*, **98** [12], 1256-1263, (2007).

[27]   C.-S. Kim, A.D. Rollett, and G.S. Rohrer, "Grain Boundary Planes: New Dimensions in the Grain Boundary Character Distribution," *Scripta Mater.*, **54,** 1005-1009, (2006).

[28]   W. W. Mullins, "The Statistical Self-Similarity Hypothesis in Grain Growth and Coarsening," *J. Appl. Phys.*, **59**, 1341, (1986).

[29]   M. C. Demirel, A. P. Kuprat, D. C. George, G. K. Straub, and A. D. Rollett, "Linking Experimental Characterization and Computational Modeling of Grain Growth in Al-Foil," *Interface Sci.*, **10**, 137-141, (2002) .

[30]   E.P. Gorzkowski, H.M Chan, M.P. Harmer, T. Sano, C.-S. Kim, and G.S. Rohrer, "Changes in the Distribution of Interfaces in PMN- 35 mol% PT as a Function of Time," *Zeit.fur Metall.*, **96**, 207-210, (2005).

[31]   E. P. Gorzkowski, M. Watanabe, H.M. Chan, and M. P. Harmer, "Effect of Liquid Phase Chemistry on Single Crystal Growth in PMN-35PT," *J. Am. Ceram. Soc.*, **89** (7), 2286-2294, (2006).

[32]   P.T. King, E. P. Gorzkowski, A. M. Scotch, D.J. Rockosi, H.M. Chan, and M.P. Harmer, "Kinetics of {001} Pb(Mg1/3Nb2/3)O3 -35 mol% PbTiO3 Single Crystals Grown by Seeded Polycrystal Conversion," *J. Am. Ceram. Soc.*, **86** [12], 2182-87, (2003).

[33]   C.-S. Kim, T.R. Massa, and G.S. Rohrer, "Interface Character Distributions in WC-Co Composites," *J. Am. Ceram. Soc.*, **91**, 996-1001, (2008).

[34]   M-B. Park, S-J Shih, and D.J.H. Cockayne, "The Preferred CSL Misorientation Distribution in Polycrystalline $SrTiO_3$," *J. of Micr.,* **227**, pt. 3, 292–297, (2007).

[35]   G. Palumbo, K.T. Aust, E.M. Lehockey, U. Erb and P. Lin, "On a More Restrictive Restrictive Geometric Criterion for "Special" CSL Boundaries," *Scripta Mater.*, **38** [11], 1685–1690, (1998).

[36]   O. Kienzle, M. Exner, and F. Ernst, "Atomistic Structure of $\Sigma = 3$; (111) Grain Boundaries in Strontium Titanate," *Phys. Stat. Sol. A*, **166**, 57 (1998).

[37]   S. Gemming and M. Schreiber, "Impurity and Vacancy Clustering at the $\Sigma 3$ (1 1 1)[1 -1 0] Grain Boundary in Strontium Titanate," *Chem. Phys.*, **309**, 3–13, (2005).

[38]   M.P. Anderson, G.S. Grest, and D.J. Srolovitz, "Computer Simulation of Normal Grain Growth in 3 Dimensions," *Phil. Mag. B*, **59** (3), 293-329, 1989.

[39]   D. Weygand, Y. Brechet, J. Lepinoux, and W Gust, "Three Dimensional Grain Growth: A Vertex Dynamics Simulation," *Phil. Mag.B*, **79** (5), 703-716, (1999).

[40]   F. Wakai, N. Enomoto, and H. Ogawa, "Three-dimensional Microstructural Evolution in Ideal Grain Growth—General Statistics," *Acta Mater.*, **48**, 1297-1311, (2000).

[41]   C.E. Krill and L. –Q. Chen, "Computer Simulation of 3-D Grain Growth Using a Phase-Field Model," *Acta Mater.*, **50**, 3059-3075, (2002).

[42]   M. Upmanyu, G.N. Hassold, A. Kazaryan, E.A. Holm, Y. Wang, B. Patton, and D.J. Srolovitz, "Boundary Mobility and Energy Anisotropy Effects on Microstructural Evolution During Grain Growth," *Interface Sci.*, **10**(2-3), 201–216, (2002).

[43]   N. Ono, K. Kimura, and T. Watanabe, "Monte Carlo Simulation of Grain Growth with the Full Spectra of Grain Orientation and Grain Boundary Energy," *Acta Mater.*, **47**(3), 1007-1017, (1999).

[44]   D. Kinderlehrer, I. Livshits, G.S. Rohrer, S. Ta'asan, and P. Yu, "Mesoscale Simulation of the Evolution of the Grain Boundary Character Distribution," Proc. 2nd Intl. Conf. on Recrystallization and Grain Growth, B. Bacroix, J.H. Driver, R. Le Gall, Cl. Maurice, R. Penelle, H. Réglé, and L. Tabourot, eds., Annecy, France, August 2004, *Materials Science Forum*, **467-470,** 1063-1068, (2004).

[45]   A. Kazaryan, Y. Wang, S.A. Dregia, and B.R. Patton, "Grain Growth in Anisotropic Systems: Comparisons of Effects of Energy and Mobility," *Acta Mater.*, **50**(3), 499-510, (2002).

[46]   J. Gruber, D.C. George, A.P. Kuprat, G.S. Rohrer, A.D. Rollett, "Effect of Anisotropic Grain Boundary Properties on Grain Boundary Plane Distributions During Grain Growth," *Scripta Mater.*, **53**, 351-355, (2005).

[47]   J.H. Cho, H.M. Chan, M. P. Harmer, J.M. Rickman, "Influence of Yttrium Doping on Grain Misorientation in Aluminum Oxide," *J.Am.Ceram.Soc.*, 81[11], 3001-3004, (1998).

[48]   S. Suzuki, K. Abiko, H. Kimura, "Phosphorus Segregation Related to the Grain-Boundary Structure in an Fe-P Alloy," *Scripta Metall.*, **15**, 1139-1143, (1981).

[49]   W. Swiatnicki, S. Lartigue-Korinek, A. Dubon, and J. Y. Laval, "Intergranular Segregation and Grain Boundary Crystallography in Al_2O_3," *Mater. Sci. Forum*, 193, 126– 128, (1993).

[50]   Y. Pang and P. Wynblatt, "Effects of Nb Doping and Segregation on the Grain Boundary Plane Distribution in TiO_2," *J. Am. Ceram. Soc.*, **89** [2] 666 – 671, (2006).

[51]   M. Ramamoorthy, D. Vanderbilt, R.D. King-Smith, "1st Principles Calculations of the Energetics of Stoichiometric TiO_2, Surfaces," *Phys. Rev. B*, **49**[23], 16721-16727, (1994).

[52]   T. Watanabe, "An Approach to Grain Boundary Design for Strong and Ductile Polycrystals," *Res. Mech.*, 11, 47–84, (1984).

[53]   P. Lin et al., "Influence of Grain Boundary Character Distribution on Sensitization and Intergranular Corrosion of Alloy 600," *Scripta Met. et Mat.*, **33** (9), 1387–1392, (1995).

[54]   G. Palumbo, E.M. Lehockey, P. Lin, U. Erb, K.T. Aust, "Interfacial Engineering for Optimized Properties," *Materials Research Society Symposium Proceedings, Pittsburgh, PA*, 458, 273–282, (1997).

[55]   G. Palumbo et al., "Grain Boundary Design and Control for Intergranular Stress-Corrosion Resistance," *Scripta Met. et Mat.*, **25** (8), 1775–1780, (1991).

[56]   G. Palumbo et al., "Grain Boundary Engineering for Intergranular Fracture and Creep Resistance," *Proc. of Micros. and Microan. '96*, 362–363, (San Francisco, CA: San Francisco Press, 1996).

[57]   E.M. Lehockey et al., "Grain Boundary Engineered Lead Alloys," *Mat. Res. Soc. Symp. Proc.*, 458, 243–248, (Pittsburgh, PA: MRS, 1997).

[58]   V. Randle, H. Davies, "Evolution of Microstructure and Properties in alpha-brass After Iterative Processing," *Met. and Mat. Trans. A*, **33**(6), 1853-1857, (2002).

[59]   V. Randle, "'Special' Boundaries and Grain Boundary Plane Engineering," *Scripta Mat.*, **54**(6), 1011-1015, (2006).

[60]   V. Randle, "Twinning-Related Grain Boundary Engineering," *Acta Mat.*, **52**, 4067-4081, (2004).

[61]   A.J. Schwartz, W.E. King, M. Kumar, "Influence of Processing Method on the Network of Grain Boundaries," *Scripta Mat.*, **54**, 963-968, (2006).

[62]   B.L. Adams, S.I. Wright, and K. Kunze, "Orientation Imaging—The Emergence of a New Microscopy," *Met. Trans. A*, **24** (4), 819–831, (1993).

[63]   S. Kikuchi, "Diffraction of Cathode Rays by Mica," *Japanese Journal of Physics*, **5**, 83-96, (1928).

[64]   S.-B. Lee, A. D. Rollett, and G. S. Rohrer, "Three-Dimensional Microstructure Reconstruction Using FIB-OIM", *Materials Science Forum*, **558-559**, 915-920, (2007).

[65]   J.E. Hilliard, "Specification and Measurement of Microstructural Anisotropy," *Trans. Metall. Soc. AIME*, **224**, 1201-1211, (1962).

[66]   B.L. Adams, "Description of the Intercrystalline Structure Distribution in Polycrystalline Materials," *Met. and Mat. Trans. A*, **17**(12), 2199-2207, (1986).

[67]   S.I. Wright, R.J. Larsen, "Extracting Twins from Orientation Imaging Scan Data," *J. Micro.*, **205**(3), 245-52, (2002).

[68]   A.P. Sutton, R.W Balluffi, "Interfaces in Crystalline Materials," Chapter 5, Oxford: Clarendon Press, (1995).

[69]   M.M. Nowell, S.I. Wright, "Orientation Effects on Indexing of Electron Backscatter Diffraction Patterns," *Ultramicr.*, **103**, 41-58, (2005).

[70]   F. Papillion, H. Miller, P. Wynblatt, G.S. Rohrer, in preparation

[71]   www.integran.com

[72]   A.J. Schwartz, W.E. King, "The Potential Engineering of Grain Boundaries Through Thermomechanical Processing," *JOM*, **February**, 50-55, 1998.

[73]   V. Randle, "Mechanism of Twinning-Induced Grain Boundary Engineering in Low Stacking-Fault Energy Materials," *Acta Metall.*, **47** [15], 4187-4196, (1999).

[74]   C. Herring, "Surface Tension as a Motivation for Sintering," 143–79, in *ThePhysics of Powder Metallurgy.* Edited by W. E. Kingston. McGraw-Hill, New York, (1951).

[75]   W. W. Mullins, "Theory of Thermal Grooving," *J. Appl. Phys.*, **28** [3], 333–339, (1957).

[76]   D.M. Saylor and G.S. Rohrer, "Measuring the Influence of Grain Boundary Misorientation on Thermal Groove Geometry in Ceramic Polycrystals," *J. Amer. Ceram. Soc.*, **82**, 1529-1536, (1999).

[77]   C. A. Handwerker, J. M. Dynys, R. M. Cannon, and R. L. Coble, "Dihedral Angles in Magnesia and Alumina: Distributions from Surface Thermal Grooves," *J. Am. Ceram. Soc.*, **73** [5] 1371–77 (1990).

[78]   S.J. Dillon and G.S. Rohrer, "Characterization of the Grain Boundary Character and Energy Distributions of Yttria using Automated Serial Sectioning and EBSD in the FIB," *J. Am. Ceram. Soc.*, submitted, 2008

[79]   A. Morawiec, "Calculation of Distribution of Grain Boundary Energy Over Grain Misorientations," *Scripta Mat.*, **41**, 13-18, (1999).

[80]   J. Gruber, H.M. Miller, T.D. Hoffman, A.D. Rollett, and G.S. Rohrer, "Misorientation Texture Development During Grain Growth: Part 1 – Random Orientation Texture," in preparation

[81]   G. Palumbo, K.T. Aust, U. Erb, and P.J. King, "," *Phys. Stat. Sol.*, **131**, 425, (1992).

[82]   H.M. Miller, C.-S. Kim, J. Gruber, V. Randle, and G.S. Rohrer, "Orientation Distribution of Sigma-3 Grain Boundary Planes in Ni Before and After Grain Boundary Engineering," *Mat. Sci. For.*, **558-559**, 641-647, (2007).

[83]   D.G. Brandon, "The Structure of High-Angle Grain Boundaries," *Acta Metall*, **14**, 1479, (1966).

[84]   D.B. Wells, J. Stewart, A.W. Herbert, P.M. Scott, D.E. Williams, "The Use of Percolation Theory to Predict the Probability of Failure of Sensitized, Austenitic Stainless-Steel by Intergranular Strees-Corrosion Cracking," *Corrosion*, **45**, 649-660, (1989).

[85]   L.C. Lim, T. Watanabe, "Fracture-Toughness and Brittle-Ductile Transition Cotrolled by Grain Boundary Character Distribution (GBCD) in Polycrcystals," *Acta Metall. et Mater.*, **38** [12], 2507-2516, (1990).

[86]   C.A. Schuh, R.W. Minich, M. Kumar, "Connectivity and Percolation in Simulated Grain-Boundary Networks," *Phil. Mag.*, **83**:6, 711-726, (2003).

[87]   V. Randle, "Mechanisms of Twinning-Induced Grain Boundary Engineering in Low Stacking-Fault Energy Materials," *Acta Mat.*, **47**, 4187-4196, (1999).

[88]   V. Randle, G. Owen, "Mechanisms of Grain Boundary Engineering," *Acta Mat.*, **54**, 1777–1783, (2006).

[89]   K. G. F. Janssens, D. Olmsted, E. A. Holm, S. M. Foiles, S. J. Plimpton, P. M. Derlet, "Computing the Mobility of Grain Boundaries," *Nature Mat.*, **5**, 124-127, (2006).

[90]   U. Wolf, F. Ernst, T. Muschik, M.W. Finnis, and H.F. F, "The Influence of Grain-Boundary Inclination on the Structure and Energy of Sigma=3 Grain-Boundaries in Copper," *Phil. Mag.*, **A66**, 991, (1992).

[91]   C. B. Thompson and V. Randle, "A Study of Twinning in Nickel," *Scripta Mat.*, **35**, 385-390, (1996).

[92]   B.B. Rath, M.A. Imam, C.S. Pande, "Nucleation and Growth of Twin Interfaces in FCC Metals and Alloys," *Mater. Phys. Mech.*, **1**, 61-66, (2000).

Appendix A. Full Triple Junction Analysis of High Purity Nickel

This appendix contains the full report of the triple junction analysis with the

grouping that considers $\Sigma 3$ coherency for the high purity nickel initial and GBE samples

as referenced in Chapter 6, Section 2.7.

TJ type			high purity Ni as received		SR5	
			number	% of total	number	% of total
(R,	R,	R)	15841	12.64	5959	7.23
(coh3,	R,	R)	32378	25.83	16870	20.46
(incoh3,	R,	R)	21559	17.2	12019	14.58
(coh3,	coh3,	9)	8152	6.5	6764	8.2
(incoh3,	incoh3,	9)	5178	4.13	5140	6.23
(coh3,	incoh3,	9)	12785	10.2	10850	13.16
(coh3,	incoh3,	R)	1697	1.35	1205	1.46
(coh3,	coh3,	R)	452	0.36	308	0.37
(incoh3,	incoh3,	R)	1007	0.8	711	0.86
(9,	R,	R)	8578	6.84	4343	5.27
(9,	9,	R)	447	0.36	471	0.57
(9,	9,	9)	464	0.37	421	0.51
(incoh3,	9,	R)	651	0.52	501	0.61
(coh3,	9,	R)	538	0.43	339	0.41
(27,	R,	R)	3207	2.56	2162	2.62
(27,	27,	R)	165	0.13	276	0.33
(coh3,	27,	R)	1743	1.39	2339	2.84
(coh3,	9,	27)	5116	4.08	5240	6.36
(incoh3,	9,	27)	3400	2.71	3866	4.69
(9,	27,	27)	402	0.32	413	0.5
(incoh3,	27,	R)	1273	1.02	1775	2.15
(9,	27,	R)	303	0.24	482	0.58
Totals			125336	100	82454	100

Appendix B. List of Figures